2021
June

HIDRAULICA

HYDRAULICS-PNEUMATICS-TRIBOLOGY-ECOLOGY-SENSORICS-MECHATRONICS

No. 2

ISSN 1453-7303
ISSN-L 1453-7303

CAD - CAE - CAM

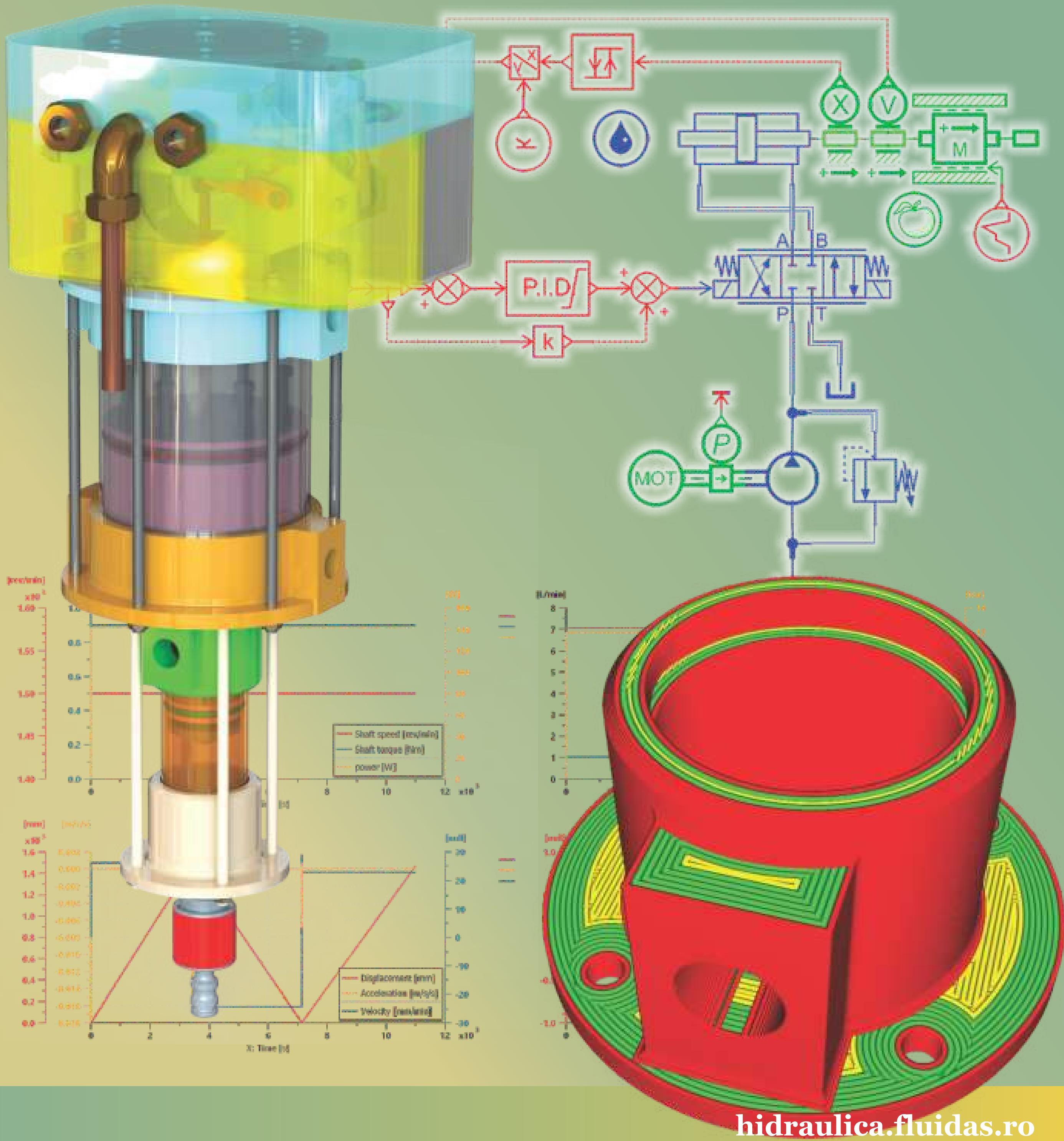

hidraulica.fluidas.ro

CONTENTS

EDITORIAL: Despre actualitatea unei viziuni / On the relevance of a vision Ph.D. Eng. **Cătălin DUMITRESCU**	5 - 6
• **Modeling and Simulating the Operation of the Hydraulic Tool Holder Tightening/Releasing Systems Served by Accumulators** Prof. PhD Eng. **Anca BUCUREȘTEANU**, Assoc. Prof. PhD Eng. **Adrian MOTOMANCEA**, Assistant **Alina OVANISOF**	7 - 14
• **Comparative Study of the Effect of the Compression and Traction Loads on the Stress and Deformation of a Toroidal LPG Tank** Assistant professor PhD. Eng. **Petre OPRIŢOIU**	15 - 28
• **Analysis of Heat Flow and Transfer in the T Joint of a Steam Installation** Prof.Dr.eng. **Mariana PANAITESCU**, Prof.Dr.eng. **Fănel-Viorel PANAITESCU**, PhD student **Robert-Alexandru DĂINEANU**	29 - 41
• **Comparative Study on Providing the Necessary Heating for a Renewable Air Treatment Plant** Prof. Dr. Eng. **Valentin APOSTOL,** Șl. Dr. Eng. **Mihaela CONSTANTIN,** Conf. Dr. Eng. **Horațiu POP,** Șl. Dr. Eng. **Beatrice IBREAN,** Std. **Cristian MARIN,** As. Dr. Eng. **Daniel TABAN**	42 - 48
• **Design and Study of Hydraulic Systems** Dipl. Eng. **Mihai DIACONU**, PhD. Eng. **Tiberiu AXINTE**, Dipl. Eng. **Cătălin FRĂȚILĂ**, Prof. PhD. Eng. **Paul BOCĂNETE**, Dipl. Eng. **Remus COJOCARU**	49 - 56
• **Rainwater Harvesting, a Solution to Reduce Drinking Water Consumption for Buildings** Assoc. Prof. Dr. Eng. **Adriana TOKAR**, Dipl. Eng. **Paul FRASIE**, Res. Asst. PhD. student Eng. **Dănuț TOKAR**	57 - 63
• **Theoretical Possibilities of Using Building Integrated Wind Turbines for Urban Energy Production** Assistant professor **Fănel Dorel ȘCHEAUA**	64 - 69
• **Analysis of Pneumatic Circuits with FluidSim** Dipl. Eng. **Remus COJOCARU**, Prof. PhD. Eng. **Paul BOCĂNETE**, Assoc. Prof. PhD. Eng. **Dumitru DELEANU**, Dipl. Eng. **Cătălin FRĂȚILĂ**, PhD. Eng. **Tiberiu AXINTE**, Dipl. Eng. **Mihai DIACONU**	70 - 75
• **Comparison of Rainfall Interpolation Methods for Obtaining Mean Annual Maximum Precipitation Isohyets in a High Elevation Zone in Mexico** Dra. **Maritza ARGANIS**, M.I. **Margarita PRECIADO**, M.I. **Juan José BAÑOS**, Dr. **Alejandro MENDOZA**	76 - 89
• **Acoustic Monitoring of Diesel Engine** Dr. **S. NARAYAN**, Dr. **Vipul GUPTA**	90 - 96
• **Intelligent Hydraulic System for Comparative Functional Testing of Biodegradable Working Fluids** PhD Stud. Eng. **Liliana DUMITRESCU,** PhD Stud. Eng. **Ștefan-Mihai ȘEFU,** PhD Stud. Eng. **Ionela-Mihaela BACIU,** PhD Eng. **Marian BLEJAN**	97 - 102
• **A Review of Combustion-Based Noise in Engines** Dr. **Vipul GUPTA,** Dr. **S. NARAYAN**	103 - 107

BOARD

Published by:
Hydraulics and Pneumatics Research Institute, Bucharest-Romania
Address: 14 Cuţitul de Argint, district 4, Bucharest, 040558, Romania
Phone: +40 21 336 39 91; Fax: +40 21 337 30 40; e-Mail: ihp@fluidas.ro; Web: www.ihp.ro
with support from:
National Professional Association of Hydraulics and Pneumatics in Romania - FLUIDAS
e-Mail: fluidas@fluidas.ro; Web: www.fluidas.ro

HIDRAULICA Magazine is indexed by international databases

ISSN 1453 – 7303; ISSN – L 1453 – 7303

EDITORIAL

Despre actualitatea unei viziuni

Dr. Ing. Cătălin DUMITRESCU
MEMBRU AL ECHIPEI REDACȚIONALE
DIRECTOR INOE 2000-IHP

În urmă cu aproape 28 ani, mai exact în 8 Decembrie 1993, profesorul W. Backé susținea în The eightieth Thomas Hawksley Memorial Lecture in London o prelegere intitulată ***"The present and future of fluid power"***; materialul se găseste în mediul electronic sub forma unui articol cu același titlu și este impresionant prin capacitatea de a previziona actualul stadiu al dezvoltării domeniului fluid power, la trecerea a aproape 3 decenii.

Cea mai interesantă parte a articolului nu se referă la recunoașterea veșnicei amenințări a acționărilor mecanice și electrice asupra celor hidraulice, în special; pentru aceasta, profesorul Backé sintetizează 3 direcții generale de abordare pentru viitor (utilizarea avantajelor specifice, compensarea dezavantajelor și utilizarea avantajelor altor tehnologii care pot fuziona cu hidraulica). După cum spuneam, cea mai interesantă parte a articolului este cea finală, în care sunt trasate 11 posibile direcții de dezvoltare a domeniului fluid power; este uimitor cum astăzi aceste direcții capătă noi valențe, legate de realitățile actuale.

Prima direcție se referea la "**Intensified application of computer programs to optimize motion, flow, noise**" – astăzi programele de modelare / simulare reduc timpii de lucru și cheltuielile prin pre-vizualizarea rezultatelor.

A doua prognoză se referea la "**Application of new materials: coatings, ceramics, plastics...**" – putem vedea câte programe de cercetare actuale au în vedere utilizarea de materiale noi, lăsând la o parte noile tehnici de tip 3D, care nu puteau fi previzionate la acel moment.

În ceea ce privește cel de-al treilea punct, "**Application of energy-savings components and systems**", pe lângă ceea ce se recomanda în acel moment, legat de load sensing și extinderea unităților cu variable displacement, în prezent s-au adăugat noile direcții de hidraulică digitală, Direct Drive Hydraulics și altele.

Punctul 5, "**Development and use of biological degradable pressure fluids**", este cât se poate de actual în contextul protejării mediului și este una dintre direcțiile de acțiune care se regăsesc în conceptul de Economie Circulară.

Și dacă tot vorbim de concepte actuale, cum vi se pare analogia dintre "**Integration of component-related electronics and sensors into device, e.g. variable displacement units, cylinders, proportional valves** – punctul 10" și termenul actual de "hidraulică inteligentă", ca parte a IoT?!

Cred că această trecere în revistă, deși incompletă din lipsă de spațiu, este elocventă pentru viziunea pe care marile personalități ale domeniului nostru o pot avea...

EDITORIAL

On the relevance of a vision

Ph.D.Eng. Cătălin DUMITRESCU
EDITORIAL BOARD MEMBER
DIRECTOR OF INOE 2000-IHP

Almost 28 years ago, on December 8, 1993, Professor W. Backé gave a lecture at The eightieth Thomas Hawksley Memorial Lecture in London, titled **“*The present and future of fluid power*”**; the material can be found online in the form of an article with the same title, and it is impressive in its ability to predict the current stage of development of the fluid power field, at the end of almost 3 decades.

The most interesting part of the article does not refer to the recognition of the eternal threat of mechanical and electrical drives on hydraulic ones, in particular; for this, Professor Backé summarizes 3 general directions for the future (use of specific advantages, compensation of disadvantages, and use of the advantages of other technologies that can merge with hydraulics). As I said, the most interesting part of the article is the final one, which outlines 11 possible directions for the development of the fluid power field; it is amazing how today these directions acquire new valences, related to the current realities.

The first direction referred to "**Intensified application of computer programs to optimize motion, flow, noise**" - Today modeling / simulation programs reduce working time and costs by allowing to preview the results.

The second forecast referred to "**Application of new materials: coatings, ceramics, plastics ...**" - We can see how many current research programmes consider the use of new materials, leaving aside the new 3D techniques, which could not have been predicted at that time.

Regarding the third point, “**Application of energy-saving components and systems**”, in addition to what was recommended at that time, related to load sensing and extensive use of variable displacement units, new directions have been added nowadays: Digital Hydraulics, Direct Drive Hydraulics, and others.

Point 5, “**Development and use of biological degradable pressure fluids**”, is very up-to-date in the context of environmental protection, and it is one of the directions of action that can be found within the concept of Circular Economy.

And since we keep talking about current concepts, what do you think of the analogy between "**Integration of component-related electronics and sensors into device, e.g. variable displacement units, cylinders, proportional valves"** - point 10, and the current term of "Intelligent Hydraulics" as part of IoT?!

I think that this review, although incomplete due to insufficient space, is indicative of the vision that the great personalities of our field can have ...

ISSN 1453 – 7303 "HIDRAULICA" (No. 2/2021)
Magazine *of Hydraulics, Pneumatics, Tribology, Ecology, Sensorics, Mechatronics*

Modeling and Simulating the Operation of the Hydraulic Tool Holder Tightening/Releasing Systems Served by Accumulators

Prof. PhD Eng. **Anca BUCUREȘTEANU[1*],** Assoc. Prof. PhD Eng. **Adrian MOTOMANCEA[1],** Assistant **Alina OVANISOF[1]**

[1] University POLITEHNICA of Bucharest

[*] ancabucuresteanu@gmail.com, (adrian.motomancea@deltainfo.ro, alinaovanisof@yahoo.com)

Abstract: *In this paper, the authors present the theoretical research, the mathematical models, and also the results of the research carried out during the production of turning tool holder tightening/releasing systems used in vertical lathes. These mechanical-hydraulic systems are typically used for vertical lathes in the SC12 - SC43 range. The work is intended to create a mathematical model that will enable these systems to be more reliable and efficient. Some results of the simulation of system operation are also presented.*

Keywords: *Hydraulic systems with accumulator, tool holder tightening/releasing systems, machine-tools*

1. Presentation of the Installation

Vertical lathes [1, 2] are intended for metalworking in the presence of high-value machining forces and torques. The tool holders of these machines must ensure accurate positioning and high rigidity.
As a rule, the tool holders are tightened mechanically using a disc spring [1, 2]. To increase the tightening forces and the rigidity and reliability of the systems, mechanical tightening can be supplemented by hydraulic tightening. As a rule, tool holders are loosened hydraulically.
The pressures required to achieve the tightening forces are maintained by hydro-pneumatic accumulators. They are filled with nitrogen at a pressure determined by the requirements of the installation. During the various stages of work, the gas undergoes isotherm or adiabatic transformations [3, 4, 5, 6, 7, 8].
Hydro-pneumatic accumulators, apart from being additional energy sources, can also ensure increased operational safety, can take over thermal oil expansion, etc. [3, 4, 7, 9].
Figure 1 shows the hydraulic diagram of a tool holder tightening/releasing unit used for vertical lathes. The figure only shows this system, but the hydraulic source also serves other consumers: the indexing/unindexing system of the crossbar, the locking/unlocking system of the crossbar etc.
The constant flow pump P is driven by the EM electric motor and sucks oil through the F_1 filter from the T tank. The oil purity (10 μm) is ensured by the F_2 filter.
During operation, the pressure in the main circuit is displayed on the M_1 pressure gauge. The maximum pressure (p_M) is adjusted by means of the pressure valve PV.
By operating the S_1 electromagnet from the directional valve D_1, it is ensured that the pressure source (pump and pressure valve) is connected to the supply circuit of the tightening/release cylinder of the C tool holder.
The tool holder is tightened using the SK disc spring system and the pressure provided on the S_2 surface on path A. If pressure oil is supplied on path B, the force developed by it on the S_1 surface compresses the SK springs, thus achieving the release. Such positions of the C cylinder rod are confirmed by the L_1 and L_2 thrusts. On path A of the D_2 directional valve there are the PS_1 and PS_2 pressure switches set at pressures p_1 and p_2. Pressure p_1 is the minimum pressure that ensures tightening and pressure p_2 is the maximum pressure in this circuit.
Also here there is the V_0 volume Ac accumulator, initially filled with nitrogen at pressure p_0. The circuit with accumulator is sealed by the hydraulic pilot operated check valve HPOCV [5]. By operating the S_2 electromagnet, the D_2 directional valve releases the tool holder. In this case, pressure is sensed by the PS_3 pressure switch. It is adjusted at p_3 pressure. The pressure in the accumulator circuit is displayed using the M_2 gauge.
The above pressures shall observe the following conditions: $p_0 < p_1 < p_2 < p_M$ and $p_3 < p_M$.

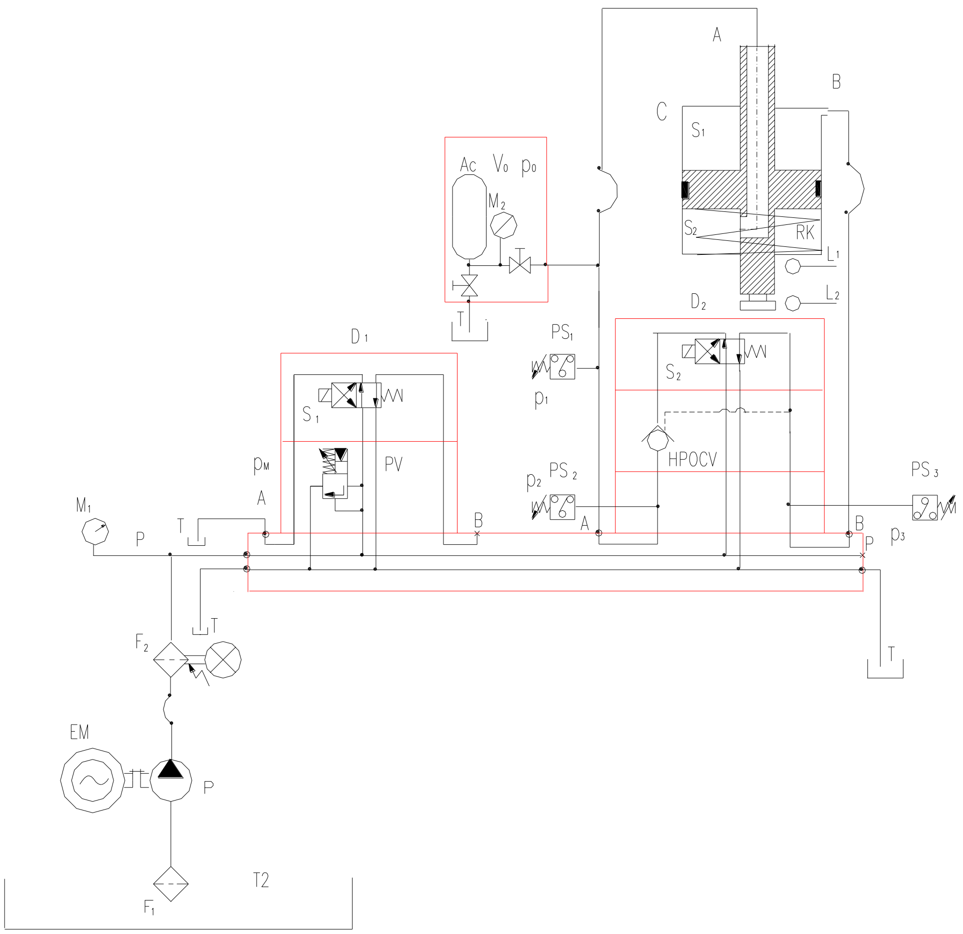

Fig. 1. The simplified hydraulic diagram of the tool holder tightening/releasing system

The operation of the installation shown in the diagram in Figure 1 is summarized in Table 1.

Table 1: The operation of the installation

	EM	S_1	S_2	PS_1	PS_2	PS_3	L_1	L_2	M_1	M_2
STOP	-	-	-				+	-	0	0 - p_2
Pump START	+	-	-				+	-	0	0 - p_2
Initial charge	+	+	-	+	+	-	+	-	p_2	p_2
Tool holder release	+	+	+	-	-	+	-	+	p_3	0
Tool holder tightening	+	+	-	+	+	-	+	-	p_2	p_2
Machine ON	+	-	-	+	+ → -	-	+	-	0	p_1 - p_2

The accumulator Ac provides proper operation, safety and reliability of the installation.
Figure 2 shows how the equipment in Figure 1 is placed on the machine, keeping the same notations.
In a lossless, properly executed and operated installation, the accumulator maintains the pressure required to tighten the tool holder as long as the tightened tool carrier is engaged in the desired cutting process.
If, however, over time, fluid is lost in the accumulator circuit, the system consisting of pump P, pressure valve PV and pressure switches PS_1 and PS_2 ensures, within certain limits, that the circuit of the accumulator on the path of the D_2 directional valve is refilled.

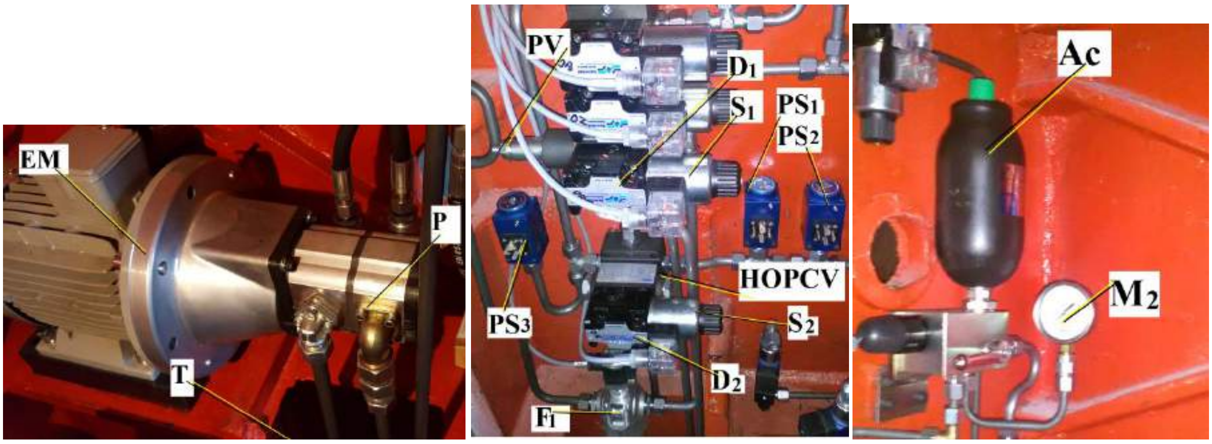

Fig. 2. The placement of the hydraulic equipment on the machine

2. Proposed Mathematical Models

The elementary source [6] consisting of pump P and pressure valve PV supplies a Q flow to the installation only when electromagnet S_1 of the D_1 directional valve is driven. The dependence of this pressure flow displayed on the M_1 pressure gauge is shown in Figure 3.

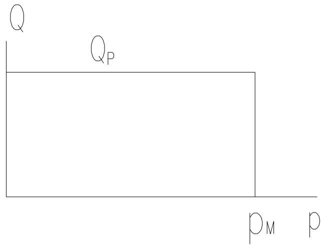

Fig. 3. The characteristic of the elementary source

The tool holder is tightened and released and the accumulator circuit is charged according to Table 1.
Under these conditions, the accumulator can be in the following situations:
a. initial charge or after the tool holder release command;
b. discharge of the accumulator due to accidental leakage through seals;
c. charging during tightening the tool holder to cover losses from the previous point;
d. discharge of the accumulator during the tool holder release phase.

a. Initial charging (when starting the machine) or after the tool holder release command

The source is considered to release liquid at pressure p_M. It enters the accumulator where gas is present, initially at pressure p_0, so as, finally, the PS_2 pressure switch commands the charge to stop when the pressure p_2 is reached. The accumulator pressure shall be considered to have a constant value equal to the average of the two. The flow rate discharged depends on the characteristics of the circuit portion and on the oil density [5, 6]. All these constants for the charging circuit shall be noted with K_1. The constant of the discharge circuit is defined in a similar way and will be noted with K_2. The constant of the circuit where losses occur shall be noted as K_3.
The charge diagram in this first case is shown in Figure 4.
During charging, losses are considered negligible.
The liquid volume sent to the accumulator ΔV_1 is:

$$\Delta V_1 = V_0\left(1 - \frac{p_0}{p_2}\right) \tag{1}$$

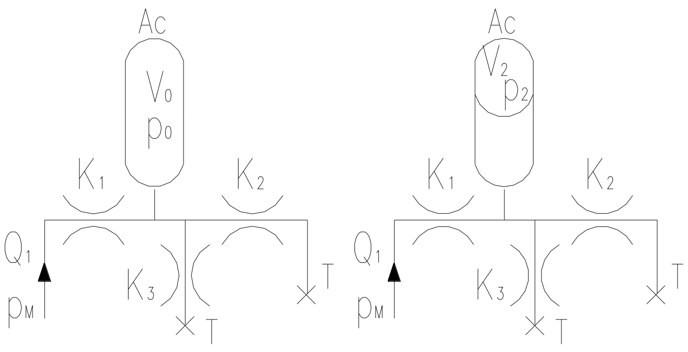

Fig. 4. Initial charge diagram

The charging time can be determined with the relation:

$$t_1 = \frac{\Delta V_1}{K_1\sqrt{p_M - \frac{p_0+p_2}{2}}} \tag{2}$$

The Q_1 flow intended to charge the accumulator results from the pump flow. The difference between them is discharged via the PV pressure valve.

b. Discharge of the accumulator due to losses

Broadly, this situation is shown in Figure 5.

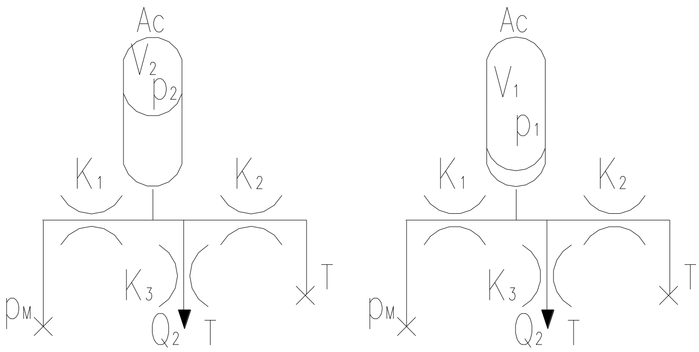

Fig. 5. Discharge diagram due to losses

Oil leaks occur from pressure p_2 until pressure p_1 is reached, which is indicated by the pressure switch PS_1 giving the recharge command.

The lost liquid volume is:

$$\Delta V_2 = \frac{p_0 V_0 (p_2 - p_1)}{p_1 p_2} \tag{3}$$

The time of discharge from pressure p_2 to pressure p_1 has the relation:

$$t_2 = \frac{p_0 V_0 (p_2 - p_1)}{p_1 p_2 K_3 \sqrt{\frac{p_1+p_2}{2}}} \tag{4}$$

The lost flow Q_2 goes to the T tank. At this stage, the pump discharges directly to the tank on the P-A path of the D_1 directional valve.

c. Charging during tightening the tool holder to cover losses from the previous point

For the installation to be effective, this phase should last as short as possible. The charge from pressure p_1 to pressure p_2 must be carried out within a few seconds. Otherwise, the pump will operate at p_M pressure, resulting in high energy consumption, noise and heating of the installation.

For these reasons, in the calculation scheme, shown in Figure 6, the charging is considered to be adiabatic, the adiabatic nitrogen coefficient being $\gamma = 1.4$ [3, 4, 5, 8].

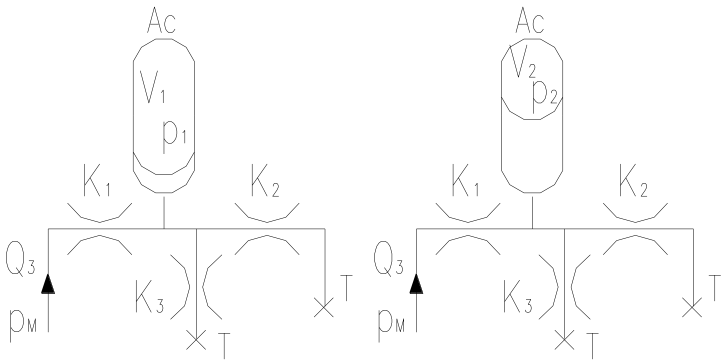

Fig. 6. Charging diagram to cover losses

During charging, a Q_3 flow from the p_M source pressure shall be considered to be sent to the accumulator. The pressure in the accumulator shall be assumed to be constant and equal to the average of the pressures p_1 and p_2.
In this case, the volume of oil sent to the accumulator ΔV_3 will be:

$$\Delta V_3 = \frac{p_0 V_0}{p_1}\left[1 - \left(\frac{p_1}{p_2}\right)^{\frac{1}{\gamma}}\right] \tag{5}$$

The charging time is:

$$t_3 = \frac{\frac{p_0 V_0}{p_1}\left[1 - \left(\frac{p_1}{p_2}\right)^{\frac{1}{\gamma}}\right]}{K_1\sqrt{p_M - \frac{p_1+p_2}{2}}} \tag{6}$$

d. Discharge of the accumulator during the tool holder release phase
In this phase, the directional valves D_1 and D_2 are activated simultaneously. The HPOCV valve opens and the accumulator discharges directly to the tank. The discharge diagram is shown in Figure 7.

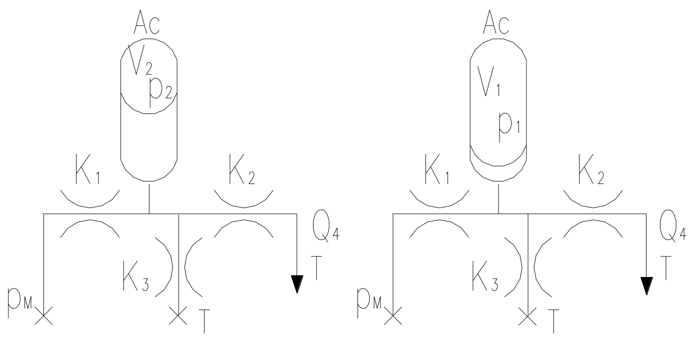

Fig. 7. The discharge diagram of the accumulator in the tool holder release phase

The volume discharged is the one in the relation (3).
The Q_4 flow rate shall be discharged directly to the tank at a t_4 time according to the relation:

$$t_4 = \frac{p_0 V_0 (p_2 - p_1)}{p_1 p_2 K_2 \sqrt{\frac{p_1+p_2}{2}}} \tag{7}$$

The accumulator becomes effective if charging to cover losses is very fast, namely adiabatic. During the remaining phases, the nitrogen in the accumulator can be considered to undergo isothermal changes. The efficiency of the accumulator in these conditions depends on the pump capacity and also on the type and size of the losses.

3. The Simulation of the Operation of the Tool Holder Tightening/Releasing System [10]

The mathematical models presented above allow a theoretical study to be carried out of the influence of the different parameters of the installation on its static operation, after certain simplifications and linearization. It has also been assumed that, when developing such models, losses are negligible during the charging phases of the circuit, which is not actually happening.
Simulation methods may be used for a more detailed study. They can take into account several variable parameters and give information on both static and dynamic behavior of the system.
For example, for the system shown in the hydraulic diagram in Figure 1, the following parameters were considered: minimum pressure (regulated at PS_1 pressure switch) p_1 = 50 bar, maximum pressure (regulated at PS_2 pressure switch) p_2 = 60 bar, maximum working pressure (regulated at PV pressure valve) p_M = 65 bar, the displacement of the pump is 4 cm^3 and is driven by an electric motor with a rated speed of 1500 rpm, the accumulator has a volume of V_0 = 2.5 l and is initially charged with nitrogen at pressure p_0 = 45 bar.
If the system is free of leakage, its initial charging shall be carried out as shown in Figure 8.

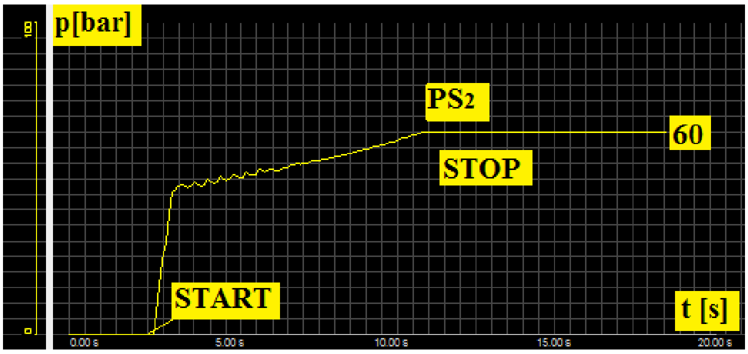

Fig. 8. The characteristic of charging the ideal circuit, loss free

It can be noted that after approximately 11 s the circuit is filled to the pressure p_2 = 60 bar. Charge stopping is controlled by the pressure switch PS_2. Under these conditions, as there are no losses, the pressure is preserved in the accumulator circuit until the tool holder is commanded to release.
For the same parameters, it is then considered that there are circuit losses with an average value of ΔQ = 1 l/min.
The amount of such losses, as seen in Figure 9, is variable. The pump refills the circuit after every delay of approximately 15 s.

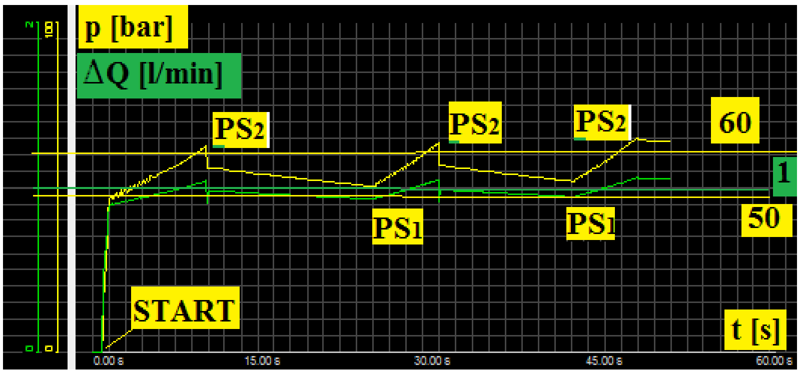

Fig. 9. The circuit charge/discharge characteristic with losses of approximately 1 l/min

The pressure switch PS_2 commands the coupling of the S_1 electromagnet from the directional valve D_1, and the pressure switch SP_1 commands it to be decoupled. If the circuit holds 15 s, the charging lasts for approximately 6 s.
If the losses are higher, e.g., ΔQ ~ 3 l/min, the operating mode of the installation is observed in Figure 10.

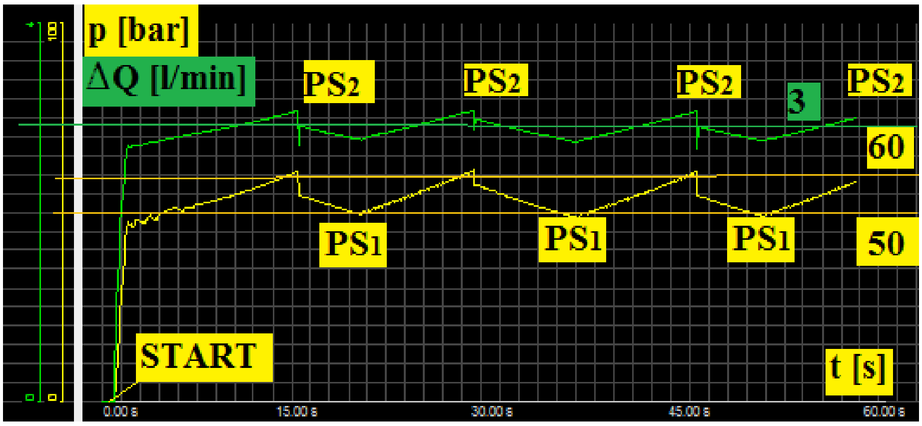

Fig. 10. The circuit charge/discharge characteristic with losses of approximately 3 l/min

In this case, the pressure is maintained only for 6 s after which, for approximately 12 s, it is necessary to couple the S_1 electromagnet. In this case, the pre-control system (i.e., the PV pressure valve and the D_1 directional valve in Figure 1) provided becomes unusable. If the installation is operating under these conditions, the causes of the losses shall be removed.

4. Conclusions

The hydraulic systems designed to tighten and release the tool holders of the machine-tools require high pressure forces. This pressure can be maintained with hydro-pneumatic accumulators. Within certain limits of pressure variations, these accumulators ensure that the systems function properly.
It is recommended that pressure sources include pre-control systems which engage at the minimum pressure and disengage at the maximum pressure required to tighten the tool holder. The pressure source shall be adjusted at a pressure above the maximum pressure required for tightening.
Pressure monitoring can be done discreetly, using pressure switches or continuously, using pressure transducers.
If fluid leaks occur over time, they can be covered by the pressure source - accumulator system. This can be done within certain limits, depending on the loss rate, pump capacity, accumulator capacity and working pressure range.
For a better choice of equipment and design of the installation, it is recommended that simulation methods should also be used before it is carried out.

References

[1] Joshi, P. H. *Machine-Tools Handbook*. New Delhi, McGraw-Hill Publishing House, 2007.
[2] Perovic, Bozina. *Machine-Tools Handbook/Handbuch Werkzeug-Maschinen*. Munchen, Carl Hanser Verlag, 2006.
[3] Bucureşteanu, Anca. *Reserch on the Performance's Growth of the Hydrostatic Drives Systems Using Hydro-Pneumatic Accumulators/Cercetări privind creşterea performanţelor sistemelor hidrostatice de acţionare utilizând acumulatoare pneumohidraulice*. Doctoral Thesis, University POLITEHNICA of Bucharest, 1998.
[4] Bucureşteanu, Anca. *Hydro-Pneumatic Accumulators. Use and Modeling/Acumulatoare pneumohidraulice. Utilizare si modelare*. Bucharest, Printech Publishing House, 2001.
[5] Prodan, Dan, Mircea Duca, Anca Bucureşteanu, and Tiberiu Dobrescu. *Hydrostatic Drives - Machine Parts/Acţionări hidrostatice – Organologie*. Bucharest, AGIR Publishing House, 2005.

[6] Prodan Dan. *Machine-Tools Hydraulics/Hidraulica Masinilor-Unelte*. Bucharest, Printech Publishing House, 2004.
[7] Prodan, Dan, Anca Bucureşteanu, and Emilia Balan. "Using Hydro-Pneumatic Accumulators to Increase the Operation Safety of Heavy-Duty Vertical Lathes." *Applied Mechanics and Materials* 772 (2015): 207-211.
[8] ***. Catalogues and leaflets FOX, PARKER and HYDAC.
[9] Prodan, Dan, and Anca Bucureşteanu. "Determining the Times of Charging and Discharging of Hydro-pneumatic Accumulators." *HIDRAULICA Magazine of Hydraulics, Pneumatics, Tribology, Ecology, Sensorics, Mechatronics*, no. 1 (March 2017): 8-15.
[10] ***. Software package AUTOMATION STUDIO.

ISSN 1453 – 7303 **"HIDRAULICA" (No. 2/2021)**
Magazine *of Hydraulics, Pneumatics, Tribology, Ecology, Sensorics, Mechatronics*

Comparative Study of the Effect of the Compression and Traction Loads on the Stress and Deformation of a Toroidal LPG Tank

Assistant professor PhD. Eng. **Petre OPRIŢOIU**

Technical University of Cluj-Napoca, Department of MTC, Observatorului Street, no. 72-74, Cluj-Napoca, 400363, Cluj county, Romania. Corresponding author* e-mail: petre.opritoiu@mtc.utcluj.ro

Abstract: *The aim of this research is to identify similarities and differences between the stress and deformation behaviors of a three-dimensional (3-D) hexagonal toroid with a regular hexagonal cross-section used in the manufacturing of liquefied petroleum gas (LPG) storage tanks from the automotive industry under compression and traction loads using the finite element simulations. Compression and traction loads applied to the structural design of a storage tank are according to its intended use, size, structure type, materials, design lifetime, in order to assure product safety and to maintain its essential functions. Numerical simulations of the influence of compression, traction loads, and temperature for a given situation considering the 3-D geometry model are used to explain observed phenomena, explore the limitations of various approaches, improved techniques, and technology, and assure the safety of LPG storage tanks. Higher temperature changes and the thermal gradient between the surface layer and the inner layer of material can determine the modification of the mechanical properties of the material and can lead to the formation of fine cracks. The storage tank design model is formulated, according geometrical, mechanical and thermal aspects, to minimize the storage tank mass in terms of thermal performance and safety aspects. The quantitative computational approaches based on the design specifications and standards were used to evaluate the product performance as well as the accuracy of results. The approach proposed by the authors enables a significant reduction in the computational time and makes it possible to perform complex numerical simulations for various 3-D models. The research results besides numerical comparisons, provide a clear basis for interpreting and understanding the relevance of this research method in design of LPG storage tanks.*

Keywords: *3-D hexagonal toroidal LPG fuel tank, compression and traction loads, automotive industry, industrial engineering design, optimization methods, finite element analysis*

1. Introduction

Computer-aided manufacturing (CAM) and computer-aided design (CAD) play a central role in developing the fuel storage tanks market from the automotive industry, to provide high-quality products and to fully satisfy customer needs and expectations [1-3].
In computer-aided design (CAD) of production models [4-7], innovative approaches are needed to satisfy the global market growth, while simultaneously reducing production costs, in correlation with quality requirements and security legislation [8-11].
Three-dimensional (3-D) CAD models not only provide geometry information for different geometrical variants of liquefied petroleum gas (LPG) storage tanks [12-15], but also serve as the basis for module configuration [16-19], as well as for various simulation [20-22], verification processes [23-25] and quality control [24-26].
Finite element analysis (FEA) is a computational tool [27-29] in engineering to design [30-32] and failure analysis to calculate the strength and behavioral characteristics of a material under various conditions, and to investigate large-scale and small-scale behaviors of materials.
This modern tool provides many useful advantages for numerical stress analysis, with an advantage of being applicable to solids of irregular geometry that contain heterogeneous material properties, not for replacements for experimental techniques. Also, the 3-D computational model [33, 34] can be tested under different conditions, under various simple or combined static or dynamic loads, and the simulation results can allow a fast, accurate comparison of numerous results for integrated product development.
In general, computational studies in fluid mechanics [35-38] and heat transfer processes of LPG storage tanks have a major benefit in geometrical optimization [39-42], fluid-structure interaction modelling, and improved product quality.

According to the scientific literature of (LPG) storage tanks, rare studies were devoted to the compression and traction loads of 3-D hexagonal toroid with a regular hexagonal cross-section, or combined deformation behaviors using the finite element simulations.
The objectives of this study are as follows: (1) to develop a simplified 3-D model for the compression and traction loads, (2) to study computationally the role of the main geometric parameters and temperature to give preliminary recommendation on optimization of engineering solutions for manufacturing, (3) to present a numerical solution for realistic case study.

2. Design methodology

2.1. Basic geometry of the parametric 3-D model

Let's consider the parametric 3-D model generated by revolving of a closed generating curve C_G (a hexagon with rounded corners) along a closed guiding curve C_D (a hexagon with rounded corners) as shown in fig. 1 [14].
The following parameters were applied as input parameters to the 3-D parametric model (figs. 1 and 2): a) a closed generating curve CG (a hexagon with a side value L = 175 mm, with rounded corners, radius R = 50 mm), and b) the guiding curve CD (a hexagon with a side value L = 430 mm, with rounded corners, radius R = 180 mm), and the thickness = 10 mm.

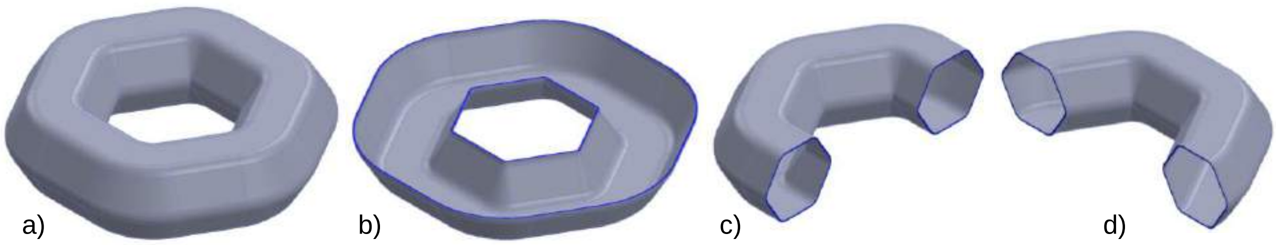

Fig. 1. The isometric representation of non-deformed 3-D model: a) view; b), c) and d) different sections

Based on the physical model, the modeling was done in the AutoCAD Autodesk 2020 software and the numerical analysis was performed with SolidWorks 2020 software with the Static, Thermal and Design Study modules. The design data used were:

- the tank material is AISI 4340 steel;
- the maximum hydraulic test pressure: p_{max} = 30 bar;
- the working temperature between the limits: T = -30 ^{0}C up to T = 60 ^{0}C;
- supporting surfaces located on the inferior side;
- the duration of the tank exploitation: n_a = 15 years;
- the corrosion rate of the material: v_c = 0.07 mm/year.

The numerical analyses of the influence of uniaxial compression and traction loads were studied in references [20, 22], considering for ΔL = 1.33% from the average diameter of the 3-D model, measured in the direction of deformation (figs. 2 and 3).

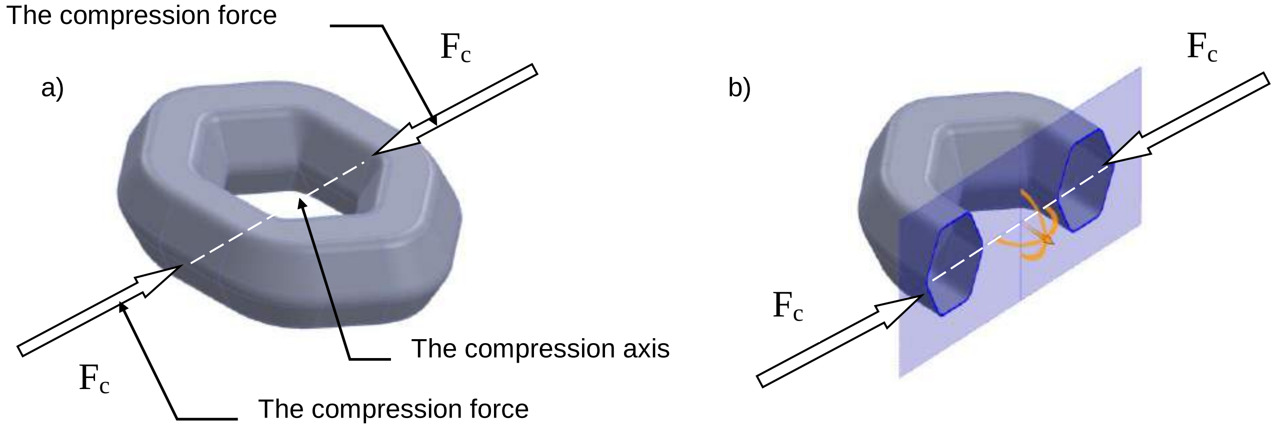

Fig. 2. The isometric representation of deformed 3-D model, after the uniaxial compression:
a) view; b) cross section

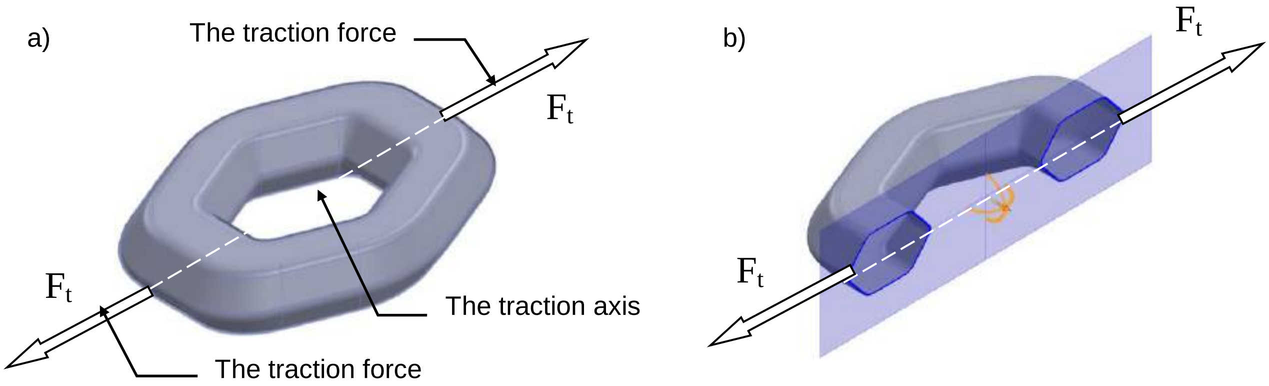

Fig. 3. The isometric representation of deformed 3-D model, after the uniaxial traction: a) view; b) cross section

The uniaxial displacement under compression or traction loads is noted with L_c.

As can be seen in the qualitative deformation of the 3-D model, for the case of compression loads the height of the cross section increases; while for the traction loads, the height of the cross section decreases. Both types of deformations determine directly, additional Von Mises resultant efforts and additonal resulting linear deformations of the 3-D model, greater than the maximum admissible limits of material.
It can be seen that the compression and traction loads are applied normally on the parallel sides of the model by means of the tangent planes (fig. 4 and 5), in addition to the affecting factors (temperature and corrosion process).

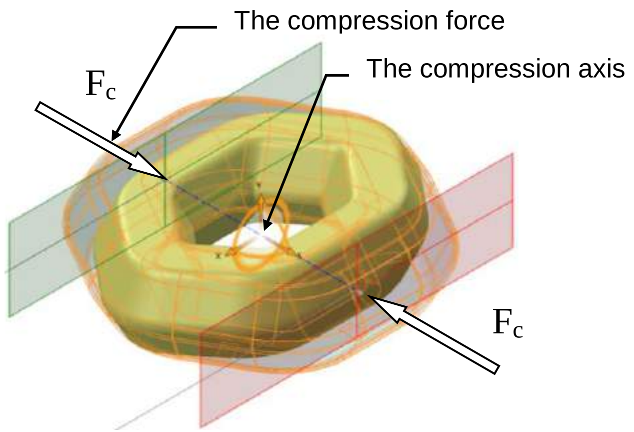

Fig. 4. The isometric representation of 3-D model, deformed, after the uniaxial compression

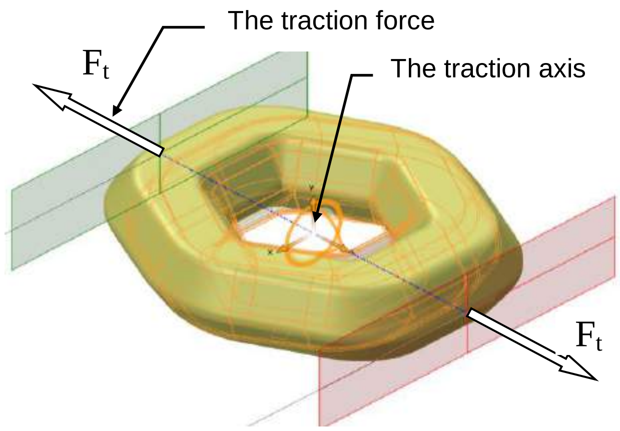

Fig. 5. The isometric representation of 3-D model, deformed, after the uniaxial traction

Numerical calculations were performed for: mesh standard type, solid mesh, curvature-based mesh with quality high, Jacobian in 16 points, element size 11 mm, number of nodes 30628, number of elements 15368. The Von Mises resultant efforts were calculated in both cases of deformations (compression and traction loads) in references [20, 22] and shown in table 1.

Table 1: The Von Mises resultant effort for: T = {-30 ^{0}C, 0 ^{0}C, 30 ^{0}C, 60 ^{0}C} and n_a= {0, 5, 10 and 15 years}

n_a [years]	$L_{c,t}$ [mm]	T [°C]				T [°C]			
		-30°	0°	30°	60°	-30°	0°	30°	60°
		σ_c [MPa] / the compression loads				σ_t [MPa] / the traction loads			
0	0	665.40	565.66	479.29	527.43	665.40	565.66	479.29	527.43
	1	639.82	542.94	515.96	557.23	545.22	470.35	485.68	541.97
	2	627.93	527.30	500.92	546.85	505.58	443.67	466.81	527.46

	3	531.38	467.79	507.29	549.93	521.01	448.29	487.10	540.16
	4	509.47	464.14	508.40	556.37	531.82	457.71	473.33	527.49
	5	589.15	499.13	448.13	452.74	529.59	455.52	488.13	546.48
	6	674.86	570.83	512.66	561.59	524.46	492.94	474.49	531.09
	7	651.59	550.74	504.76	547.34	657.82	559.64	485.78	538.97
	8	525.77	472.30	516.00	563.23	619.07	524.38	468.05	468.05
	9	523.78	529.17	521.79	570.21	523.90	446.61	466.19	521.03
	10	568.13	533.82	498.05	543.62	522.72	444.74	470.08	527.07
5	0	610.22	514.24	511.09	560.58	610.22	514.24	511.09	560.58
	1	532.28	510.09	552.49	598.10	593.51	502.09	506.01	563.14
	2	564.98	521.91	562.62	606.45	534.81	472.72	510.20	556.49
	3	631.33	538.41	557.01	600.40	584.30	502.98	514.43	571.78
	4	678.74	578.54	544.43	591.21	546.24	474.59	525.31	588.70
	5	665.32	564.82	559.06	604.03	565.15	486.81	500.36	558.24
	6	674.56	570.71	512.09	542.58	602.07	524.28	521.33	578.30
	7	679.16	578.01	478.09	488.02	576.45	494.93	478.15	522.33
	8	674.37	570.86	494.20	528.26	704.33	604.23	505.07	559.88
	9	646.48	550.40	559.13	600.81	691.79	591.13	502.17	556.59
	10	649.97	555.16	560.20	596.27	589.18	514.04	507.66	568.22
10	0	656.26	615.97	591.97	641.72	656.26	615.97	591.97	641.72
	1	566.98	568.67	606.88	647.44	718.61	623.72	586.50	632.99
	2	577.49	580.21	623.99	670.84	585.76	509.56	535.62	587.22
	3	680.81	585.12	611.01	658.16	591.81	516.25	567.98	623.54
	4	690.24	589.25	601.49	655.87	722.39	623.49	525.83	545.66
	5	703.44	600.73	635.70	675.09	602.64	531.32	576.29	642.99
	6	698.80	601.83	608.11	652.30	737.04	738.28	740.10	742.49
	7	677.61	593.07	639.09	690.45	587.54	510.56	528.33	559.51
	8	657.19	565.88	533.39	570.39	683.04	585.06	555.56	609.76
	9	589.70	547.00	578.70	613.37	584.59	509.34	584.59	585.40
	10	581.48	563.95	606.61	652.00	581.63	505.67	511.08	561.02
15	0	754.50	655.70	636.94	688.12	754.50	655.70	636.94	688.12
	1	760.74	661.69	677.69	720.92	680.88	589.79	591.14	638.86
	2	733.97	630.11	636.39	671.18	760.61	669.24	628.56	679.21
	3	608.07	618.41	658.21	700.28	657.33	583.00	643.56	708.33
	4	618.59	636.51	681.17	728.32	640.55	566.19	600.51	644.61
	5	644.32	579.84	618.48	662.06	660.04	586.78	622.83	658.88
	6	633.14	632.84	599.81	627.73	602.60	572.32	634.55	700.08
	7	640.52	627.79	669.36	713.72	636.33	567.02	565.91	573.71
	8	667.74	655.60	703.00	754.60	695.16	592.73	556.54	591.79
	9	624.54	623.04	667.02	713.53	789.42	683.81	579.95	597.50
	10	599.76	618.13	661.29	707.00	735.27	637.78	542.83	590.54

2.2. Numerical analysis of the parametric 3-D model

The graphs of curves corresponding to the Von Mises resultant efforts $\sigma_{c,t}$ (L_c, T) are graphically shown in fig. 6, for n_a = {0, 5, 10, and 15 years} and T = {-30 ^{0}C, 0 ^{0}C, 30 ^{0}C, 60 ^{0}C}.

Fig. 6 The graphs of the Von Mises resultant efforts with highlighted details:
(T = 60 ^{0}C; n_a= {0, 5, 10 and 15 years}; T = {-30 ^{0}C, 0 ^{0}C, 30 ^{0}C, 60 ^{0}C}})

The 3-D graphs corresponding to the Von Mises resultant efforts $\sigma_{c,t}$ (L_c, T) taking into account the results from table 1 are graphically shown in figs. 7-10, respectively.

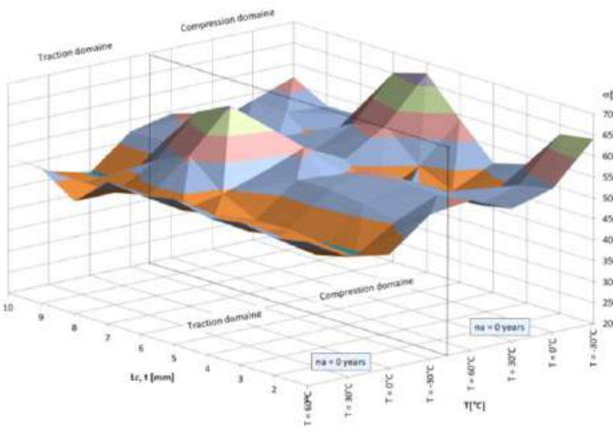

Fig. 7. The graphs of σ = f(L_c, T) for n_a = 0 years left (traction domain); right (compression domain)

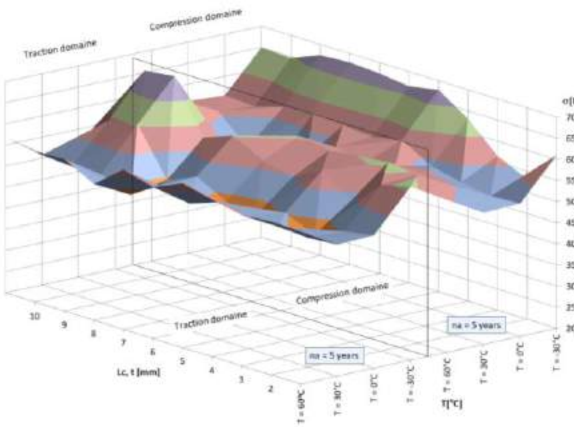

Fig. 8. The graphs of σ = f(L_c, T) for n_a = 5 years left (traction area); right (compression area)

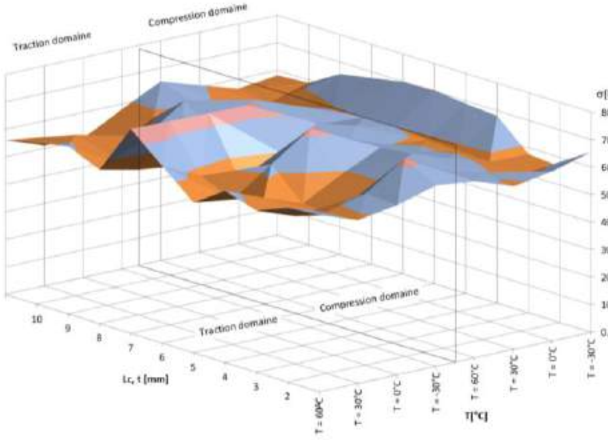

Fig. 9. The graphs of σ = f(L_c, T) for n_a = 10 years left (traction domain); right (compression domain)

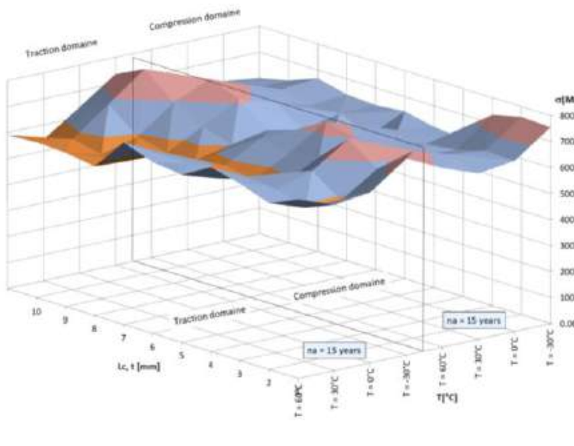

Fig. 10. The graphs of σ = f(L_c, T) for n_a = 15 years left (traction area); right (compression area)

The graphs of curves $\sigma = f(L_c, T)$ with these highlighted details are shown in figs. 11-14.

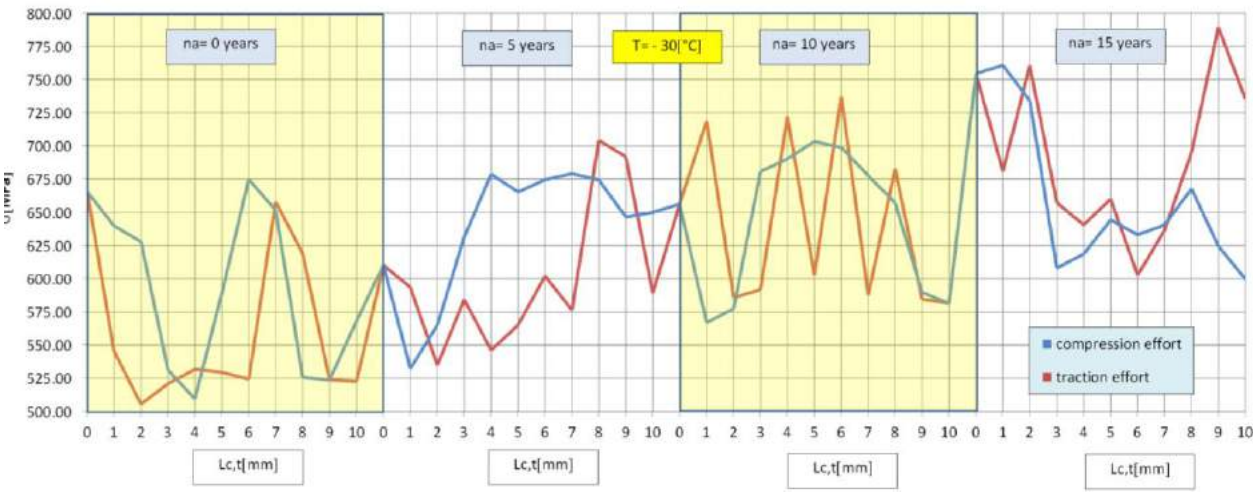

Fig. 11. The graphs of the Von Mises resultant efforts $\sigma = f(L_c, T)$ with highlighted details:
(T = -30 ^{0}C; n_a= {0, 5, 10 and 15 years}; blue curve – the compression effort; red curve – the traction effort;

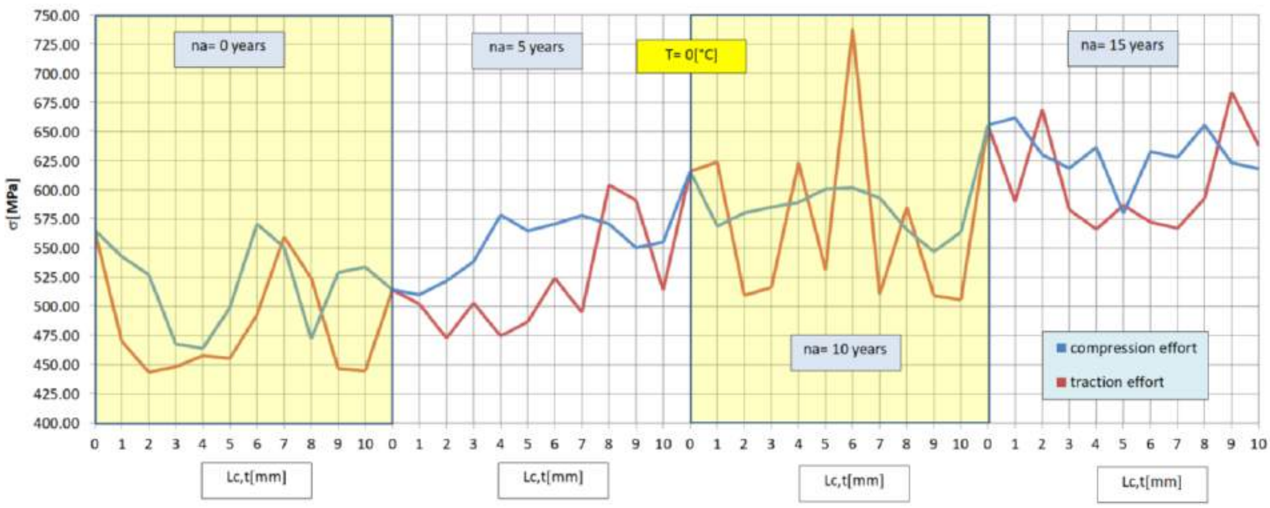

Fig. 12. The graphs of the Von Mises resultant efforts $\sigma = f(L_c, T)$ with highlighted details:
(T = 0 ^{0}C; n_a= {0, 5, 10 and 15 years}; blue curve – the compression effort; red curve – the traction effort;

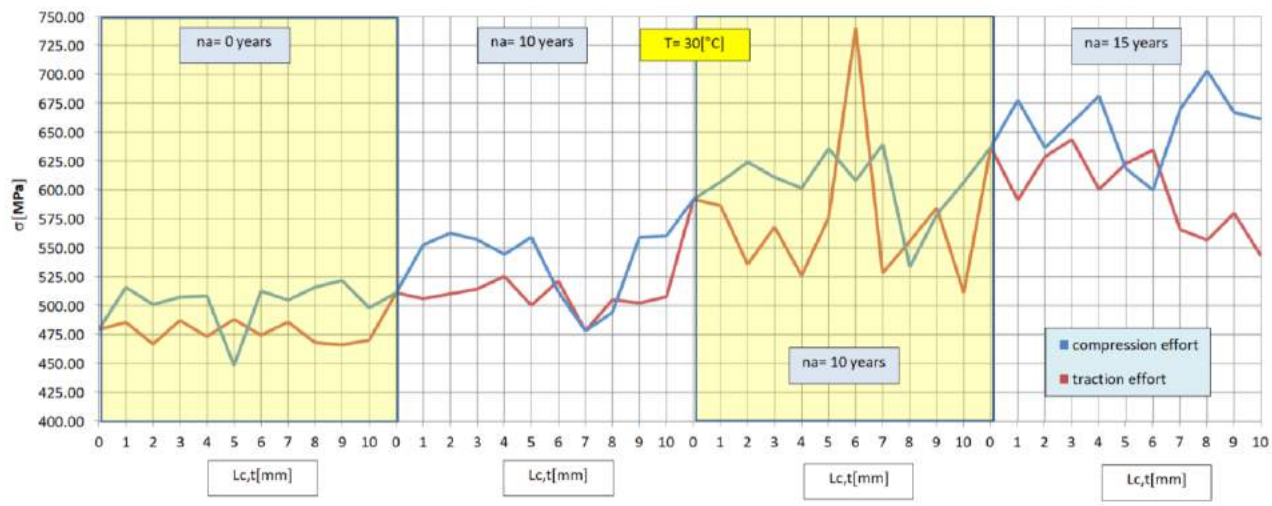

Fig. 13. The graphs of the Von Mises resultant efforts $\sigma = f(L_c, T)$ with highlighted details:
(T = 10 ^{0}C; n_a= {0, 5, 10 and 15 years}; blue curve – the compression effort; red curve – the traction effort;

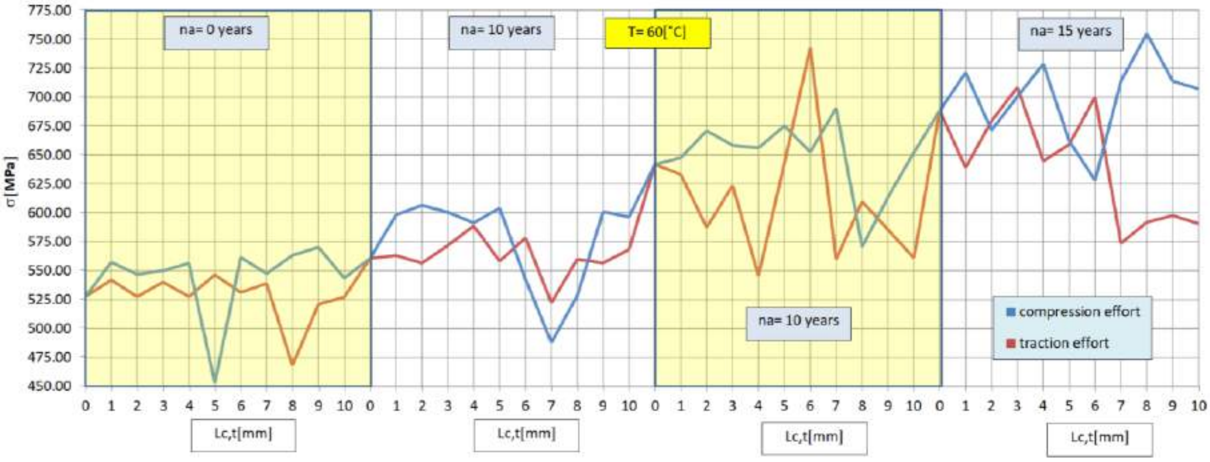

Fig. 14. The graphs of the Von Mises resultant efforts $\sigma = f(L_c, T)$ with highlighted details: ($T = 60\ ^0C$; $n_a = \{0, 5, 10$ and 15 years$\}$; blue curve – the compression effort; red curve – the traction effort.

It was calculated the percentage variation of the Von Mises effort $\Delta\sigma$ (L_c, T) given by compression versus the resulting stress state given by traction, using the following formula:

$$\Delta\sigma = \frac{(\sigma_c - \sigma_t)}{\sigma_t} \cdot 100\ [\%] \qquad (1)$$

The percentage variation of Von Mises resultant effort $\Delta\sigma$ was computed in table 2 and the corresponding graphs (in 2-D) are shown in fig. 15.

Table 2: The percentage variation ($\Delta\sigma$) of the Von Mises effort for: $T = \{-30\ ^0C, 0\ ^0C, 30\ ^0C, 60\ ^0C\}$ and $n_a = \{0, 5, 10$ and 15 years$\}$

$L_{c,t}$ [mm]	T [°C]				T [°C]			
	-30°	0°	30°	60°	-30°	0°	30°	60°
	Δσ [MPa]				Δσ [MPa]			
	n_a = 0 [years]				n_a = 5 [years]			
1	17.35	15.43	6.23	2.82	-10.32	1.59	9.19	6.21
2	24.20	18.85	7.31	3.68	5.64	10.41	10.27	8.98
3	1.99	4.35	4.14	1.81	8.05	7.05	8.28	5.01
4	-4.20	1.40	7.41	5.48	24.26	21.90	3.64	0.43
5	11.25	9.57	-8.19	-17.15	17.72	16.03	11.73	8.20
6	28.68	15.80	8.05	5.74	12.04	8.86	-1.77	-6.18
7	-0.95	-1.59	3.91	1.55	17.82	16.79	-0.01	-6.57
8	-15.07	-9.93	10.24	20.33	-4.25	-5.52	-2.15	-5.65
9	-0.02	18.49	11.93	9.44	-6.55	-6.89	11.34	7.94
10	8.69	20.03	5.95	3.14	10.32	8.00	10.35	4.94
	n_a = 10 [years]				n_a = 15 [years]			
1	-21.10	-8.83	3.47	2.28	11.73	12.19	14.64	12.85
2	-1.41	13.86	16.50	14.24	-3.50	-5.85	1.24	-1.18
3	15.04	13.34	7.58	5.55	-7.49	6.07	2.28	-1.14
4	-4.45	-5.49	14.39	20.20	-3.43	12.42	13.43	12.99
5	16.73	13.06	10.31	4.99	-2.38	-1.18	-0.70	0.48
6	-5.19	-18.48	-17.83	-12.15	5.07	10.57	-5.48	-10.33
7	15.33	16.16	20.96	23.40	0.66	10.72	18.28	24.41
8	-3.79	-3.28	-3.99	-6.46	-3.94	10.61	26.32	27.51
9	0.87	7.40	-1.01	4.78	-20.89	-8.89	15.01	19.42
10	-0.03	11.53	18.69	16.22	-18.43	-3.08	21.82	19.72

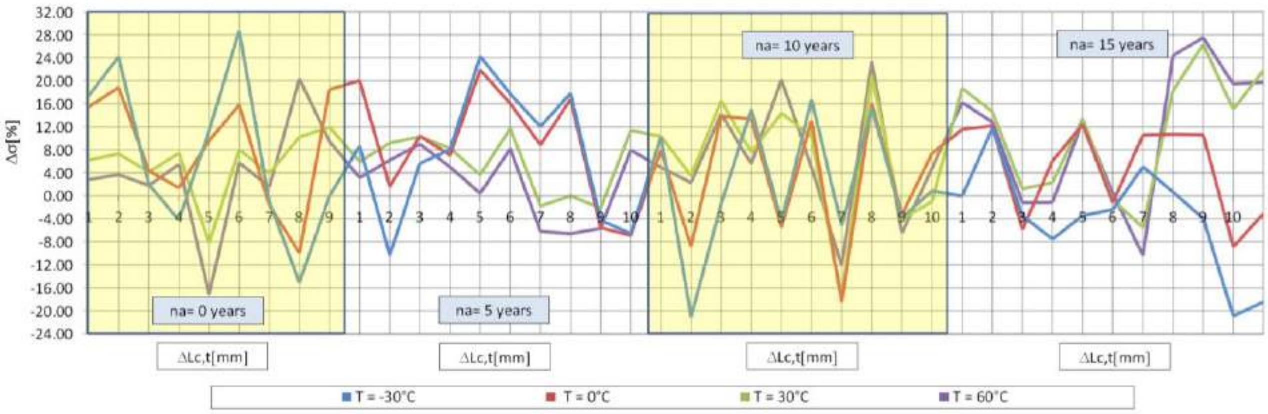

Fig. 15. The graphs of $\Delta\sigma$ (L_c, T) for: T = {-30 ^{0}C, 0 ^{0}C, 30 ^{0}C, 60 ^{0}C} and n_a= {0, 5, 10 and 15 years}

The values of the resultant linear deformation *u* determined by compression and traction for n_a= {0, 5, 10 and 15 years} are shown in table 3.

Table 3: The resultant linear deformations *u* for: T = {-30 ^{0}C, 0 ^{0}C, 30 ^{0}C, 60 ^{0}C} and n_a= {0, 5, 10, 15 years}

n_a [years]	$L_{c,t}$ [mm]	T [°C]				T [°C]			
		-30°	0°	-30°	0°	-30°	0°	-30°	0°
		u_c [mm] / the compression loads				u_t [mm] / the traction loads			
0	0	0.869	0.837	0.805	0.777	0.869	0.837	0.805	0.777
	1	0.695	0.704	0.715	0.728	0.652	0.660	0.671	0.685
	2	0.675	0.683	0.693	0.704	0.596	0.603	0.612	0.622
	3	0.673	0.681	0.690	0.700	0.619	0.628	0.638	0.651
	4	0.656	0.664	0.673	0.684	0.622	0.631	0.642	0.656
	5	0.635	0.626	0.619	0.614	0.624	0.628	0.634	0.641
	6	0.623	0.632	0.645	0.659	0.618	0.626	0.637	0.650
	7	0.669	0.676	0.685	0.694	0.618	0.624	0.634	0.646
	8	0.654	0.661	0.670	0.680	0.598	0.604	0.611	0.611
	9	0.636	0.644	0.655	0.666	0.602	0.609	0.617	0.629
	10	0.671	0.678	0.686	0.696	0.614	0.621	0.631	0.642
5	0	0.938	0.904	0.871	0.841	0.938	0.904	0.871	0.841
	1	0.761	0.769	0.780	0.793	0.709	0.715	0.724	0.733
	2	0.728	0.736	0.745	0.757	0.675	0.683	0.693	0.705
	3	0.727	0.735	0.745	0.757	0.672	0.678	0.686	0.695
	4	0.708	0.712	0.720	0.730	0.700	0.711	0.723	0.736
	5	0.697	0.702	0.709	0.718	0.685	0.692	0.700	0.711
	6	0.720	0.719	0.719	0.720	0.675	0.682	0.691	0.703
	7	0.727	0.720	0.713	0.706	0.644	0.636	0.632	0.639
	8	0.718	0.707	0.699	0.696	0.671	0.679	0.689	0.700
	9	0.687	0.695	0.704	0.714	0.698	0.701	0.707	0.713
	10	0.693	0.699	0.707	0.719	0.699	0.703	0.710	0.717
10	0	1.011	0.974	0.944	0.916	1.011	0.974	0.944	0.916
	1	0.836	0.845	0.855	0.866	0.840	0.842	0.845	0.851
	2	0.805	0.815	0.825	0.837	0.711	0.715	0.721	0.729
	3	0.807	0.816	0.826	0.839	0.737	0.748	0.761	0.776
	4	0.805	0.811	0.819	0.828	0.731	0.729	0.735	0.743
	5	0.791	0.796	0.807	0.817	0.754	0.761	0.770	0.780
	6	0.784	0.790	0.797	0.807	0.748	0.744	0.741	0.739
	7	0.788	0.796	0.80	0.814	0.708	0.710	0.714	0.722
	8	0.795	0.793	0.795	0.802	0.755	0.752	0.759	0.769
	9	0.797	0.789	0.783	0.779	0.799	0.788	0.799	0.769
	10	0.804	0.811	0.820	0.831	0.761	0.763	0.766	0.771

15	0	1.106	1.076	1.047	1.020	1.106	1.076	1.047	1.020
	1	0.927	0.933	0.941	0.952	0.872	0.869	0.867	0.800
	2	0.887	0.891	0.887	0.884	0.788	0.791	0.797	0.805
	3	0.905	0.914	0.924	0.935	0.777	0.787	0.799	0.812
	4	0.873	0.882	0.893	0.905	0.834	0.837	0.842	0.849
	5	0.843	0.835	0.829	0.831	0.829	0.835	0.843	0.851
	6	0.882	0.873	0.872	0.877	0.808	0.813	0.820	0.830
	7	0.932	0.938	0.948	0.960	0.792	0.783	0.774	0.768
	8	0.871	0.879	0.888	0.898	0.805	0.804	0.806	0.812
	9	0.833	0.839	0.847	0.855	0.812	0.805	0.802	0.800
	10	0.899	0.904	0.910	0.917	0.842	0.836	0.830	0.824

The graphs of curves (in 2-D) corresponding to the resultant linear deformation u = (L_c, T) for n_a = {0, 5, 10 and 15 years}; are graphically shown in fig. 16, while the corresponding graphs (in 3-D) are shown figs. 17-21.

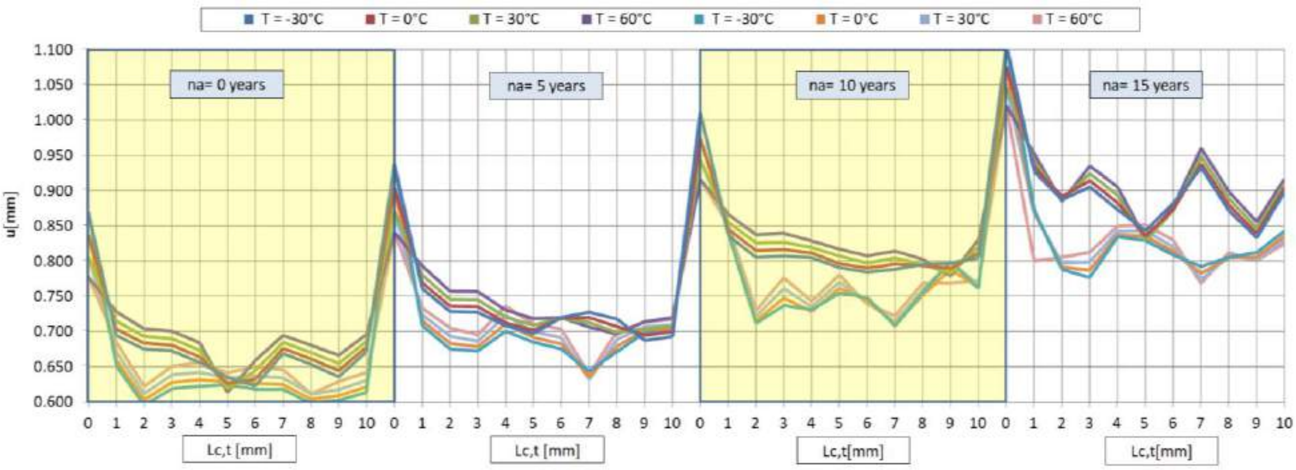

Fig. 16. The graphs of u = ($L_{c,t}$, T) for: T = {-30 ^{0}C, 0 ^{0}C, 30 ^{0}C, 60 ^{0}C} and n_a= {0, 5, 10 and 15 years}

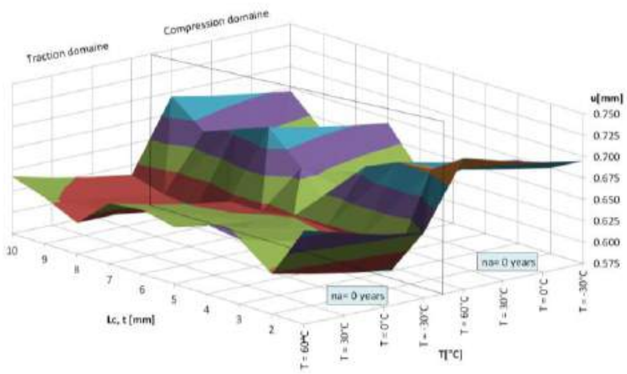

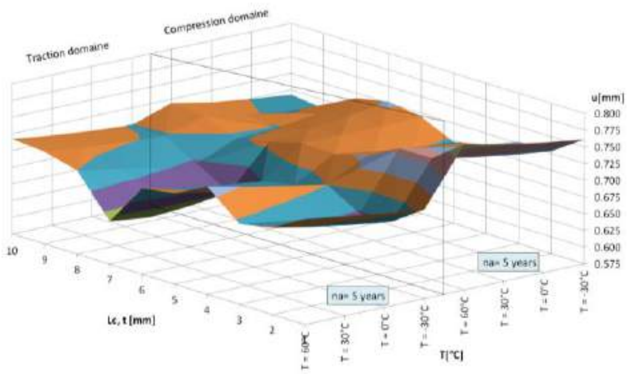

Fig. 17. The graphs of u = (L_c, T) for n_a = 0 years left (traction domain); right (compression domain)

Fig. 18. The graphs of u = (L_c, T) for n_a = 5 years left (traction area); right (compression area)

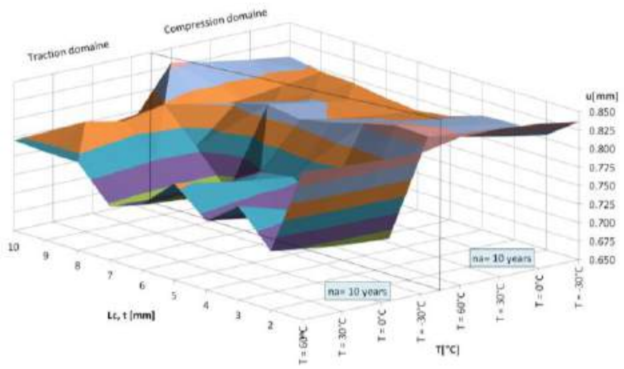

Fig. 19. The graphs of u = (L_c, T) for n_a = 10 years left (traction domain); right (compression domain)

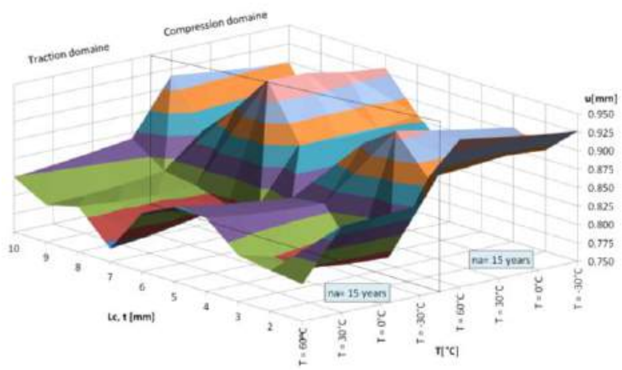

Fig. 20. The graphs of u = (L_c, T) for n_a = 15 years left (traction area); right (compression area)

The graphs of curves u = (L_c, T) with these highlighted details are shown in figs. 21-24.

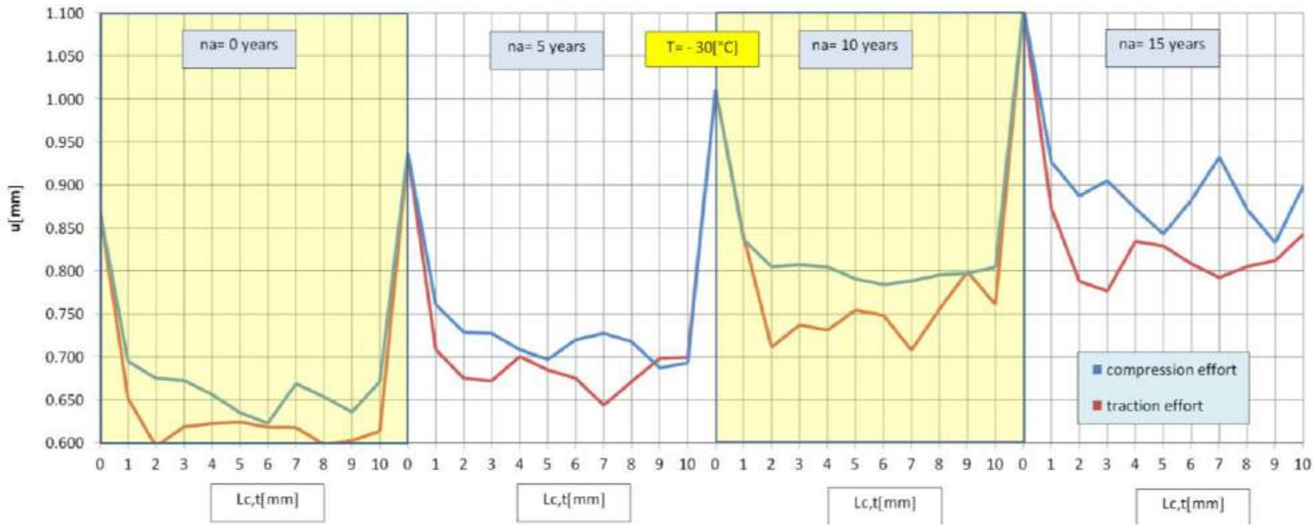

Fig. 21. The graphs of the resulting linear deformations u = f(L_c, T) with highlighted details: (T = -30 ^{0}C; n_a= {0, 5, 10 and 15 years}; blue curve – the compression effort; red curve – the traction effort;

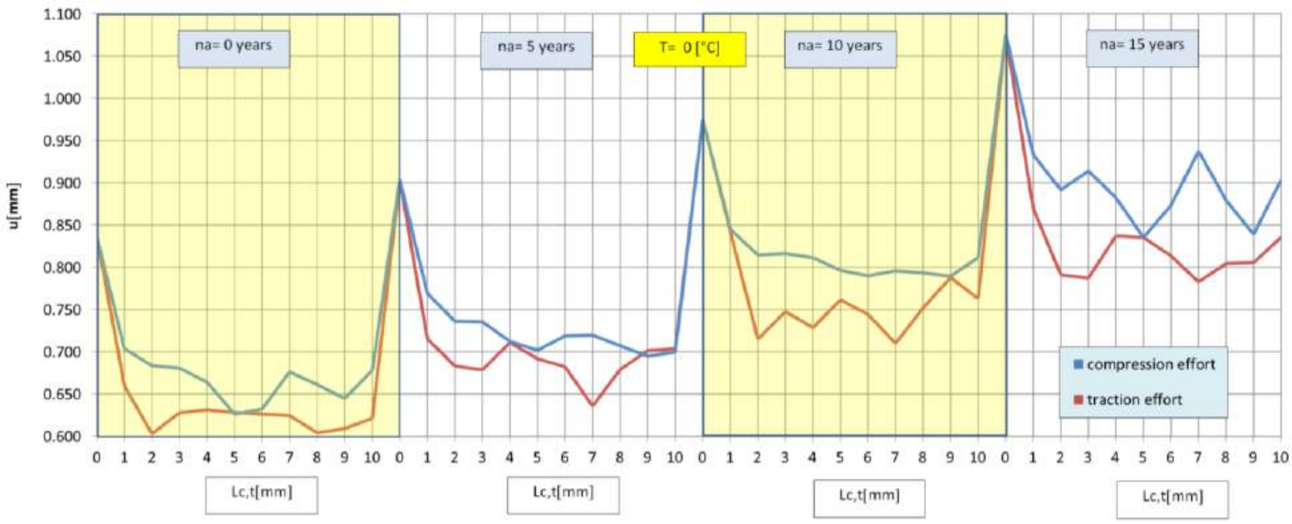

Fig. 22. The graphs of the resulting linear deformations u = f(L_c, T) with highlighted details: (T = 0 ^{0}C; n_a= {0, 5, 10 and 15 years}; blue curve – the compression effort; red curve – the traction effort;

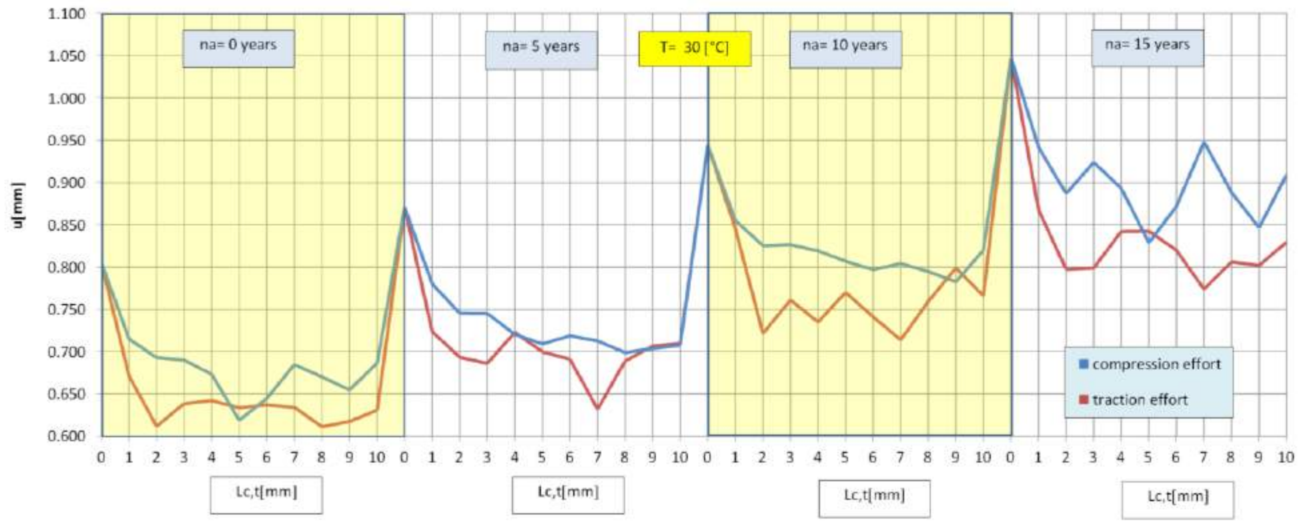

Fig. 23. The graphs of the resulting linear deformations *u* = f(L_c, T) with highlighted details: (T = 30 ^{0}C; n_a= {0, 5, 10 and 15 years}; blue curve – the compression effort; red curve – the traction effort;

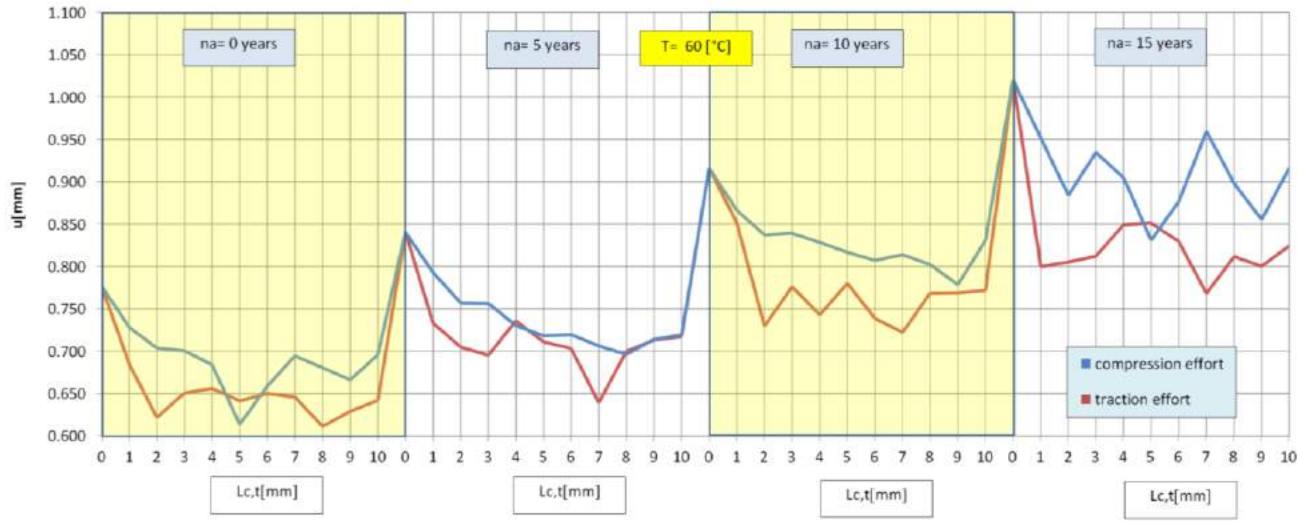

Fig. 24. The graphs of the resulting linear deformations *u* = f(L_c, T) with highlighted details: (T = 60 ^{0}C; n_a= {0, 5, 10 and 15 years}; blue curve – the compression effort; red curve – the traction effort;

It was calculated the percentage variation of the resultant linear deformation Δu (L_c, T) given by compression versus the resulting stress state given by traction, using the following formula:

$$\Delta u = \frac{(u_c - u_t)}{u_t} \cdot 100 \; [\%] \quad (1)$$

The percentage variation of Von Mises resultant effort Δu was computed in table 4 and the corresponding graphs (in 2-D) are shown in fig. 25.

Table 4: The percentage variation of resultant liniar deformation Δu for: T = {-30 ^{0}C, 0 ^{0}C, 30 ^{0}C, 60 ^{0}C} and n_a= {0, 5, 10 and 15 years}

$L_{c,t}$ [mm]	T [°C]				T [°C]			
	-30°	0°	-30°	0°	-30°	0°	-30°	0°
	Δu [mm]				Δu [mm]			
	n_a = 0 [years]				n_a = 5 [years]			
1	6.62	6.65	6.51	6.35	7.41	7.52	7.81	8.16
2	13.31	13.36	13.29	13.17	7.92	7.75	7.52	7.38

3	8.72	8.42	8.06	7.66	8.19	8.40	8.60	8.82
4	5.48	5.18	4.87	4.26	1.14	0.18	-0.35	-0.78
5	1.73	-0.31	-2.37	-4.34	1.78	1.47	1.34	1.02
6	0.76	0.93	1.23	1.37	6.62	5.36	4.01	2.30
7	8.26	8.26	7.96	7.52	13.01	13.22	12.77	10.53
8	9.30	9.47	9.65	11.34	6.90	4.16	1.46	-0.52
9	5.53	5.81	6.04	5.90	-1.56	-0.93	-0.42	0.13
10	9.40	9.17	8.83	8.38	-0.94	-0.58	-0.30	0.29
	n_a = 10 [years]				n_a = 15 [years]			
1	-0.44	0.35	1.16	1.78	6.22	7.31	8.53	18.99
2	13.17	13.96	14.43	14.78	12.63	12.71	11.24	9.79
3	9.51	9.17	8.58	8.11	16.53	16.12	15.66	15.09
4	10.08	11.35	11.44	11.50	4.58	5.40	6.03	6.54
5	4.79	4.57	4.78	4.69	1.66	0.00	-1.64	-2.37
6	4.80	6.14	7.55	9.28	9.15	7.36	6.32	5.70
7	11.39	12.10	12.66	12.70	17.71	19.82	22.57	24.99
8	5.25	5.51	4.65	4.39	8.18	9.29	10.14	10.65
9	-0.24	0.19	-2.05	1.26	2.58	4.18	5.58	6.88
10	5.71	6.37	7.06	7.67	6.66	8.14	9.65	11.18

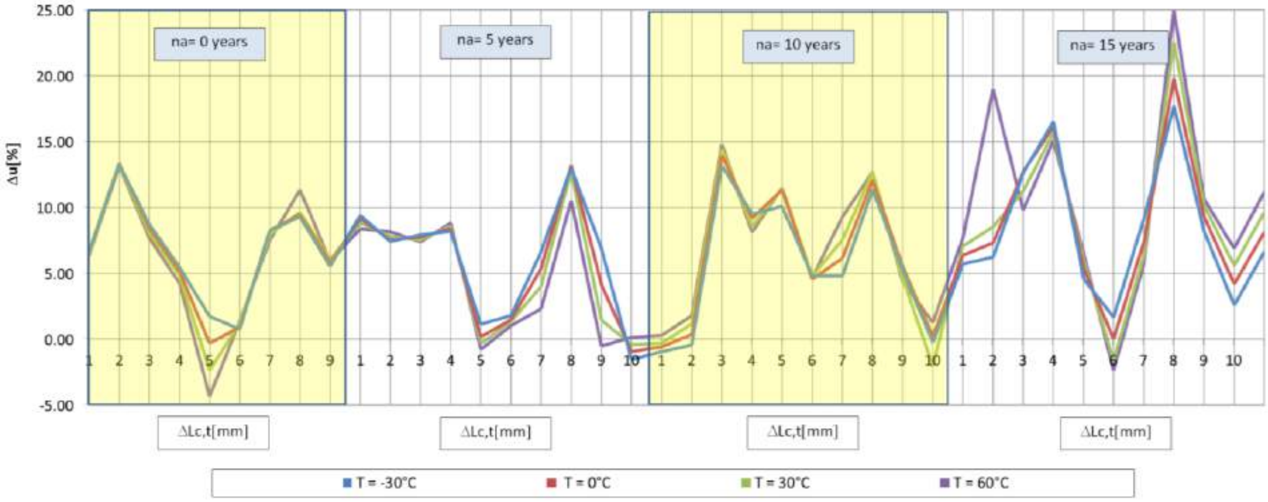

Fig. 25. The graphs of Δu (L_c, T) for: T = {-30 ^{0}C, 0 ^{0}C, 30 ^{0}C, 60 ^{0}C} and n_a= {0, 5, 10 and 15 years}

3. Conclusions

Following the numerical analyses and the resulting graphs it has been found that:
- the state of deformations are amplified with the increase of compression and traction loads;
- the state of efforts are amplified with the increase of compression and traction loads, and by the decreasing of the working temperature;
- for the compression loads, n_a= 15 years, T = -30 ^{0}C, σ_{max} = 760.64 MPa > σ_a = 710 MPa, and L_c = 2 mm;
- the percentage variation of Von Mises resultant effort ($\Delta\sigma$) for the compression loads is greater with $\Delta\sigma$ = 28.68% than the traction loads;
- the values of the resultant linear deformation *u* for compression loads are greater than traction loads. Also, the resultant linear deformation *u* is amplified with the increase of the working period;
- the resultant linear deformation (u) for the compression loads is greater than the traction loads and is amplified with the increase of the working period;
- the percentage variation of resultant linear deformation (Δu) is greater with Δu = 25 [%] for the compression loads is greater than the traction loads;
- it can be appreciated that the most disadvantageous state of stresses appears in case the compression loads.

References

[1] Ghiţă, C. Mirela, Anton C. Micu, Mihai Ţălu and Ştefan Ţălu. "Shape optimization of a thoroidal methane gas tank for automotive industry." *Annals of Faculty of Engineering Hunedoara - International Journal of Engineering, Hunedoara, Romania*, Tome X, Fascicule 3 (2012): 295-297.
[2] Ghiţă, C. Mirela, Anton C. Micu, Mihai Ţălu and Ştefan Ţălu. "Shape optimization of vehicle's methane gas tank." *Annals of Faculty of Engineering Hunedoara - International Journal of Engineering, Hunedoara, Romania*, Tome X, Fascicule 3 (2012): 259-266.
[3] Ghiţă, C. Mirela, Anton C. Micu, Mihai Ţălu, Ştefan Ţălu and Ema I. Adam. "Computer-Aided Design of a classical cylinder gas tank for the automotive industry." *Annals of Faculty of Engineering Hunedoara - International Journal of Engineering, Hunedoara*, *Romania*, Tome XI, Fascicule 4 (2013): 59-64.
[4] Ghiţă, C. Mirela, Anton C. Micu, Mihai Ţălu and Ştefan Ţălu. "3D modelling of a shrink fitted concave ended cylindrical tank for automotive industry." *Acta Technica Corviniensis – Bulletin of Engineering, Hunedoara, Romania*, Tome VI, Fascicule 4 (2013): 87-92.
[5] Ghiţă, C. Mirela, Anton C. Micu, Mihai Ţălu and Ştefan Ţălu. "3D modelling of a gas tank with reversed end up covers for automotive industry." *Annals of Faculty of Engineering Hunedoara - International Journal of Engineering, Hunedoara*, *Romania*, Tome XI, Fascicule 3 (2013): 195-200.
[6] Ghiţă, C. Mirela, Ştefan C. Ghiță, Ştefan Ţălu and Simona Rotaru. "Optimal design of cylindrical rings used for the shrinkage of vehicle tanks for compressed natural gas." *Annals of Faculty of Engineering Hunedoara - International Journal of Engineering, Hunedoara*, Tome XII, Fascicule 3 (2014): 243-250.
[7] Vintilă, Daniela, Mihai Ţălu and Ştefan Ţălu. "The CAD analyses of a torospheric head cover of a pressurized cylindrical fuel tank after the crash test." *Magazine of Hydraulics, Pneumatics, Tribology, Ecology, Sensorics, Mechatronics (HIDRAULICA)*, no. 4 (December 2017): 57-66.
[8] Bică, Marin, Mihai Ţălu and Ştefan Ţălu. "Optimal shapes of the cylindrical pressurized fuel tanks." *Magazine of Hydraulics, Pneumatics, Tribology, Ecology, Sensorics, Mechatronics (HIDRAULICA)*, no. 4 (December 2017): 6-17.
[9] Ţălu, Mihai. "The influence of the corrosion and temperature on the Von Mises stress in the lateral cover of a pressurized fuel tank." *Magazine of Hydraulics, Pneumatics, Tribology, Ecology, Sensorics, Mechatronics (HIDRAULICA)*, no. 4 (December 2017): 89-97.
[10] Ţălu, Ştefan and Mihai Ţălu. "The influence of deviation from circularity on the stress of a pressurized fuel cylindrical tank." *Magazine of Hydraulics, Pneumatics, Tribology, Ecology, Sensorics, Mechatronics (HIDRAULICA)*, no. 4 (December 2017): 34-45.
[11] Ţălu, Mihai and Ştefan Ţălu. "Design and optimization of pressurized toroidal LPG fuel tanks with variable section." *Magazine of Hydraulics, Pneumatics, Tribology, Ecology, Sensorics, Mechatronics (HIDRAULICA)*, no. 1 (March 2018): 32-41.
[12] Ţălu, Mihai and Ştefan Ţălu. "Analysis of temperature resistance of pressurized cylindrical fuel tanks." *Magazine of Hydraulics, Pneumatics, Tribology, Ecology, Sensorics, Mechatronics (HIDRAULICA)*, no. 1 (March 2018): 6-15.
[13] Ţălu, Ştefan and Mihai Ţălu. "Algorithm for optimal design of pressurized toroidal LPG fuel tanks with constant section described by imposed algebraic plane curves." *Magazine of Hydraulics, Pneumatics, Tribology, Ecology, Sensorics, Mechatronics (HIDRAULICA)*, no. 2 (June 2018): 14-21.
[14] Ţălu, Mihai and Ştefan Ţălu. "The optimal CAD design of a 3D hexagonal toroid with regular hexagonal cross-section used in manufacturing of LPG storage tanks." *Magazine of Hydraulics, Pneumatics, Tribology, Ecology, Sensorics, Mechatronics (HIDRAULICA)*, no. 2 (June 2018): 49-56.
[15] Ţălu, Mihai and Ştefan Ţălu. "The influence of corrosion and temperature variation on a CNG storage tank with a combined form consisting of a torus and a sphere." *Magazine of Hydraulics, Pneumatics, Tribology, Ecology, Sensorics, Mechatronics (HIDRAULICA)*, no. 4 (December 2019): 93-104.
[16] Ţălu, Mihai and Ştefan Ţălu. "Optimal design of a CNG storage tank with a combined form consisting of a torus and a sphere." *Magazine of Hydraulics, Pneumatics, Tribology, Ecology, Sensorics, Mechatronics (HIDRAULICA)*, no. 4 (December 2019): 73-82.
[17] Ţălu, Mihai and Ştefan Ţălu. "The influence of corrosion and temperature variation on the minimum safety factor of a 3D hexagonal toroid with regular hexagonal cross-section used in manufacturing of LPG storage tanks." *Magazine of Hydraulics, Pneumatics, Tribology, Ecology, Sensorics, Mechatronics (HIDRAULICA)*, no. 3 (September 2018): 16-25.
[18] Ţălu, Ştefan and Mihai Ţălu. "The influence of corrosion and pressure variation on the minimum safety factor of a 3D hexagonal toroid with regular hexagonal cross-section used in manufacturing of LPG storage tanks." *Magazine of Hydraulics, Pneumatics, Tribology, Ecology, Sensorics, Mechatronics (HIDRAULICA)*, no. 3 (September 2018): 39-45.
[19] Ţălu, Mihai and Ştefan Ţălu. "Study of temperature–corrosion–torsion affecting factors on the shape of a toroidal LPG tank using the finite element method." *Magazine of Hydraulics, Pneumatics, Tribology, Ecology, Sensorics, Mechatronics (HIDRAULICA)*, no. 1 (March 2020): 21-32.

[20] Ţălu, Ştefan and Mihai Ţălu. "Numerical analysis of the influence of uniaxial compression loads on the shape of a toroidal LPG tank." *Magazine of Hydraulics, Pneumatics, Tribology, Ecology, Sensorics, Mechatronics (HIDRAULICA)*, no. 1 (March 2020): 47-58.
[21] Ţălu, Mihai and Ştefan Ţălu. "Stress and deformation analysis under bending and torsional loads of a toroidal LPG tank based on the finite element analysis." *Magazine of Hydraulics, Pneumatics, Tribology, Ecology, Sensorics, Mechatronics (HIDRAULICA)*, no. 1 (March 2020): 88-101.
[22] Oprițoiu, Petre. "Analysis of uniaxial traction loads on the 3-D geometry of a toroidal LPG storage tank." *Magazine of Hydraulics, Pneumatics, Tribology, Ecology, Sensorics, Mechatronics (HIDRAULICA)*, no. 2 (June 2020): 15-26.
[23] Ţălu, Ştefan and Mihai Ţălu. "Constructive CAD variants of toroidal LPG fuel tanks used in automotive Industry." *Advances in Intelligent Systems Research* 159 (2018): 27-30. DOI: 10.2991/mmsa-18.2018.7.
[24] Ţălu, Mihai and Ştefan Ţălu. "3D geometrical solutions for toroidal LPG fuel tanks used in automotive industry." *Advances in Intelligent Systems Research* 151 (2018): 189-193. DOI: 10.2991/cmsa-18.2018.44.
[25] Ţălu, Mihai and Ştefan Ţălu. "Optimal engineering design of a pressurized paralepipedic fuel tank." *Annals of Faculty of Engineering Hunedoara - International Journal of Engineering, Hunedoara, Romania*, Tome XVI, Fascicule 2 (2018): 193-200.
[26] Ţălu, Ştefan and Mihai Ţălu. "The Influence of corrosion on the vibration modes of a pressurized fuel tank used in automotive industry." *DEStech Transactions on Materials Science and Engineering,* (2018): 1-6. DOI: 10.12783/dtmse/icmsa2018/20560.
[27] Oprițoiu, Petre. PhD thesis: *Cercetări privind transferul termic și al pierderilor de presiune la un schimbător de căldură din metal poros / Research on heat transfer and pressure losses through porous metal heat exchanger.* Technical University of Cluj-Napoca, Romania, Faculty of Mechanics, 2014.
[28] Oprițoiu, Petre. "Fluid flow and pressure drop simulation in aluminium foam heat exchanger." *Acta Tech. Napocensis: Civil Eng. & Arch*., no. 50 (2007): 101-112.
[29] Oprițoiu, Petre. "Heat transfer performance analysis in porous heat exchanger." *Magazine of Hydraulics, Pneumatics, Tribology, Ecology, Sensorics, Mechatronics (HIDRAULICA)*, no. 3 (September 2015): 32-41.
[30] Oprițoiu, Petre. "Rans simulation of combined flow and heat transfer through open-cell aluminum foam heat sink." *Magazine of Hydraulics, Pneumatics, Tribology, Ecology, Sensorics, Mechatronics (HIDRAULICA)*, no. 3 (September 2013): 15-25.
[31] Oprițoiu, Petre. "Prediction of turbulent flow using upwind discretization scheme and k-ε turbulence model for porous heat exchanger." *Magazine of Hydraulics, Pneumatics, Tribology, Ecology, Sensorics, Mechatronics (HIDRAULICA)*, no. 2 (June 2016): 88-97.
[32] Oprițoiu, Petre. "Validation of porous heat exchanger simulation model." Paper presented at International Conference and Exhibition of Hydraulics & Pneumatics HERVEX 2014, Călimăneşti-Căciulata, Romania, 5-7 noiembrie 2014.
[33] Ţălu, Ştefan and Mihai Ţălu. "CAD generating of 3D supershapes in different coordinate systems. "*Annals of Faculty of Engineering Hunedoara - International Journal of Engineering, Hunedoara, Romania*, Tome VIII, Fascicule 3 (2010): 215-219.
[34] Ţălu, Ştefan and Mihai Ţălu. "A CAD study on generating of 2D supershapes in different coordinate systems. "*Annals of Faculty of Engineering Hunedoara - International Journal of Engineering, Hunedoara, Romania*, Tome VIII, Fascicule 3 (2010): 201-203.
[35] Domanski, Jerzy and Zywica Grzegorz. "Optimization of the construction of a pressure tank using CAD/CAE systems." *Technical Sciences* 10 (2007): 41-59. DOI: 10.2478/v10022-007-0006-4.
[36] Nedelcu, Dorian. *Digital Prototyping and Numerical Simulation with SolidWorks / Proiectare și simulare numerică cu SolidWorks*. Timişoara, Eurostampa Publishing House, 2011.
[37] Ţălu, Mihai. *Mecanica fluidelor. Fluid mechanics. The monodimensional laminar flow / Curgeri laminare monodimensionale.* Craiova, Universitaria Publishing House, 2016.
[38] Țălu, Mihai. *Hydraulic pressure loss in technical piping with annular section. Numerical calculation and C.F.D. / Pierderi de presiune hidraulică în conducte tehnice cu secțiune inelară. Calcul numeric și analiză C.F.D.* Craiova, Universitaria Publishing House, 2016.
[39] Niţulescu, Theodor and Ştefan Ţălu. *Applications of descriptive geometry and computer aided design in engineering graphics / Aplicaţii ale geometriei descriptive şi graficii asistate de calculator în desenul industrial.* Cluj-Napoca, Risoprint Publishing House, 2001.
[40] Bîrleanu, Corina and Ştefan Ţălu. *Organe de maşini. Machine elements. Designing and computer assisted graphical representations / Proiectare şi reprezentare grafică asistată de calculator.* Cluj-Napoca, Victor Melenti Publishing House, 2001.
[41] Ţălu, Ştefan. *AutoCAD 2017*. Cluj-Napoca, Napoca Star Publishing House, 2017.
[42] Racocea, Cristina and Ştefan Ţălu. *The axonometric representation of technical geometric shapes / Reprezentarea formelor geometrice tehnice în axonometrie.* Cluj-Napoca, Napoca Star Publishing House, 2011.

ISSN 1453 – 7303 **“HIDRAULICA” (No. 2/2021)**
Magazine *of Hydraulics, Pneumatics, Tribology, Ecology, Sensorics, Mechatronics*

Analysis of Heat Flow and Transfer in the T Joint of a Steam Installation

Prof.Dr.eng. **Mariana PANAITESCU**[1], Prof.Dr.eng. **Fănel-Viorel PANAITESCU**[2],
PhD student **Robert-Alexandru DĂINEANU**[2]

[1] Constanta Maritime University, panaitescumariana1@gmail.com,

[2] Doctoral School of Mechanical and Mechatronics Engineering, Constanta Maritime University, robertibanesto@yahoo.es

Abstract: *In order to produce the steam necessary for the operation of the main cars of the ship and to supply all the consumers on board, the naval boilers need an operating regime, which ensures the transformation of the chemical energy of the fuel into caloric energy contained in steam in the best conditions. In this paper, we showed a high temperature fluid flow in a pipe through a T section and the effect of temperature on the pipe material. Pipe deformation caused by fluid temperature was analyzed. The temperature distribution effect of ANSYS Fluent was used as a thermal load in the pipe body. The pipe deflection was discovered together with the equivalent voltage and thermal stress.*

Keywords: *Heat, flow, transfer, steam, structural, pipe, joint*

1. Introduction

The main parts of a steam production installation are the boiler itself or the boiler system (composed of the drum or water collectors and all the pipes in which the water vaporization occurs), the steam superheater, the preheater of the supply water, the air preheater and the hearth or combustion chamber.
The resulting steam will be used for the operation of various mechanisms and auxiliary devices or on-board systems such as:
• steam extinguishing system
• installation for heating fuel and oil in storage, settling, service and mixing tanks
• ship heating installation
• water heating to prepare the main engine.
In order to produce the steam necessary for the operation of the main cars of the ship and to supply all the consumers on board, the naval boilers need an operating regime, which ensures the transformation of the chemical energy of the fuel into caloric energy contained in steam in the best conditions [1].
The intimate operating regime of the boiler is when the water turns into steam, accumulating a maximum amount of heat from the burned fuel in the boiler hearth. The steam will be able to accumulate maximum heat, only if the combustion process takes place with a maximum heat release and if the heating is provided with a good circulation and water supply, and the heating surface allows a good heat transfer from gas to the water.

The above-mentioned boiler is an aquatubular naval boiler that works at a nominal pressure of 7 bar.

Boiler is used to produce the amount of steam needed to heat a ship's main engine.
The ship is equipped with a main engine type MAN 6L 52 / 55A with an effective power P_e = 6100 HP = 4413 kW.
The available flow of the main engine is

$$Q_{dMP} = \frac{c_e \cdot P_e \cdot Q_l}{3600}, \text{ [kW]} \qquad (1)$$

Where:

c_e = 0.265 [kg / kWh]- the actual specific consumption of the engine

P_e = 4413 [kW] effective engine power

Q_l = 37500 [kJ / kg] lower calorific value of the fuel used.
If the cooling water is heated by means of a preheater mounted in the technical water circuit, the following curves can be used (Figure 1) [2]:

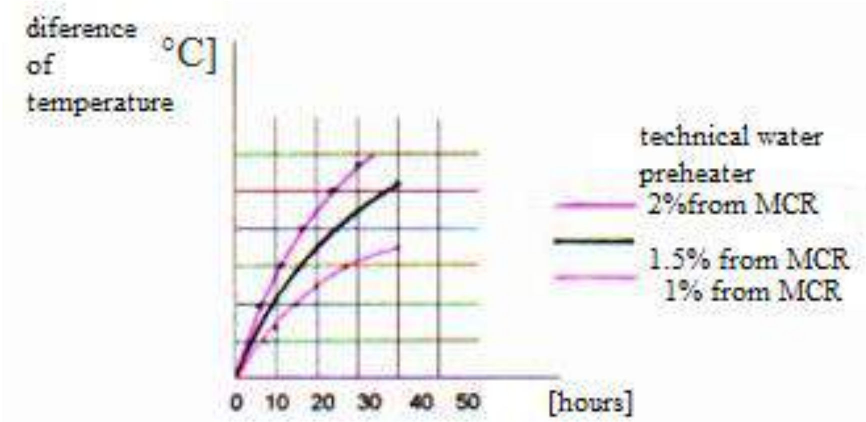

Fig. 1. Cooling curves in the preheater

The technical water flow of the preheater, if installed by bypass, will be around 10% of the flow of the main technical water pump. The pressure drop in the preheater will be about 0.2 [bar].
The curves are drawn in these hypotheses, at the beginning of the preheating, the temperature of the engine and of the engine room being equal [3].
Normally, before taking the first steps to start the engine, the minimum engine temperature must be 60°C, and the engine can start slowly without further restrictions. In exceptional cases, a minimum temperature of 20°C is allowed. In these circumstances, the engine can start slowly up to 90% rpm, without restrictions. In order to operate between 90% rpm and 100% MCR, a minimum temperature of 50°C must be ensured. The time interval for raising the engine temperature from 20°C to 50°C depends on the amount of water in the system and the engine load. It is recommended in the region of 90% rpm and 100% MCR; the load will be raised slowly - in 30 minutes.

2. Method and research

We will choose a preheater with a heating capacity of 2% of MCR, which will raise the engine temperature to 55°C in 30 hours.

$$Q_{pr} = P_e \cdot 0.02 \quad [kW] \tag{2}$$

So, Q_{pr} = 88.26 kW.
However, this energy flow is equal to that given by the steam produced in the boiler necessary to heat the water

$$m = Q_{pr}/D_{i7bar} = 152.22 \quad [kg/h] \tag{3}$$

Where:
$\Delta i_{5bar} = 2109\ [kJ/kg]$- the difference in enthalpy of steam at the boiler working pressure of 5 bar.

2.1 The amount of steam needed to heat the fuel in the storage tanks

The cargo ship 7800 tdw can ship a bunker quantity of 1200 tons of fuel.
We consider that we must always have 10% of the amount of bunker, ready at all times, for consumption on board.

$m_{cb.\ tk.\ dep.}$= 120 [t].

The heating time of this mass of fuel will be: $\tau = 6\ hours$. It turns out that a mass flow of:

$$m_{cb.tk.dep.} = \frac{m_{cb.tk.dep.}}{\tau \cdot 3600} \quad \left[\frac{kg}{s}\right] \tag{4}$$

So, $m_{cb.tk.dep.}$ = 5.55 [kg/s].
The energy flow required to heat the fuel will be:

$$Q_{cb.tk.dep.} = m_{cb.tk.dep.} \cdot c_{cb} \cdot \left(t_{cb} - t_{dep}\right)\ [kW] \tag{5}$$

So, $Q_{cb.tk.dep.}$ = 333.33 [kW],

Where:
$c_{cb} = 2\ [kJ/kg \cdot grd]$ is specific heat of the fuel;

$t_{cb} = 40°[C]$ is the temperature at which the fuel must be heated in the storage tank;

$t_{dep} = 10°[C]$ is fuel temperature in the storage tank.

The mass steam flow required to heat the fuel in the storage tank is:

$$\eta_{serp} = \frac{Q_{cb.tk.dep.}}{Q_{steam}} = \frac{Q_{cb.tk.dep.}}{m_{steam} \cdot \Delta i_{5bar}} \Rightarrow m_{steam} = \frac{Q_{cb.tk.dep.}}{\eta_{serp} \cdot \Delta i_{5bar}} \quad \left[\frac{kg}{h}\right] \tag{6}$$

So, the value is η_{serp} = 605.16 [kg/h].

3. The amount of steam required to heat the fuel in the tailings tank

The hourly consumption of the 3 Diesel Generators is noted C_{h3DG}. The boiler with burner we assume has a consumption of: C_{harz} = 88 [kg / h].

The total hourly consumption of all the aggregates on the ship is:

$$C_{htot} = C_{hMP} + C_{h3DG} + C_{harz}\ \ [kg/h] \tag{7}$$

So, the value is C_{htot} = 0.4168 [kg/s] = 1500.4 [kg/h].

The mass flow rate of fuel to be heated in the tailings tank will be 2.5 times higher than the total hourly fuel consumption of the aggregates on the ship:

$$m_{cb.tk.dec.} = 2.5 \cdot C_{htot}\ \ [kg/h] \tag{8}$$

So, will be equal $m_{cb.tk.dec.}$ = 3751 [kg/h]
Where:

- fuel temperature in the settling tank, $t_{dec} = 30\ [°C]$;

- the temperature to be reached before the fuel enters the two preheaters of fuel separators, $t_{sep} = 70\ [°C]$.

The mass steam flow required to heat the fuel in the tailings tank is:

$$m_{steam.tk.dec.} = \frac{Q_{cb.tk.dep.}}{\eta_{serp} \cdot \Delta i_{5bar}} \quad \left[\frac{kg}{h}\right] \tag{9}$$

So, the value is $m_{steam\ tk.dec.}$= 211.87 [kg/h].

4. The amount of steam needed to heat the fuel in the mixing tank

Whether

$t_{imp} = 120° \; [C]$ - fuel injection temperature;

$t_{tkam.} = 95° \; [C]$ - temperature in the mixing tank.

Mass flow rate of steam required to heat fuel before injection is calculated with formula (10):

$$m_{cb.tk.am.} = \frac{Q_{cb.tkam.}}{\eta_{serp} \cdot \Delta i_{5bar}} \quad \left[\frac{kg}{h}\right] \tag{10}$$

The values is $m_{cb\ tk.am.}$= 29.5 [kg/h].

5. The amount of steam needed to heat the main engine lubricating oil before entering the separator

Actual specific oil consumption of the main engine is:

$$c_e = (2.5 \ldots 7) \cdot \; 10^{-4} \quad [kg/kWh] \tag{11}$$

So,
c_e = 0.00033 [kg/kWh].
Hourly oil consumption of the main engine is:

$$C_{hoil} = c_e \cdot P_e \qquad [kg/h] \tag{12}$$

So, c_{hoil} = 1.4563 [kg/h].
Energy flow required to heat the oil before entering the separators is:

$$Q_{oil.inc.sep.} = \; m_{oil} \cdot c_{oil} \cdot \left(t_{sep} - t_{dep}\right) \qquad [kW] \tag{13}$$

Where:

$c_{oil} = 2.1 \;\; [kJ/kg \cdot grd]$ - specific heat of the lubricating oil;

$t_{sep} = 90° \; [C]$ - the temperature at which the oil is separated;

$t_{dep} = 20° \; [C]$ - the temperature at which the oil is stored.

So, $Q_{oil.inc.sep.}$ = 429.149 [kW].
Mass flow of oil to be circulated by separators is:

$$m_{oil} = 2 \cdot C_{oil} \qquad [kg/s] \tag{14}$$

So, m_{oil} = 0.000809 [kg/s].
Mass flow of steam required to heat the oil in the separator preheaters is:

$$m_{steam\ oil} = \frac{Q_{oil\ inc\ sep.}}{\eta_{serp} \cdot \Delta i_{5bar}} \qquad [kg/h] \tag{15}$$

So, $m_{steam\ oil}$ = 0.2159 [kg/h].

6. The amount of steam needed to heat the air in the room heating installation

The mass flow of air circulated for heating the cabins is given by the volume flow of the fan, which is:

$$m_{air} = \rho_{air} \cdot V_{air} \qquad [kg/s] \tag{16}$$

Where:

V_{air} = 25000 [m^3/h]; $c_{air} = 1\ \ [kJ/kg \cdot grd]$ - specific heat of the air; $t_{inc} = 24°\ [C]$ - cabin heating temperature; $t_{m\ amb} = 5°\ [C]$ - ambient temperature.

Therefore, the mass flow of air circulated will be m_{air} = 8.5139 [kg/s].

Mass flow of steam required for heating the air in the air conditioning system is:

$$m_{steam\ inc\ air} = \frac{Q_{air\ inc}}{\eta_{serp} \cdot \Delta i_{5bar}} \qquad [kg/h] \tag{17}$$

So, the value is $m_{steam\ inc.air}$ = 293.68 [kg/h].

7. Determining the boiler flow and its power

The total flow of the boiler with aquatubular type burner is given by the relation:

$$m_{CA} = \sum_{i-1}^{8} m_i \qquad [kg/h] \tag{18}$$

So, m_{CA} = 1455.3 [kg/h].

The available boiler flow is:

$$Q_{DCA} = \frac{C_h \cdot Q_i}{3600} \quad [\text{kW}] \tag{19}$$

So, Q_{DCA} = 916.66 [kW].

Boiler power is:

$$Q_{CA} = Q_{DCA} \cdot\ \eta_{CA} \tag{20}$$

So, Q_{CA} = 843.33 [kW]. Otherwise, the power of the boiler is given by the relation:

$$Q_{Cazn} = m_{steam\ tot} \cdot \Delta i \qquad [kW] \tag{21}$$

So, Q_{Cazn} = 843.81 [kW].

Fuel consumption will be determined from the relation:

$$\eta_{CA} = \frac{Q_{Cazn}}{Q_{dispCA} \cdot \frac{C_h \cdot Q_i}{3600}} \ \ \Rightarrow\ \ C_h = \frac{3600 \cdot Q_{Cazn}}{\eta_{CA} \cdot Q_i} \qquad [kg/h] \tag{22}$$

Therefore, the value is 88.05 [kg/h] and the value adopted in the previous point is correct.

8. Analysis of heat flow and transfer in the T joint

8.1. The interaction of fluid structure

The geometry of the part is created in the Ansys program and the domains are defined and the surface of the inner domain is defined. (Figure 2).

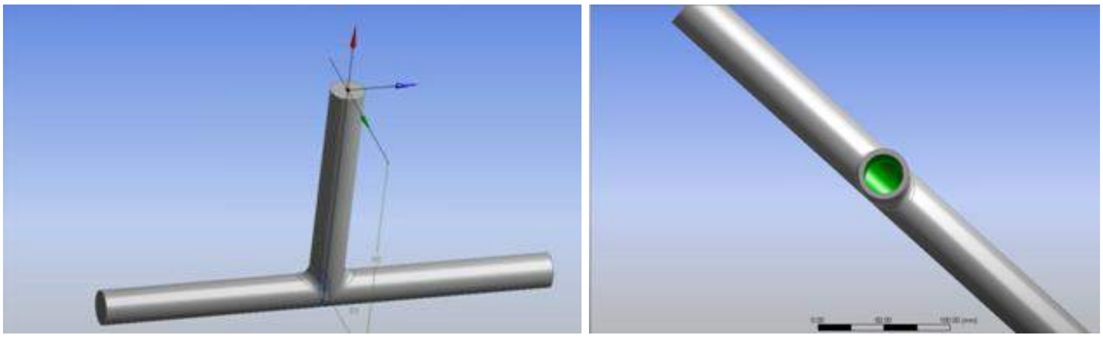

Fig. 2. The geometry and the inner domain

We change the flow direction to be able to add the inner surface to the solid so that it forms a single body. The fluid domain is created inside the pipe as seen in the figures below (Figure 3, 4).

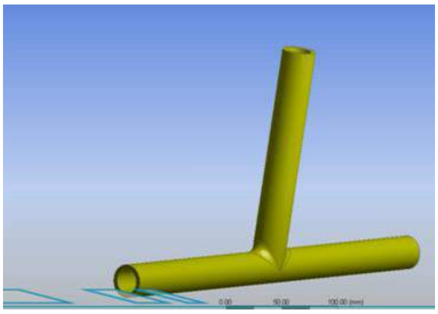

Fig. 3. The flow direction and the addition of the inner surface to the solid

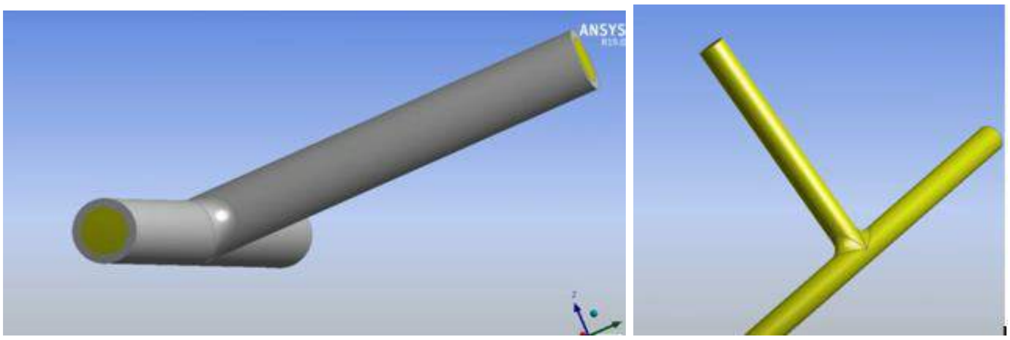

Fig. 4. The fluid domain

The discretization of the reference piece follows. Following the discretization, 16429 nodes and 83346 elements are obtained (Figure 5).

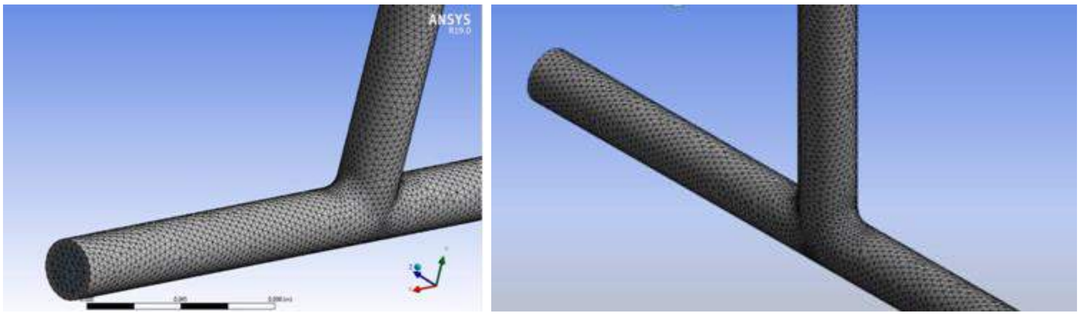

Fig. 5. The discretization

Check the quality of the discretization using the "Skewness" display style (Figure 6).

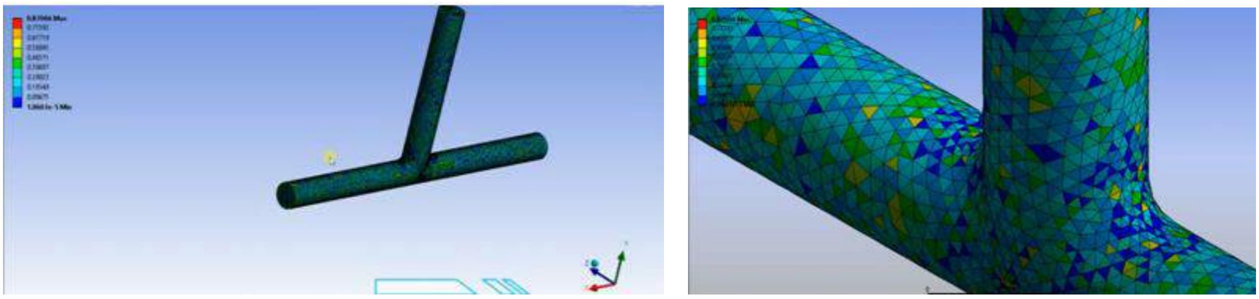

Fig. 6. The discretization using the "Skewness" style

We name the surfaces as can be seen in the following Figures 7, 8, 9.

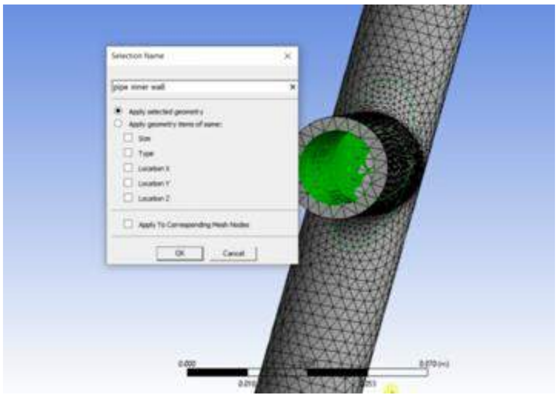

Fig. 7. The pipe inner wall

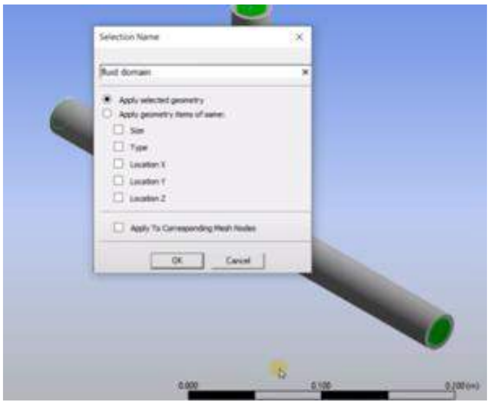

Fig. 8. The fluid domain

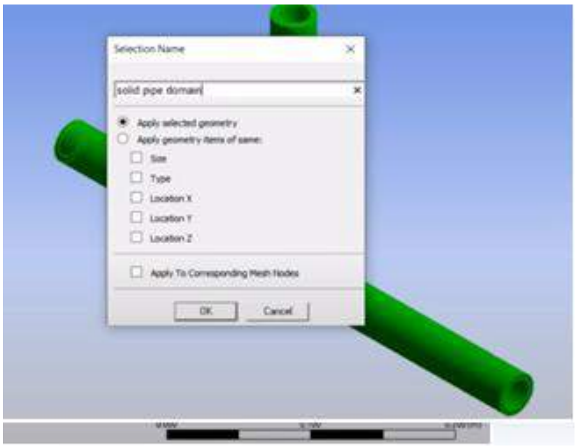

Fig. 9. The solid domain

The characteristics of the model and the material are defined. The material is assigned to the areas for which we have defined it. We set the limit conditions for entry and exit (Figure 10).

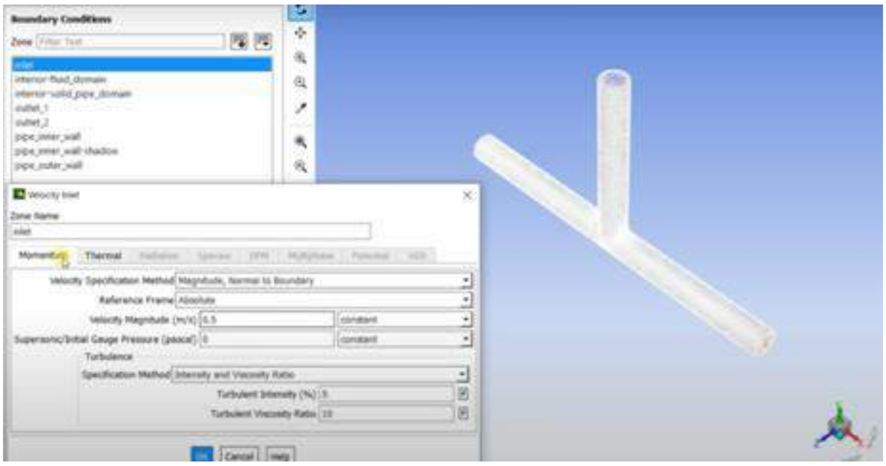

Fig. 10. The boundary conditions

8.2. Experimental data

Set the temperature of the pipe (300^0 C) and the hybrid solution is initialized with a number of 800 iterations. Create a plan in the middle section of the pipe. When representing the temperature, we notice that the temperature decreases towards the outside of the pipe (Figure 11).

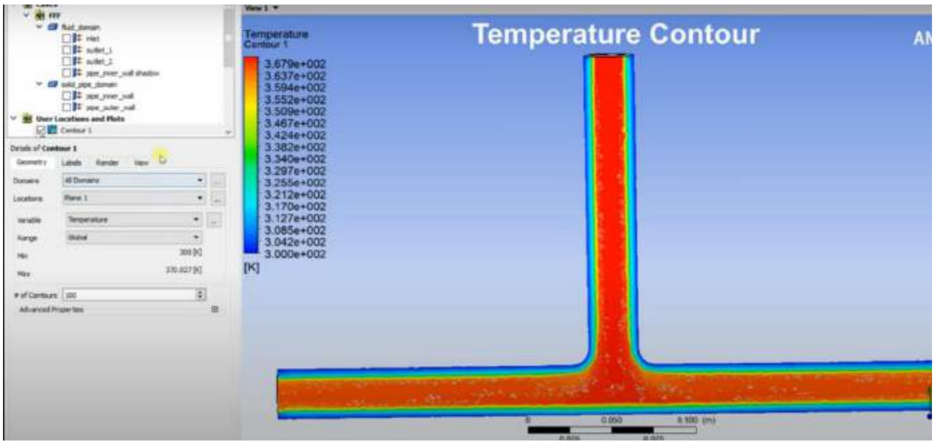

Fig. 11. The variation of temperature

The fluid speed decreases in the flow direction, from the inlet to the outlets (Figure 12).

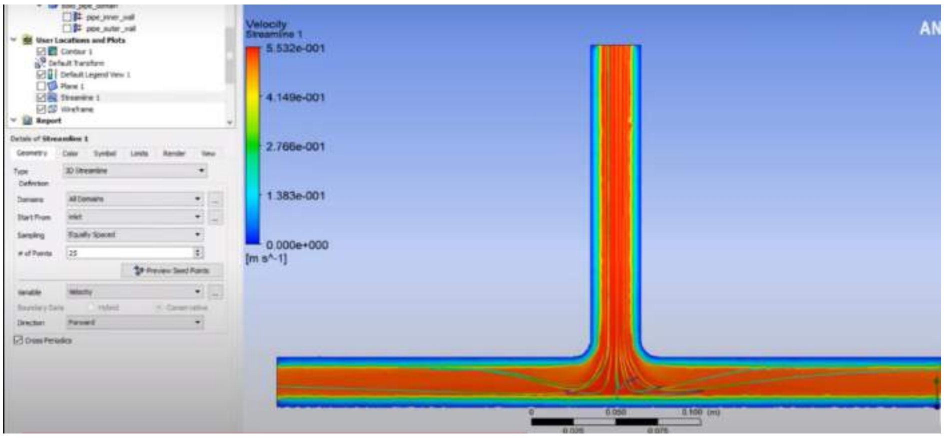

Fig. 12. The variation of fluid speed

The speed animation I showed in the figure below (Figure 13).

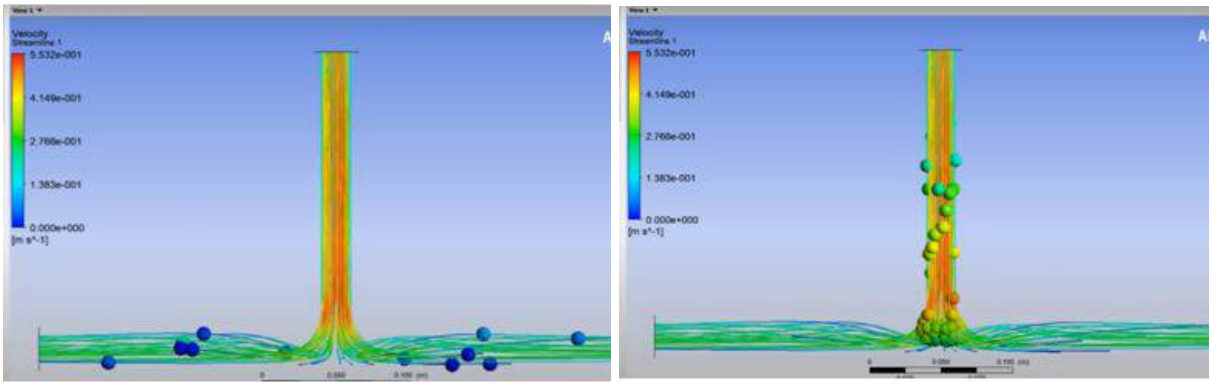

Fig. 13. The speed animation

We add the static structural analysis system in the schematic window of the project, near the "Fluid Flow (Fluent)" analysis system; we connect the geometry and the solution between the two systems (Figure 14).

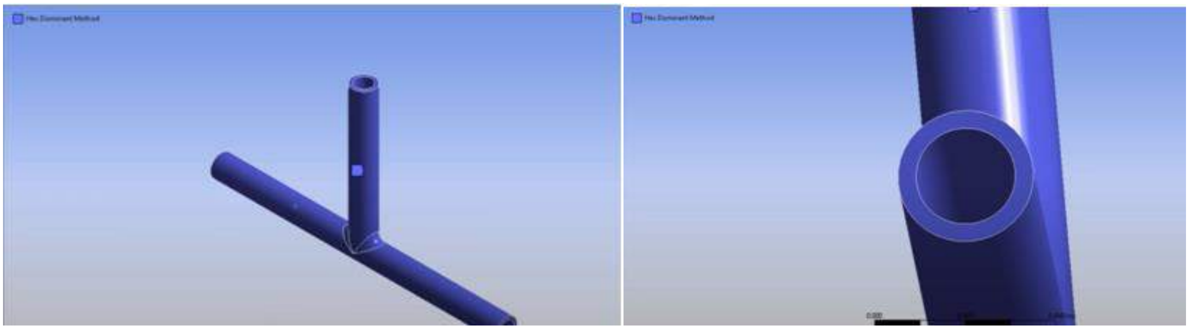

Fig. 14. The static structural analysis system

The piece is discretized and 59826 nodes and 15721 elements are obtained (Figure 15).

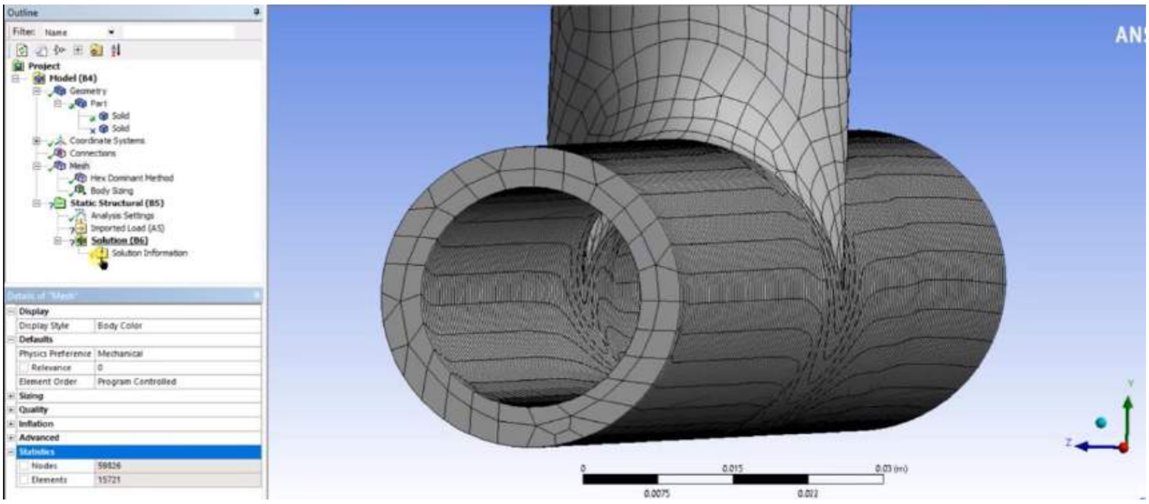

Fig. 15. The discretization of system

The standard gravitational acceleration is introduced in the direction of the fluid velocity, in order to be able to calculate the deformation (Figure 16) [4].

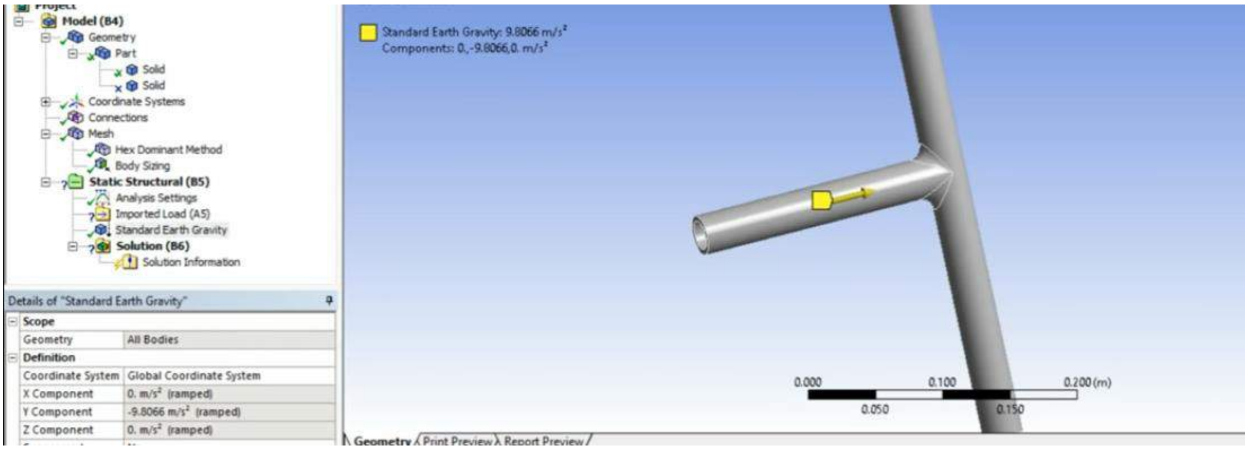

Fig. 16. The addition of standard gravitational acceleration

The distribution temperature is imported (Figure 17).

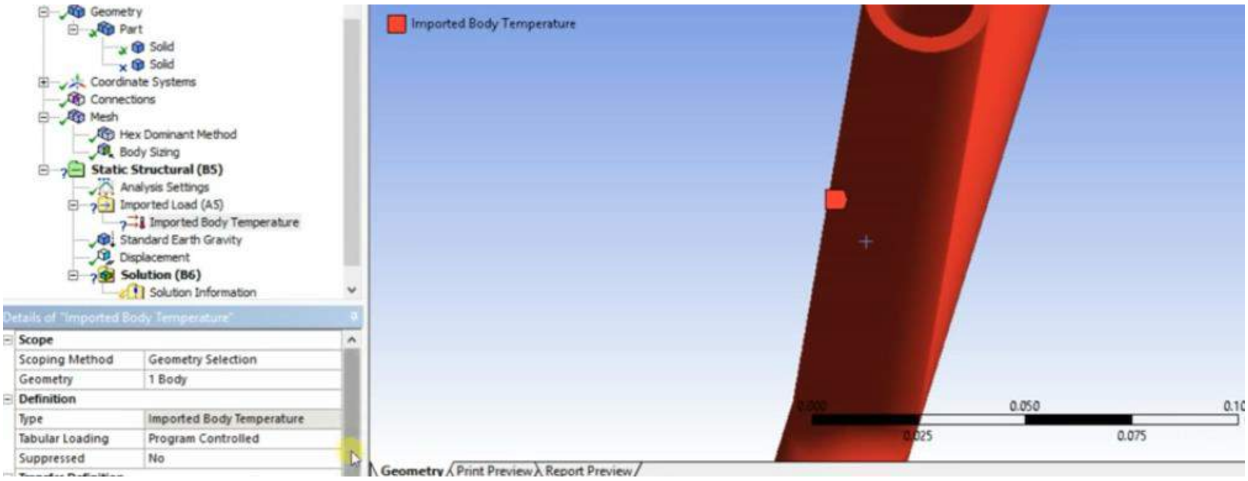

Fig. 17. The imported distribution of temperature

The points where the temperature is maximum are shown, it is found inside the pipe (Figure 18).

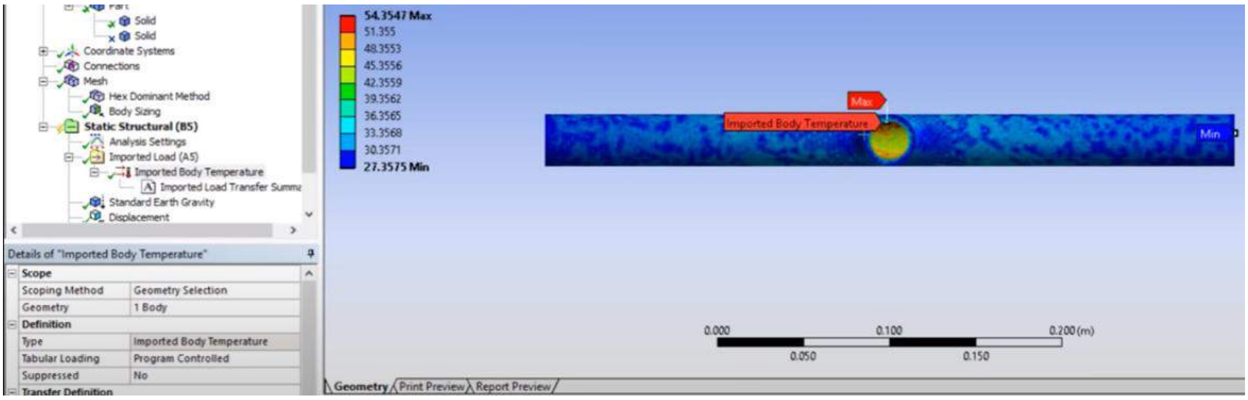

Fig. 18. The maximum temperature inside of pipe

The maximum total deformation is found in the pipe joint (Figure 19).

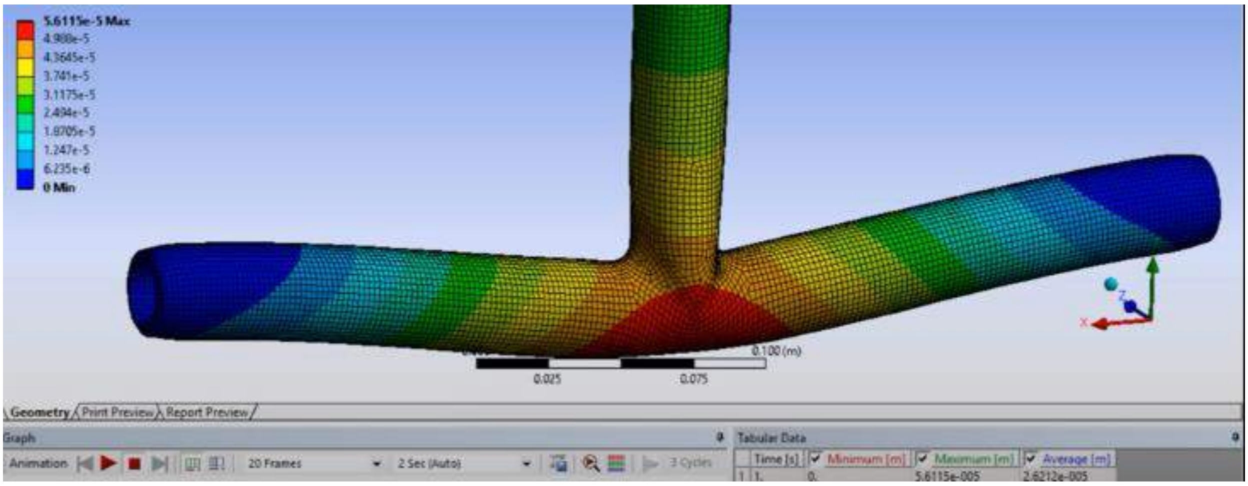

Fig. 19. The maximum total deformation

The directional deformation, on the y axis, has a maximum value of 0.002824 [mm].

The maximum equivalent stress is found in the joint area (Figure 20) and has a maximum value of 530.36 MPa.

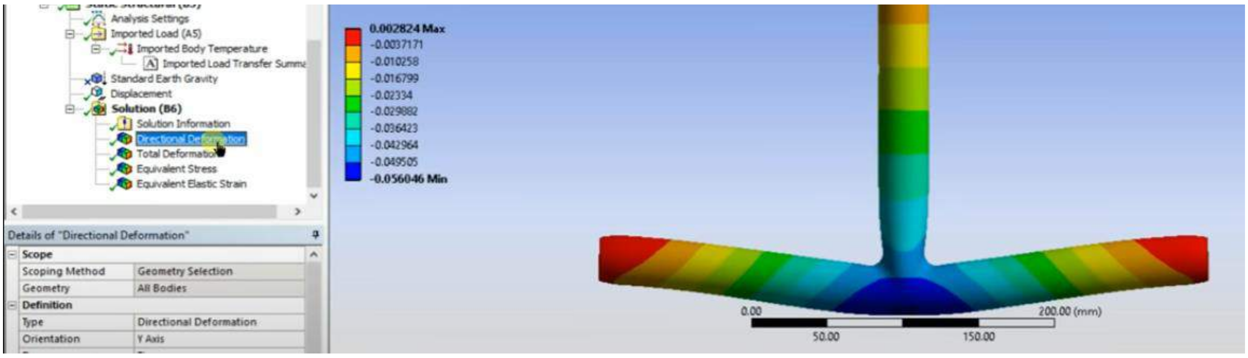

Fig. 20. The maximum equivalent stress

The equivalent elastic tension (Figure 21) has a maximum value of 0.0027516 and is found inside the pipe.

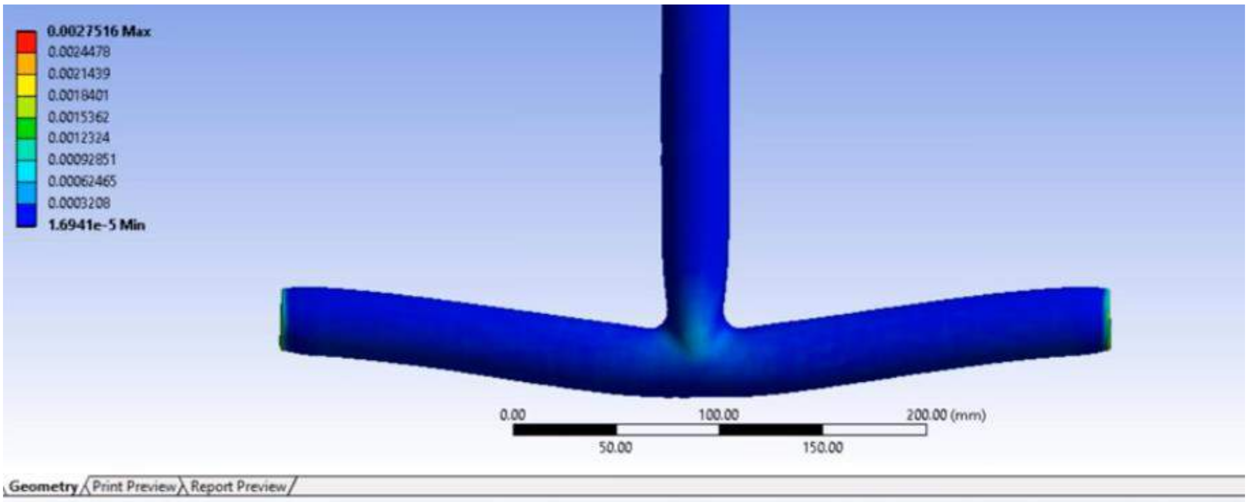

Fig. 21. The equivalent elastic tension

8.3. Final results

The final results are:
- Total deformation (Figure 22);
- Deformation on the "Y" direction measured in mm (Figure 23);
- Equivalent stress measured in MPa (Figure 24);
- Equivalent elastic tension measured in mm (Figure 25).

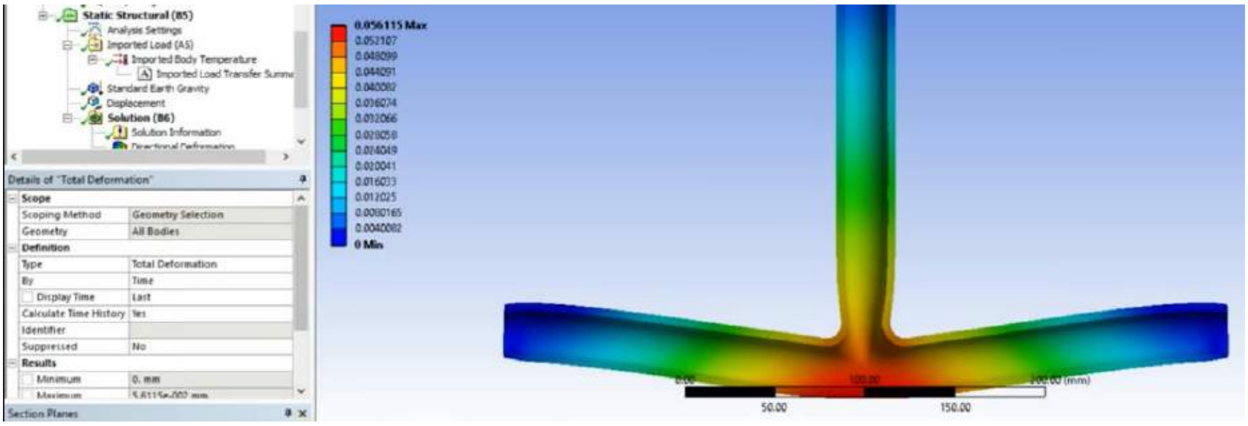

Fig. 22. Total deformation

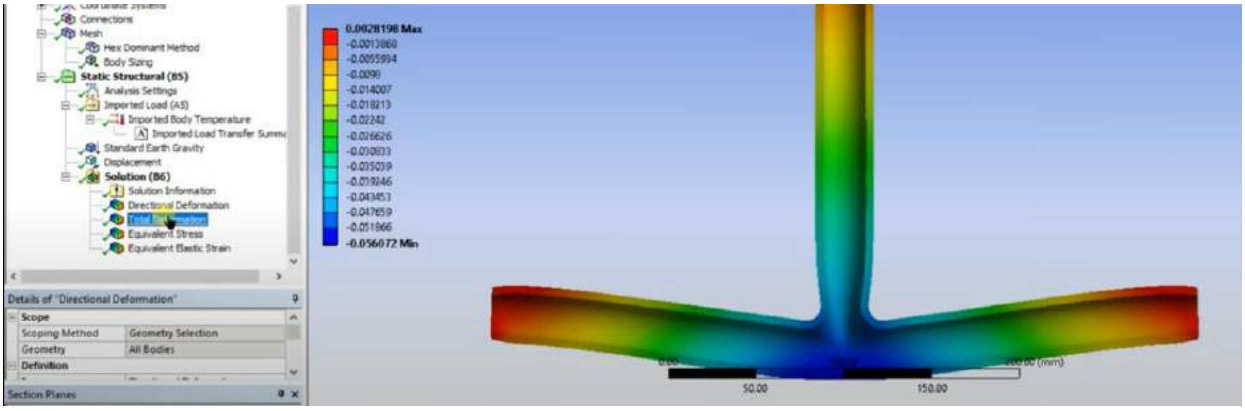

Fig. 23. The deformation on the "Y" direction

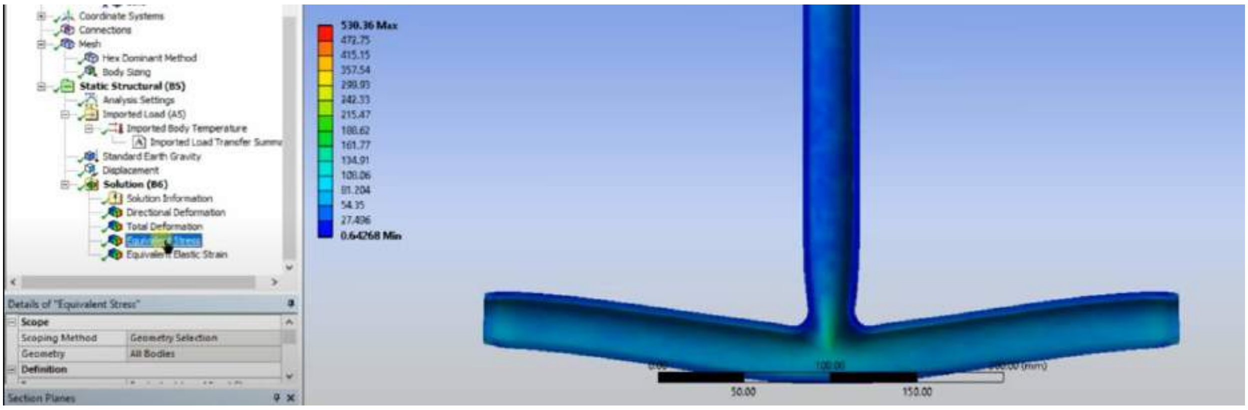

Fig. 24. The equivalent stress

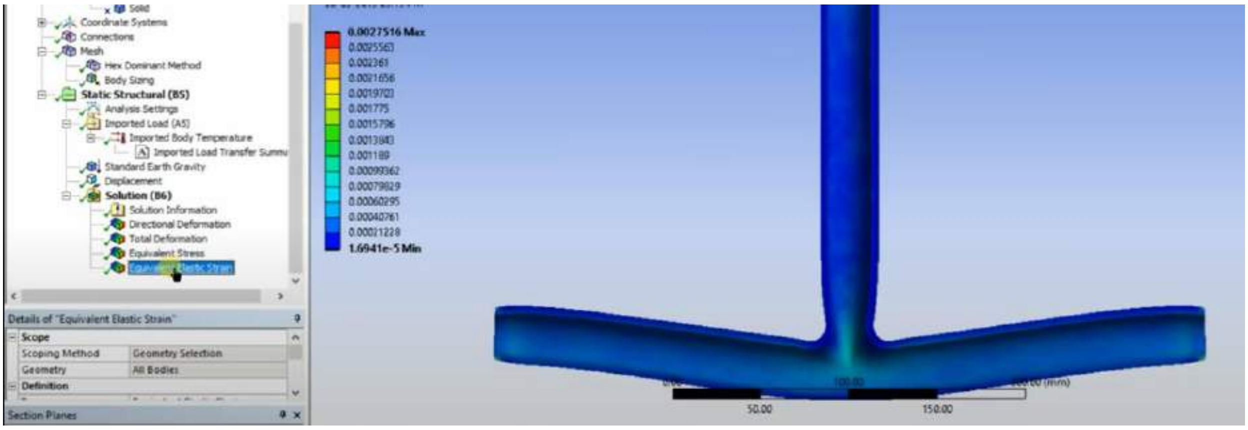

Fig. 25. The equivalent elastic tension

9. Conclusions

We analyzed a high temperature fluid flow in a pipe through a T section and the effect of temperature on the pipe material. Pipe deformation caused by fluid temperature was analyzed. The temperature distribution effect of ANSYS Fluent was used as a thermal load in the pipe body. The pipe deflection was discovered together with the equivalent voltage and thermal stress.

References

[1] Panaitescu, Fanel-Viorel, and Mariana Panaitescu. *Naval machines and installations/Maşini şi instalaţii navale.* Constanta, EXPONTO Publishing House, 2009.
[2] Radcenco, Vsevolod. *Generalized thermodynamics/Termodinamica generalizata.* Bucharest, Technical Publishing House, 1994.
[3] Radcenco, Vsevolod. "The Treatment of the energy Preservation Principle on the Base of the Generalized Polytropic Transformation." *Poytechnic Bulletin*, no. 2 (June 1994): 15-29.
[4] Voicu, Cosmin. *Fluid structure interaction using the Ansys program/Interacțiunea structurii fluidelor folosind programul Ansys: project Advanced concepts of naval hydrodynamics.* Constanta, 2020.

Comparative Study on Providing the Necessary Heating for a Renewable Air Treatment Plant

Prof. Dr. Eng. **Valentin APOSTOL**[1], Ș.l. Dr. Eng. **Mihaela CONSTANTIN**[1*],
Conf. Dr. Eng. **Horațiu POP**[1], Ș.l. Dr. Eng. **Beatrice IBREAN**[1],
Std. **Cristian MARIN**[1], As. Dr. Eng. **Daniel TABAN**[1]

[1] University Politehnica of Bucharest

* i.mihaelaconstantin@gmail.com

Abstract: *This paper presents a comparative study of the different types of solar collectors regarding the provision of heating for an air treatment plant from renewable sources, namely, solar energy. An analysis of the area required for the use of photovoltaic panels and a calculation of the determination of thermal energy from the sun's rays when using solar collectors is provided. The study established that the production of own energy by capturing sunlight using these types of networks is advantageous in the long run. The possibility of faster amortization of the investment is obtained by putting to use the surplus energy to various consumers.*

Keywords: *Solar collectors, solar energy, photovoltaic panels*

1. Introduction

The sun is a sphere of very hot gaseous matter with a diameter of 1.39 x 109 m. It has an effective black body temperature of 5762 K [1]. In fact, the sun is a continuous fusion reactor in which hydrogen is converted to helium. The total energy production of the sun is 3.8 x 10^{20} MW which is equal to 63 MW / m^2 of the sun's surface. This energy radiates outward in all directions. Only a small fraction, 1.7 x 10^{14} kW, of the total radiation emitted is intercepted by the earth [1]. However, even with this small fraction it is estimated that 30 minutes of solar radiation falling to the earth is equal to the world's energy demand for a year.
Solar energy collectors are a special type of heat exchanger that converts the energy of solar radiation into the internal energy of the transport environment. The major component of any solar system is the solar collector. A large number of solar collectors are available on the market. A comprehensive list is presented in the paper [2].
The aim of this paper was to ensure the necessary heating of a space by adapting renewable energy sources. The following types of batteries were used to perform the heating process:
- Heating battery with electric resistance;
- Hot water heating battery.

Fig. 1. Heating battery with electric resistance [3]

Fig. 2. Hot water heating battery [4]

Photovoltaic panels aim to transform the sun's light energy into electricity. The main characteristic element of these panels are the photovoltaic cells. It can be used in connection with, or separately from, electricity storage batteries produced to power consumers.

To perform the calculation, a solar panel was chosen from the manufacturer WATTROM, with the WT 60-SM series [5].

Fig. 3. Photovoltaic panel [6]

The energy produced by the photovoltaic panels is used to provide the electricity needed for an air heater battery by means of an electrical resistor shown in Figure 1.
Compared to the photovoltaic panels (fig. 3), the flat solar collectors (fig. 4) through their constructive form capture the solar energy transforming it into thermal energy, used for heating the fluid that crosses the coil of the panel. Subsequently, the fluid is used to supply the heating battery (fig. 2).
To perform the calculation, a flat solar collector was chosen from the manufacturer SUNSYSTEM, with the PK SL / CL - 2.0 series [7].

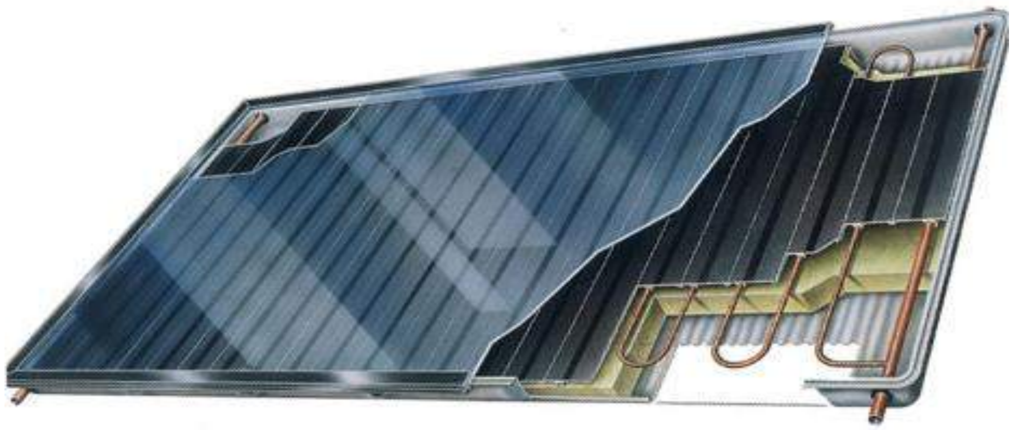

Fig. 4. Flat solar collector

The variability of electricity costs imposes uncertainties in the use of air conditioning systems in the future. For these reasons, the aim is to adapt to air conditioning the sources that produce the necessary electricity from renewable sources.
Today's air conditioning systems have become considerably more energy efficient, but these systems are usually the largest consumer of electricity in a residence, commercial or industrial space.
This paper was made for the climatic conditions on the territory of Bucharest. The aim was to find the collecting area required for a consumption of 4 kW.

2. Calculation of the area required for the use of photovoltaic panels

To perform the calculations of energy produced with the help of the sun, the Photovoltaic Geographical Information System program was used, in which the coordinates of the Municipality of Bucharest were introduced. These coordinates are shown in Table 1.

Table 1: The coordinates of the Municipality of Bucharest.

City	Latitude	Longitude
Bucharest	44.4267674	26.102538390000063

Figure 1 shows the workspace of the Photovoltaic Geographical Information System [8].

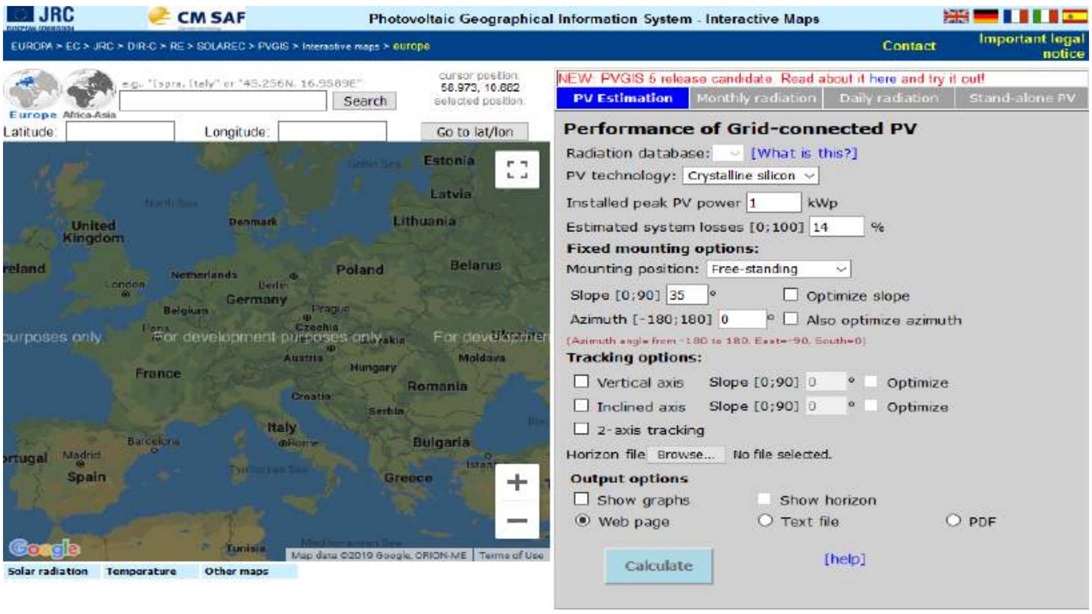

Fig. 5. Photovoltaic Geographical Information System

The results generated by the program shown in Figure 5 are presented in Table 2:

Table 2: Numerical simulation results.

	E_d [kWh]	E_m [kWh]	H_d[kWh/m^2]	H_m[kWh/m^2]
January	1.60	49.50	1.91	59.30
February	2.45	68.60	3.01	84.20
March	3.69	114.00	4.78	148.00
April	4.09	123.00	5.50	165.00
May	4.41	137.00	6.07	188.00
June	4.53	136.00	6.32	190.00
July	4.68	145.00	6.60	204.00
August	4.56	141.00	6.43	199.00
September	3.79	114.00	5.22	157.00
October	3.13	97.10	4.10	127.00
November	2.00	60.10	2.51	75.40
December	1.37	42.30	1.65	51.30

Where:
E_d - average daily electricity produced by the collecting area [kWh];
E_m - average annual electricity produced by the collecting area [kWh];
H_d - average daily solar radiation per m2 received by the collecting area [kWh /m^2];
H_m - average annual solar radiation per m^2 received by the collecting area [kWh/m^2].

To determine the optimal area, a study was performed based on an imposed energy requirement and several values of the solar energy collecting area.
The data sheet of the treatment plant [9] specifies that the air handling unit has a heating battery with an electrical resistance with two coils, each of 3 kW. Thus, a minimum value (3kW) and a maximum value (6 kW) were chosen, with the help of which the energy requirement (4kW) was determined, for which the module operates at a capacity of 67%.
Five values of the optimal area of the photovoltaic panels were chosen. These are shown in Table 3.

Table 3: Areas of photovoltaic panels.

Collecting area 1	10	m^2
Collecting area 2	25	m^2
Collecting area 3	50	m^2
Collecting area 4	**75**	$\mathbf{m^2}$
Collecting area 5	105	m^2

With the help of the Photovoltaic Geographical Information System program, depending on each chosen value, the total electricity produced for each month of the year was calculated. The results are presented in Table 4

Table 4: Annually produced electricity.

	E_d Area 1	E_d Area 2	E_d Area 3	E_d Area 4	E_d Area 5
January	0.67	1.67	3.33	**5.00**	7.07
February	1.02	2.55	5.10	**7.66**	10.82
March	1.54	3.84	7.69	**11.53**	16.30
April	1.70	4.26	8.52	**12.78**	18.06
May	1.84	4.59	9.19	**13.78**	19.48
June	1.89	4.72	9.44	**14.16**	20.01
July	1.95	4.88	9.75	**14.63**	20.67
August	1.90	4.75	9.50	**14.25**	20.14
September	1.58	3.95	7.90	**11.84**	16.74
October	1.30	3.26	6.52	**9.78**	13.82
November	0.83	2.08	4.17	**6.25**	8.83
December	0.57	1.43	2.85	**4.28**	6.05
Total [kW]	16.79	41.98	83.96	**125.94**	177.99

Based on the data presented in Table 4, the graph in Figure 6 was plotted.

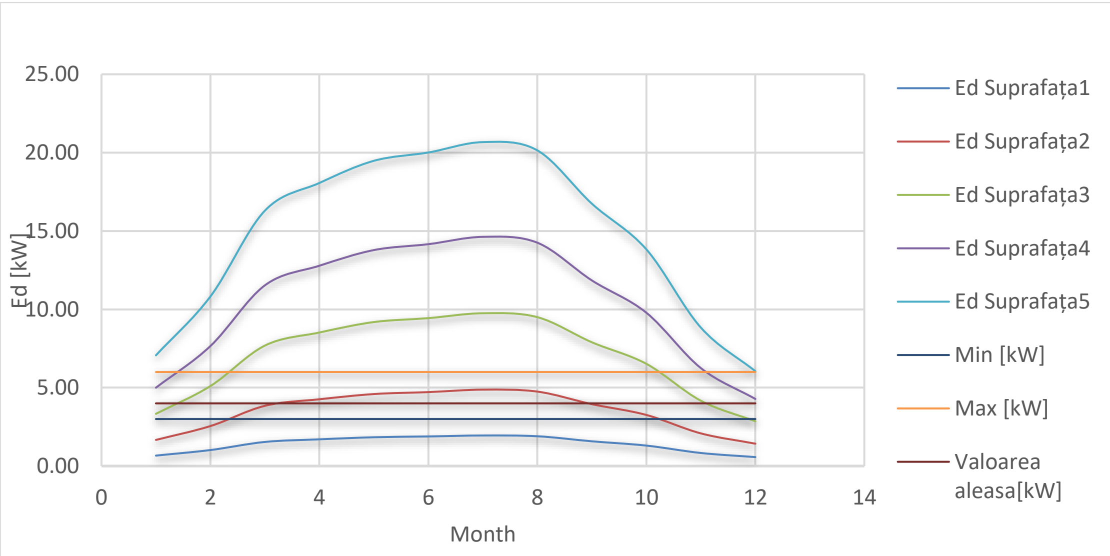

Fig. 6. Study of the energy produced by the sun's rays for several areas

The aim was to obtain a power requirement greater than or at least equal to 4 kW (previously established value). As can be seen, for the value of area 4, the energy requirement has a minimum value of 4.28 kW in December. Thus, the value of the optimal area will be 7575 m^2.

3. Calculation of heat flux when using the solar collector

For the use of thermal energy calculations from the sun's rays, the Photovoltaic Geographical Information System program was used, in which the coordinates of the Municipality of Bucharest were introduced, presented in table 1.
Figure 7 shows the Photovoltaic Geographical Information System program interface.

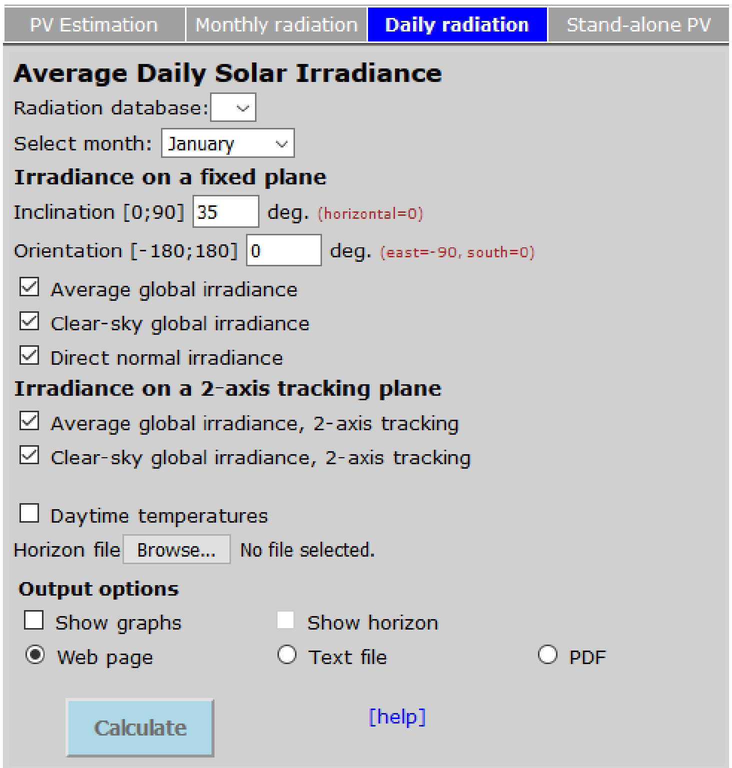

Fig. 7. Solar radiation section within the Photovoltaic Geographical Information System program

The heat flow rate can be determined with the following relation:

$$\dot{Q}_{cs} = \frac{m_w \cdot c_w \cdot \left(t_{final} - t_{initial}\right)}{\Delta\tau}\left[kW\right] \quad (1)$$

Where:
m_w = 700 kg – the mass of water in the installation tank;
c_w = 4,186 kJ/kgK – specific heat of water;
t_{final} – the final temperature of the water in the tank after 15 min;
$t_{initial}$ – the initial temperature of the water in the tank at the beginning of a new measurement;
$\Delta\tau$ = 15 min – the time interval at which a new measurement is made.
The determination of the value for t_{final} after every 15 minutes can be done by means of an iterative calculation.
From relation (1) it is possible to determine t_{final}, as:

$$t_{final_I} = \frac{\dot{Q}_{cs_I} \cdot \Delta\tau_I}{m_w \cdot c_w} + t_{initial_I}\left[^\circ C\right] \quad (2)$$

For the next iteration, the condition that the value of t_{final} from the previous calculation becomes the new value for $t_{initial}$.

$$t_{final_{II}} = t_{initial_{I}} \left[^{\circ}C \right]$$

$$t_{final_{II}} = \frac{\dot{Q}_{cs_{II}} \cdot \Delta\tau_{II}}{m_w \cdot c_w} + t_{final_{I}} \left[^{\circ}C \right] \tag{3}$$

Is possible to determine the iterative computational relation:

$$t_{final_{i}} = \frac{\dot{Q}_{cs_{i}} \cdot \Delta\tau_{i}}{m_w \cdot c_w} + t_{final_{i-1}} \left[^{\circ}C \right] \tag{4}$$

In relation (4) the determination of the final temperature in the tank of the installation at the end of a unit of time (Δτ = 15 min) was performed. The installation was designed to power the heating battery of an air treatment plant. The treatment plant module needs a water temperature between 50 - 60 °C according to the technical data sheet of the installation [9].
To determine the t_{final} temperature, the relation (4) is resumed:

$$t_{final_{i}} = \frac{\left(\dot{Q}_{cs_{i}} - \dot{Q}_{CTA_{i}}\right) \cdot \Delta\tau_{i}}{m_w \cdot c_w} + t_{final_{i-1}} \left[^{\circ}C \right] \tag{5}$$

Where:

$\dot{Q}_{CTA_{i}}$ - heat flow rate consumed by the air treatment plant [kW].

The graph presented in figure 8 was made based on the values determined for a whole year.

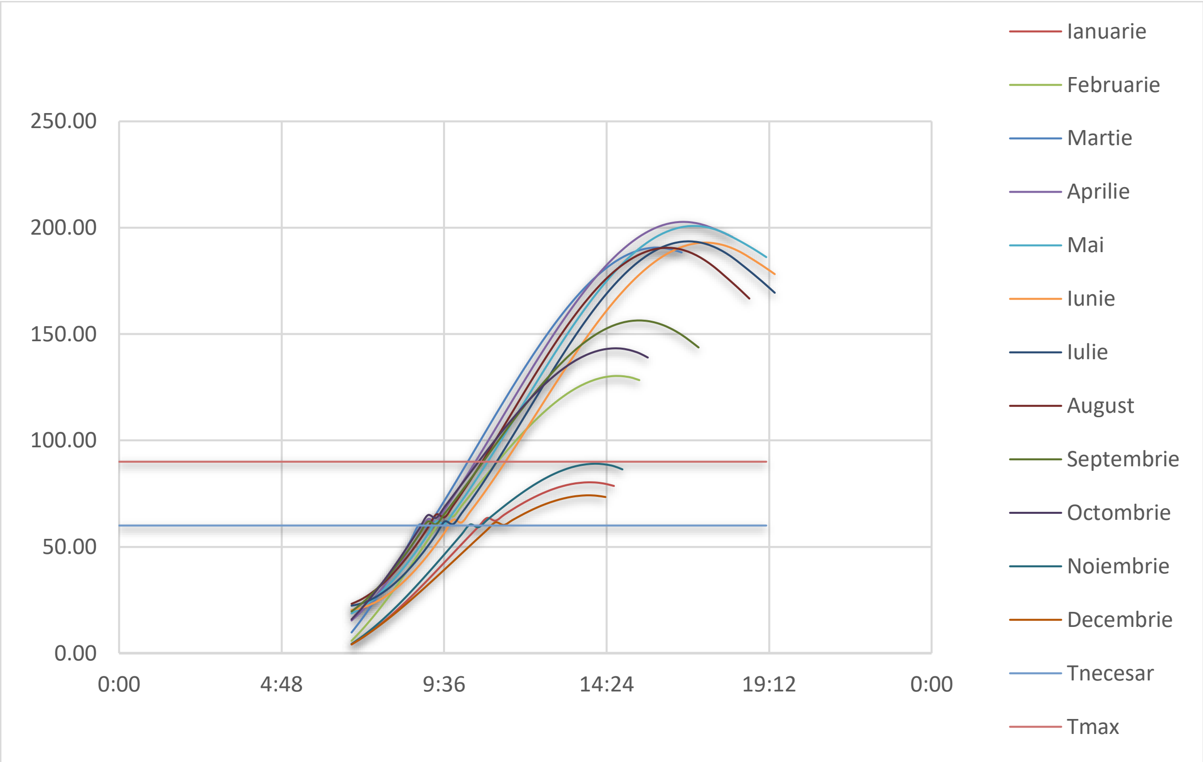

Fig. 8. Temperature variation in the installation tank

It can be seen that the temperatures reach values approximately equal to 210 °C.
To avoid overheating, the network of solar collectors must be equipped with an automatic shading system. This system has a trigger temperature of 90 °C.

4. Comparative study on the prices of the two installations

A comparative study was carried out on the approximate costs of achieving the desired installation.

Table 5: The price of the elements when using photovoltaic panels

Elements	Price
Complete set of photovoltaic panels x 12 (75 m^2)	41000 RON
Invertor x 1	1700 RON
Total (approximative)	**42700 RON**

Table 6: The price of the elements when using solar collectors

Elements	Price
Solar collectors x 24 pieces (60 m^2)	42000 RON
Tank	2600 RON
Circular water pump x 2	800 RON
Piping	70 RON/4 m
Water temperature sensor	40 RON
Total (approximative)	**45510 RON**

The difference in cost between the two types of solar collectors is acceptable, either of which can be used in an air treatment plant depending on the beneficiary requirements.

5. Conclusions

In the present paper, a theoretical study was carried out on the adaptation of photovoltaic panels and flat solar collectors to the air treatment plant (ATP), located in room CG126 within the Department of Thermotechnics, Engines, Thermal and Refrigeration Equipment's of the Faculty of Mechanical and Mechatronics Engineering, University Politehnica of Bucharest.
The fields of application described in this paper show the possibility of using solar collectors in a wide variety of systems. It can provide significant benefits to the environment and should be used whenever possible.
The useful collecting area to ensure a need of 4kW is large, and the investment price for an installation of photovoltaic panels or flat solar collectors is quite high.
The efficiency of solar energy capture installations (photovoltaic panels, flat solar collectors) is closely related to the geographical region in which it is to be located. Both the angle of inclination and the altitude at which it is located must be calculated so that the exposure to the sun's rays is as high as possible throughout the day.
Due to the complexity and lower investment costs, the use of photovoltaic panels is more advantageous than that of flat solar collectors.

Acknowledgments

This work was supported by a grant of the Romanian Ministry of Research and Innovation, CCCDI-UEFISCDI, project number PN-III-P1- 1.2-PCCDI-2017-0406/ NR. 81PCCDI / 2018 "Tehnologii inovative de producere a energiei regenerabile din surse naturale integrate în instalații complexe", within PNCDI III.

References

[1] Kreith F, and J.F. Kreider. *Principles of solar engineering*. New York, McGraw-Hill, 1978.
[2] Kalogirou, Soteris A. "Solar thermal collectors and applications." *Progress in Energy and Combustion Science* 30 (2004): 231–295.
[3] https://www.ventilatierecuperarecaldura.ro/1045-large_default/baterie-incalzire-electrica-rectangulara-vents-nk-400x200-105-3.jpg, accessed June 23, 2019, at 13:14.
[4] http://www.calorserv.ro/images/products/imported/14524-baterie-de-incalzire-pe-apa-nkw.jpg/14524-baterie-de-incalzire-pe-apa-nkw.jpg, accessed June 23, 2019, at 13:20.
[5] https://www.wattrom.com/wp-content/uploads/2017/10/data-sheet-WT-60P-S17_250W-RO.pdf, accessed June 24, 2019.
[6] http://www.secpralpro.ro/Images/Produs/00000618/00001187_large.jpg, accessed June 24, 2019.
[7] https://www.sistemepanourisolare.ro/pdf/panou-solar-plan-sunsystem-select-pk-20/382.
[8] Photovoltaic Geographical Information System http://re.jrc.ec.europa.eu/pvgis/apps4/pvest.php.
[9] https://www.komfovent.com/en, accessed June 24, 2019.

Design and Study of Hydraulic Systems

Dipl. Eng. **Mihai DIACONU[1],** PhD. Eng. **Tiberiu AXINTE[1],** Dipl. Eng. **Cătălin FRĂȚILĂ[1],**
Prof. PhD. Eng. **Paul BOCĂNETE[2],** Dipl. Eng. **Remus COJOCARU[3]**

[1]Research Center for Navy, Romania

[2]Constanta Maritime University, Romania

[3]Princess Cruises, U.S.A.

*tibi_axinte@yahoo.com

Abstract: *In this paper, the electro-hydraulic schemes are made with the FluidSim software from Festo. Electro-hydraulic circuits are used in transport, construction, research, etc. It is very important that in some emergencies, people's lives depend on some electro-hydraulic systems (e.g., launching systems from lifeboats). We present at the beginning the main components that are used in electrical (switches, relays) and hydraulic circuits (compressors, hydraulic cylinders, distributors, etc.). Next, the electrical and hydraulic circuits are made and studied separately. At the end of the paper, we designed and studied simple and complex electro-hydraulic schemes. These electro-hydraulic systems can be used in unfavourable weather conditions, for example, some cranes on a fishing vessel that use electro-hydraulic systems. These cranes can be used in cold, strong wind or storm fishing conditions.*

Keywords: *FluidSim, hydraulic, electrical, scheme, circuit, valve*

1. Introduction

In practice, electro-hydraulic systems are generally used for lifting or lowering heavy materials. The transmission of hydraulic energy in the electro-hydraulic circuit is done through mineral oils. The mineral oils used are: without additive, with additives and with additional additives.

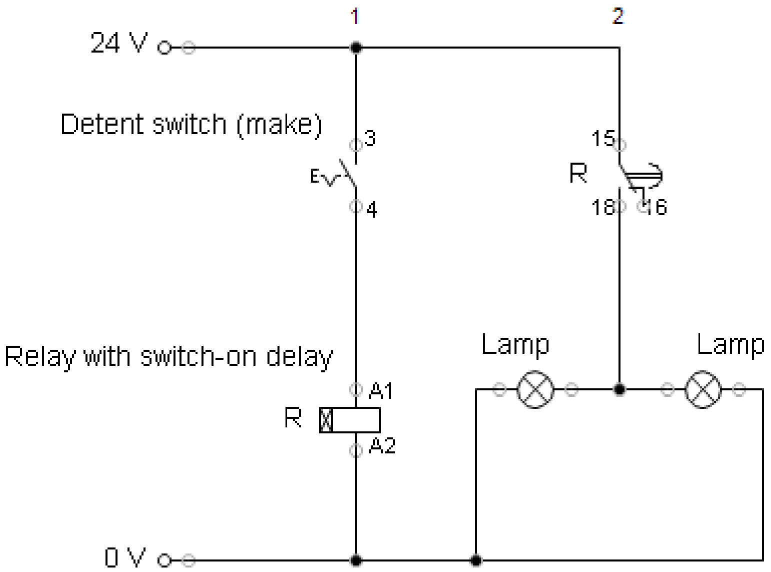

Fig. 1. Simple electrical scheme

The most important properties of oils are viscosity and density.
The oils of type H19, H35 or H57 can be used for the electro-hydraulic circuits presented in the paper.
Electro-hydraulic systems are used for cranes, elevators, jacks, etc. The electro-hydraulic scheme is made of two parts:

- Electrical scheme.
- Hydraulic scheme.

Relays, pushbuttons, electrical connection, make switch, light bulbs (lamps), etc. are used for electrical schemes.
Pump unit, hydraulic cylinders, distributors, etc. are used for hydraulic schemes.
In the diagrams made in this article, parts manufactured by Festo can be, [1].
The simplest electrical diagram is made of a light bulb and a battery.
In this paper, the simple electrical circuit is connected to an alternating current source consisting of: detent switch (make), relay with switch-on delay and two lamps, Fig.1.
If we press the detent switch, the electric current enters through the simple circuit, Fig. 2.

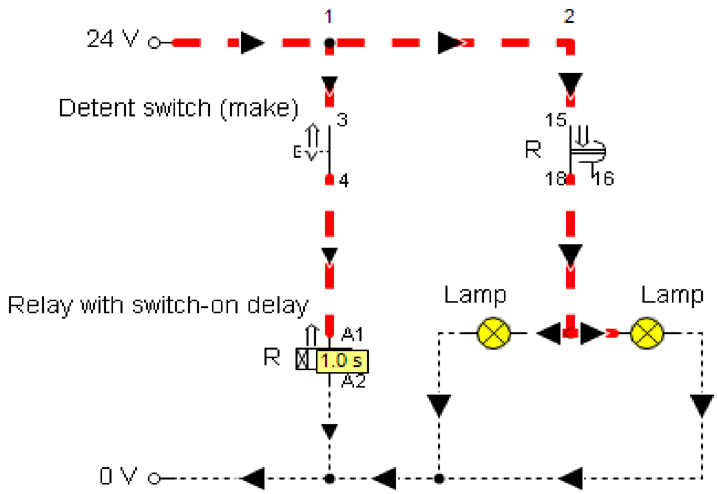

Fig. 2. Simple open electrical circuit

The electrical circuit is equipped with two lamps. These lamps light up simultaneously when current flows through the circuit, Fig. 2.

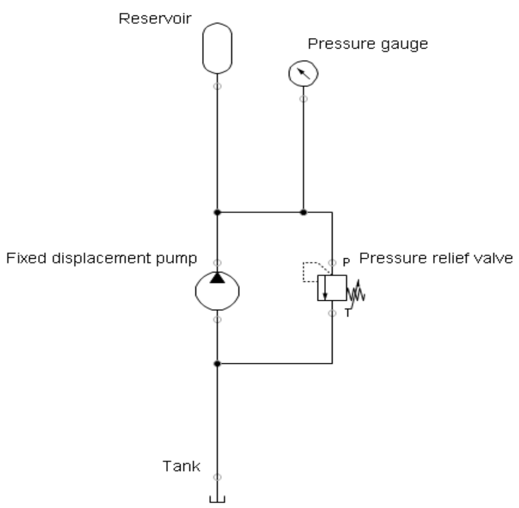

Fig. 3. Simple hydraulic scheme

The simple hydraulic circuit in the article is composed of tank, fixed displacement pump, reservoir, pressure gauge and pressure relief valve, Fig. 3.
If we start the pump, then the fluid in the tank moves into the tank and pressure relief valve.
Pressure gauge records the pressure in the hydraulic circuit. At this point, the circuit pressure is P_c = 3.46 MPa, Fig. 4.

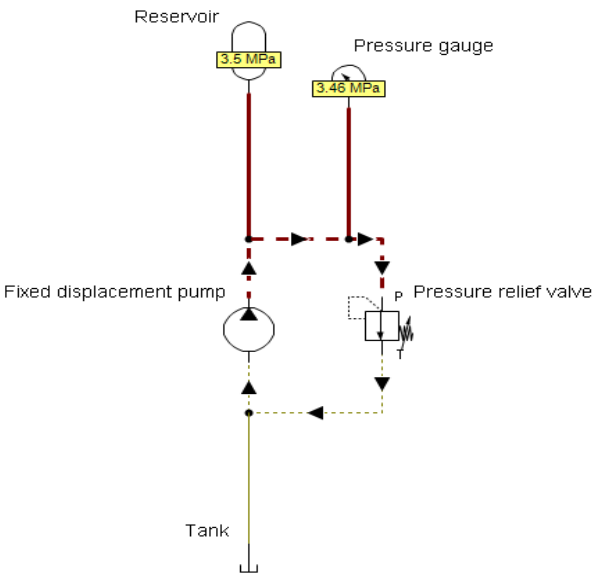

Fig. 4. Simple open hydraulic scheme

2. The main devices

All electrical and hydraulic circuits are made of main components. The electrical diagrams may contain the following basic components: pushbutton, make switch, pump unit and hydraulic reservoir.

1) Pushbutton (make)

Fig. 5. Pushbutton

Description	Symbol
That switch closes when actuated and opens immediately when released.	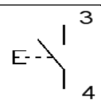

2) Make switch (switch-on delayed)

Fig. 6. Make switch

Description	Symbol
Switch that delayed closing after pickup. Switch-on delayed make switches are created by using a general make switch and setting a label.	

An electric current is a flow of electric charge. The equation in circuit is, [2]:

$$I = \frac{\Delta Q}{\Delta t} \tag{1}$$

Where:

- I – current flowing.
- ΔQ – the change in electrical charge.
- Δt – the change in time.

Pneumatic diagrams may contain the following basic components:

3) Pump unit (simplified)

Fig. 7. Pump unit

Description	Symbol
A pump unit is a device that moves liquid by mechanical action, typically converted from electrical energy into hydraulic energy.	

In the hydraulic circuit, using pump unit and the Bernoulli’s equation is valid, [3]:

$$P + \rho g h + \frac{\rho \vartheta^2}{2} = constant \qquad (2)$$

Where:

- P – pressure
- ρ – density
- g – the acceleration due to gravity
- h – the elevation
- ϑ – velocity

4) Hydraulic reservoir

Fig. 8. Hydraulic reservoir

Description	Symbol
The reservoir enables the performance of a hydraulic system to be optimized. It can be used as an energy reservoir and for the absorbance of pressure surges or flow fluctuation.	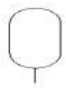

3. The electro-hydraulic systems

In this paper, we make two electro-pneumatic schemes. The controls in this circuit are electric. The pressure in the compressor is 0.6 MPa (6 bar). The first electro-hydraulic scheme in the paper aims to move a piston from the hydraulic cylinder. This piston is equipped with adjustable cushioning. [4].

The hydraulic cylinder (piston diameter-16mm, piston rod diameter-10mm, maximum stokes - 200 mm) is of type double acting cylinder, Fig. 9.

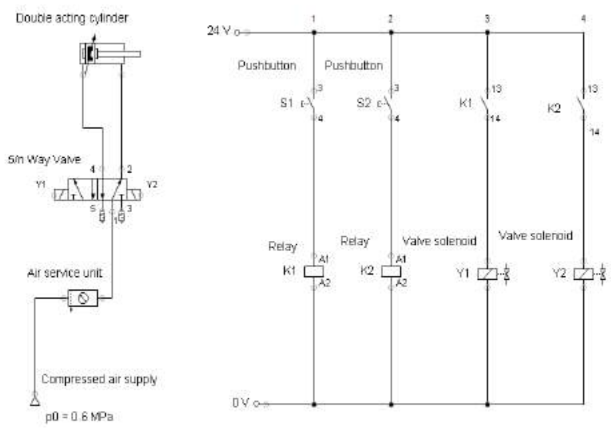

Fig. 9. Electro-hydraulic scheme – Case 1

To open the electro-hydraulic circuit we must press the S1 button. Then the piston moves to the right, Fig. 10.

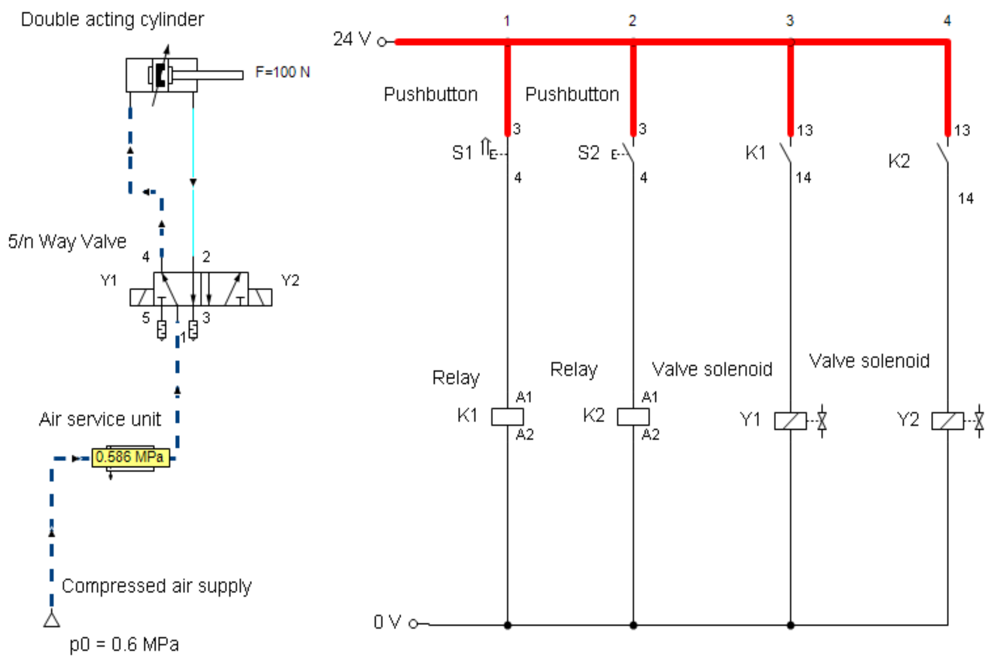

Fig. 10. Electro-hydraulic circuit opening – Case 1

To close the electro-hydraulic circuit, we must press the S2 button. Then the piston moves backwards, figure 11, [4].

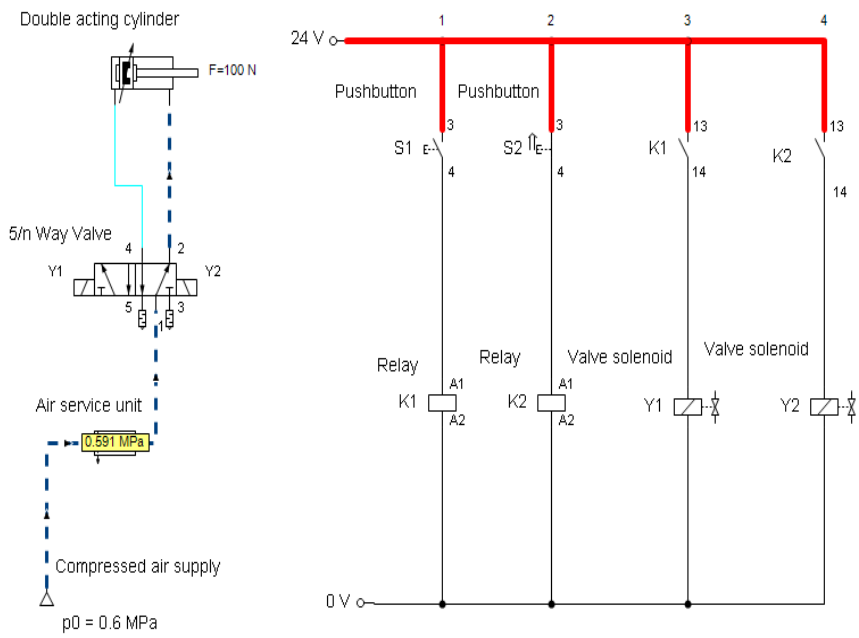

Fig. 11. Closing the electro-hydraulic circuit – Case 1

In the second case, we used an air tank, compressor, a hydraulic, a throttle and two distributors. For case 2, the piston has the same dimensions as in case 1. However, the piston has not adjustable type cushioning, Fig. 12.

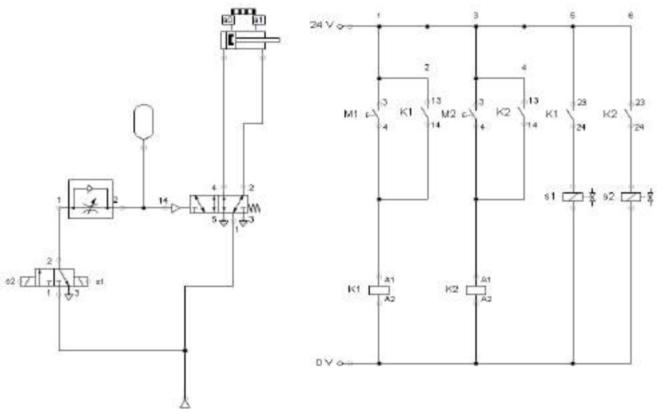

Fig. 12. Electro-hydraulic scheme – Case 2

In the case 2, at the hydraulic cylinder, the piston moves from a0 to a1. To do this, press the M1 button, Fig. 13.

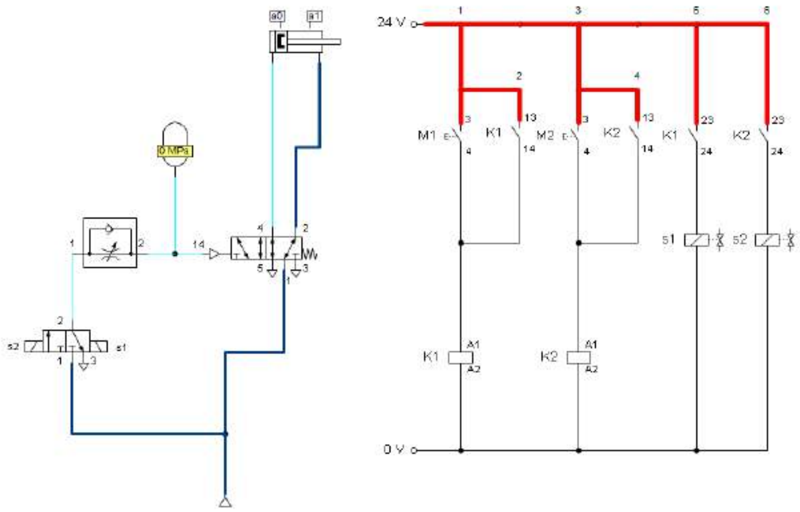

Fig. 13. Electro-hydraulic circuit (press M1 button) – Case 2

To move the piston from a1 the a0, press the M2 button, Fig. 14, [5].

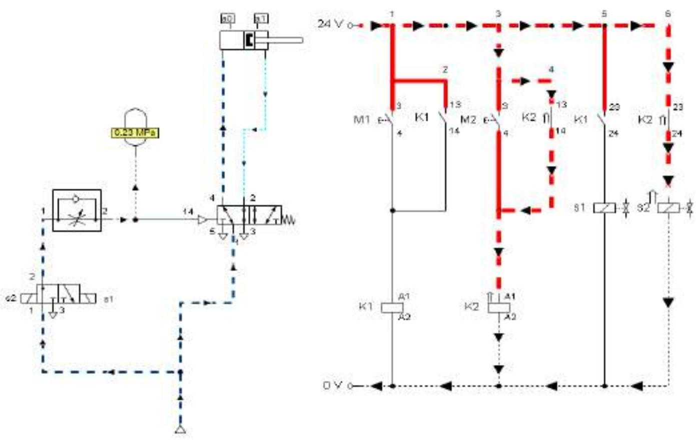

Fig. 14. Electro-hydraulic circuit (press M2 button) – Case 2

The parameters of the cylinder from the case 2: position (x) and velocity (v), Fig. 15.

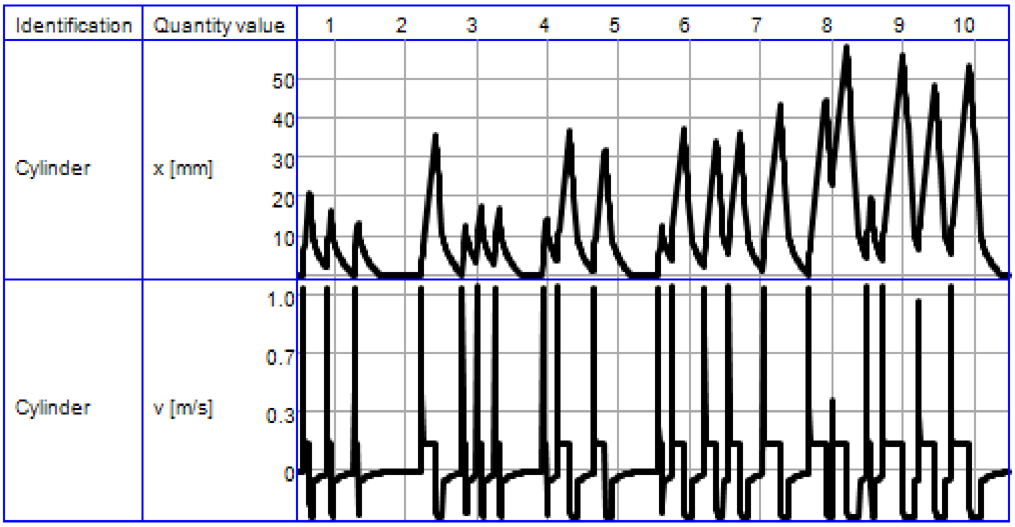

Fig. 15. Diagrams from cylinder – Case 2

3. Conclusions

Regarding the schemes presented in this paper the complex electro-hydraulic circuits can be developed. From these electro-hydraulic schemes other electrical or hydraulic schemes can be further developed. The advantage of electro-hydraulic schemes made in the FluidSim software is that circuits with good quality electrical and hydraulic devices (e.g. Festo products) can be used in practice. The advantage is the electro-hydraulic schemes that are made in a timely manner. Changing the schemes to achieve optimal circuits can be done in a short time.
In the future, we would like to develop electro-hydraulic schemes in the FluidSim Software that will work at better yields.

References

[1] Ebel, F., and Ch. Loffler. *Electrohydraulics, basic level TP 601: Workbook*. Edition 03/2016, Festo Didactic.
[2] Ciucur, V. "Current control for stepper motor operation." *Journal of Marine Technology & Environment* 2, (2020): 13-16.
[3] Degeratu, M. *Dimensional analysis, similarity and modeling. Guide for applications in Fluid Mechanics and Hydraulics / Analiză dimensională, similitudine și modelare. Îndrumar pentru aplicații în mecanica fluidelor și hidraulică*. Bucharest, Publishing House of the Romanian Academy of Scientists, 2015.
[4] Nicolae, I., and T. Dordea. "Lift of hydraulic powered materials and driven by a programmable Automatic." Paper presented at International Conference on Hydraulics and Pneumatics HERVEX 2019, Baile Govora, Romania, November 13-15, 2019.
[5] Fratila, C., T. Axinte, R.C. Cojocaru, C. Berescu, and I.C. Scurtu. "The study of the lifting mechanism of the crane arm to a barge." Paper presented at the Technium Conference, Constanta, Romania, December 15, 2019. *Technium: Romanian Journal of Applied Sciences and Technology* 2, no. 1 (2020): 91–96. https://doi.org/10.47577/technium.v2i1.47.

ISSN 1453 – 7303 "HIDRAULICA" (No. 2/2021)
Magazine *of Hydraulics, Pneumatics, Tribology, Ecology, Sensorics, Mechatronics*

Rainwater Harvesting, a Solution to Reduce Drinking Water Consumption for Buildings

Assoc. Prof. Dr. Eng. **Adriana TOKAR[1],** Dipl. Eng. **Paul FRASIE[2],**
Res. Asst. PhD. student Eng. **Dănuț TOKAR[1]**

[1] Politehnica University Timisoara, Faculty of Civil Engineering, adriana.tokar@upt.ro

[2] Pinchin Ltd., Canada, paul.frasie@yahoo.com

[*] adriana.tokar@upt.ro

Abstract: *Water consumption worldwide has increased considerably in recent decades and has a growing trend due to population growth in the coming years. Migration of the population from rural areas to urban areas will lead to problems arising from water insufficiency in crowded areas. Urban areas are oftentimes up to 8°F warmer than the surrounding rural area, creating "urban heat islands". In densely populated areas where more water is consumed, an important consideration would be whether a part of the urban water requirement can be covered by rainwater harvesting. First, rainwater harvesting helps to conserve water by reducing the amount of water needed for toilet (and urinal) flushing, and outdoor watering. The article analyzes the water consumption averaged between years 2015 and 2017 (thermal power plants, humidifiers, and plumbing) for a 25- stories building located in Canada. Based on the analysis, it was found that the combined seasonal average for the spring and summer was 62% higher than the winter and fall seasons. By using rainwater instead of potable (drinking) water for these applications, homeowners can reduce their daily water use by approximately 30%.*

Keywords: *Rainwater Harvesting, Reducing Water Consumption, High Buildings, Measures and Recommendations*

1. Introduction

"Humanity has the ability to make development sustainable to ensure that meets the needs of the present without compromising the ability of future generations to meet their own needs", is definition from Brundland Commission's report "Our Common Future (WCED), 1987.

Increased of world population in the next years will affect natural resources consumption. As a result, water consumption will increase with the same pace with the demographic increased and shall create problems like water scarcity in the urban areas. Meanwhile, water supply systems face water loss caused by both the age of pipes and system optimization issues such as pressure loss in the water network.

The study of economic profitability and various pressure control are required to establish the ways to take for the water network upgrades in the urban areas. This will meet the safety water consumption and protect the natural resources.

Natural resources management is a global concern and a priority for the lasting development. The population are in the center of this development. The understanding of population global trends and the next demographic changes are crucial to establish the objectives of lasting development for 2030. The right projections and forecast for the population water consumption will allow the government to anticipate future demographic trends and to include that information in their planning policies for 2030 [1]. Table 1 shows important data related to world population trend from EU and Romania [1]. The probabilities forecast was conducted on 80% and 90% samples.

Table 1: Total population by world, EU and Romania, annually for 1950-2100 [1]

No.	Total population (thousands)							
	Standard Projections (Estimates and Projection variants) 2015-2020 reported to the year							
	Area	1995	2015	2016	2017	2018	2019	2020
1	World	2.536.43	7.379.79	7.464.02	7.547.85	7.631.09	7.713.46	7.794.79
2	Europe	549.32	743.05	744.26	745.41	746.41	747.18	747.63

3	Romania	16.236	19.925	19.796	19.654	19.506	19.36	19.23
Probabilistic Projections (including prediction intervals)									
	Area	2030	2040	2050	2060	2070	2080	2090	2100
1	World	8.548.48	9.198.84	9.735.03	10.151.47	10.459.24	10.673.90	10.809.89	10.875.39
2	Europe	741.30	727.81	710.48	688.79	666.59	649.58	638.36	629.56
3	Romania	18.30	17.30	16.26	15.17	14.12	13.25	12.53	11.87

Table 1 shows that from 1995 to 2018 the population increase in all analyzed areas (i.e., Worldwide, Europe, Romania); after 2018 the forecasts show a Worldwide population increase, a slow population decrease in Europe and a concerning decrease population in Romania. If you look at 1995 forecast only, the population increased trend is the same in EU and Worldwide, meanwhile in Romania the concern stays the same. One of the most concerning issue is the fact the next decades will have the highest urban increase rate in human history, with 2.6 billion additional inhabitants until 2050. All the addition inhabitants will need water, but more importantly, there is not too much information about big cities water management and how the infrastructure affects global hydrologic cycle [2]. The adaptability to the recent challenges regarding the environment and water systems associated with the buildings is crucial. Rainwater harvesting plays a major role [3, 4, 5].

2. Influence of using stormwater

Stormwater contains pollutants and nutrients which can endanger soils, groundwater and slowly flowing receiving water when it is discharged.
The natural groundwater regeneration is influenced by the high degree of sealed surfaces and therefore, water bodies are considerably burdened as a result of the direct rainwater discharges. [6]
Paved surfaces (such as highways, roads, runways, parking areas, sidewalks, and driveways) typically constitute about 30 to 40% of developed urban areas. In the past few decades, the bane of urban cities has been the increased heating of the city by sunlight due to dark, heat-absorbing materials used in the construction of pavements and buildings. Urban areas are oftentimes up to 8°F warmer than the surrounding rural area, creating "urban heat islands" [7]. In densely populated areas where more water is consumed, an important consideration would be whether a part of the urban water requirement can be covered by rainwater harvesting, and whether traffic and other surfaces, in addition to roof surfaces, can be used for rainwater catchment. In this case, rainwater need not be drained into the sewer. This will result in an upgrading of the water quality, since urban surface water bodies are increasingly negatively affected by rainwater discharges and overflows mainly from the combined sewer. [6]
Rainwater harvesting has several benefits. First, rainwater harvesting helps to conserve water by reducing the amount of water needed for toilet (and urinal) flushing and outdoor watering. A new approach for the plumbing design to integrate and use the rainwater harvesting will drive to drinking water reduction and also to natural resources preservation. Studies show that using rainwater will reduce the drinking water consumption. [8,9,10]. Using this concept, the plumbing design will take into consideration plumbing fixtures that require potable water and those that don't require drinking conditions [3, 4, 5, 11]. By using rainwater instead of potable (drinking) water for these applications, homeowners can reduce their daily water use by approximately 30%. Secondly, rainwater harvesting can improve ecosystem health and reduce river and stream erosion by means of managing stormwater runoff. For instance, in Province of Ontario Canada, the approved uses for rainwater are for toilet flushing, urinal flushing, and outdoor use (hose taps and irrigation system). In contrast, uses rainwater for washing machine, shower and baths, cooking and drinking, lavatory faucets, et cetera are prohibited [12]. The article analyzes the water consumption averaged between years 2015 and 2017 (thermal power plants, humidifiers, and plumbing) for 25 stories building, located in Canada.

- ***Water Conservation***

The water-using systems in use for the multi stories building consist of the following: kitchen faucets, bathroom faucets, toilets, and urinals. The following tables (Table 2) quantifies domestic water fixtures in place.

Table 2: Conventional Domestic Water Systems Inventory for the 25 stories Building

Floor	Toilets	LPF	Urinals	LPF	Faucet	LPM	Custodial Sink	LPM	Kitchen Faucets	LPM
Typical Floor (14 Floors)	6	6	2	3.8	4	8.3	1	8.3	1	8.3

Table 3: Upgraded Domestic Water Systems Inventory for the 25 stories Building

Floor	Toilets with Sensors	LPF	Urinals with Sensors	LPF	Faucets with Sensors	LPM
Typical Floor (10 Floors)	6	4.8	2	1.9	4	1.9
Lobby	6	4.8	1	1.9	3	1.9

Figure 1 illustrates the estimated water consumption breakdown of a multi-tenant building based on the following sources and assumptions:

- Normalized sub-metered water data provided by the client July to November 2018 for the cooling tower, humidification, irrigation and DHW supply systems;
- Plumbing fixtures found on site;
- Typical water use patterns and typical distribution of office building water consumption.

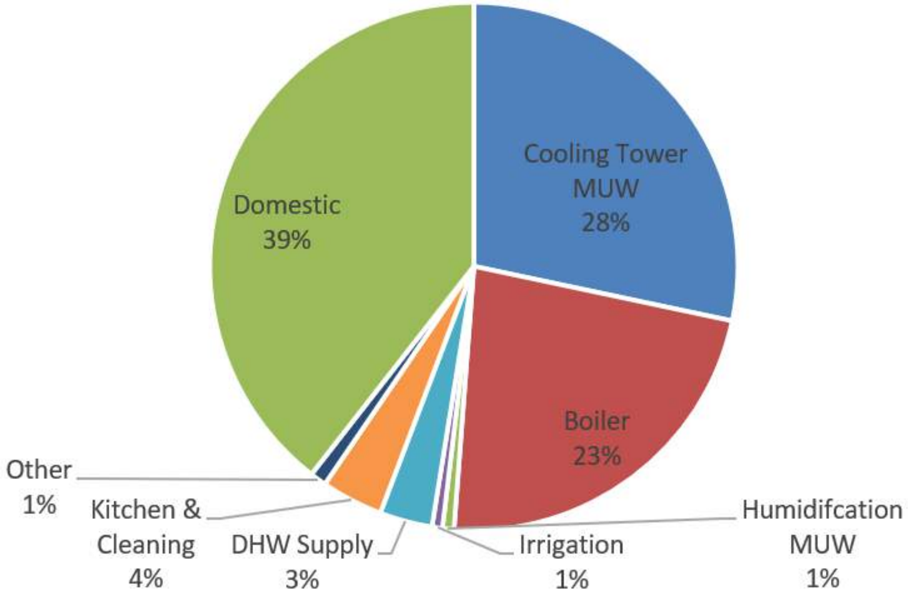

Fig. 1. Estimated Breakdown of Annual Water Consumption

Water conserving measures are expected to reduce water costs and wear and tear within water consuming systems. Table 4 lists water conservation recommendations for the building.

Table 4: Water Conservation Recommendations

Equipment Type	Issue	Recommendation	Section
Cooling Tower	Higher efficient cooling towers are now available that can possibly use rainwater harvesting.	Full cooling tower performance review and system design review at the end of their typical life prior to replacement.	3
Humidification	Humidifier may not be performing at optimal efficiency	Full humidifier performance review and system design review at the end of their typical life prior to replacement	3

- ***Water Consumption***

The data recorded for the period 2015-2017 regarding the annual and monthly consumptions are presented in figures 2 and 3, as follows: Figure 2 provides a summary of annual water data for the period from 2015 to 2017 and Figure 3 provides a monthly summary for the Site building over the same time period.

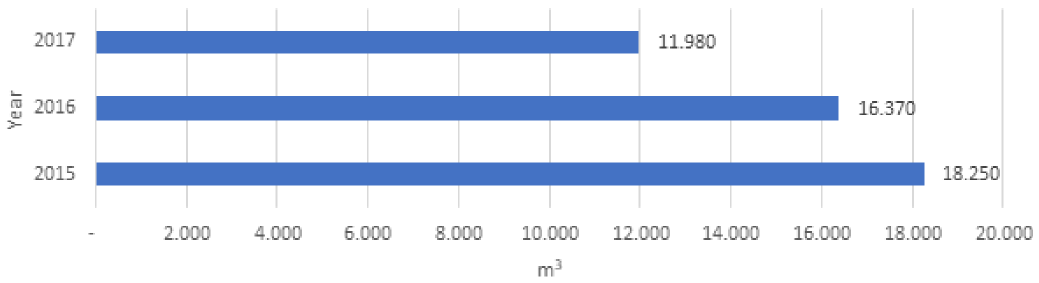

Fig. 2. Total Water Consumption

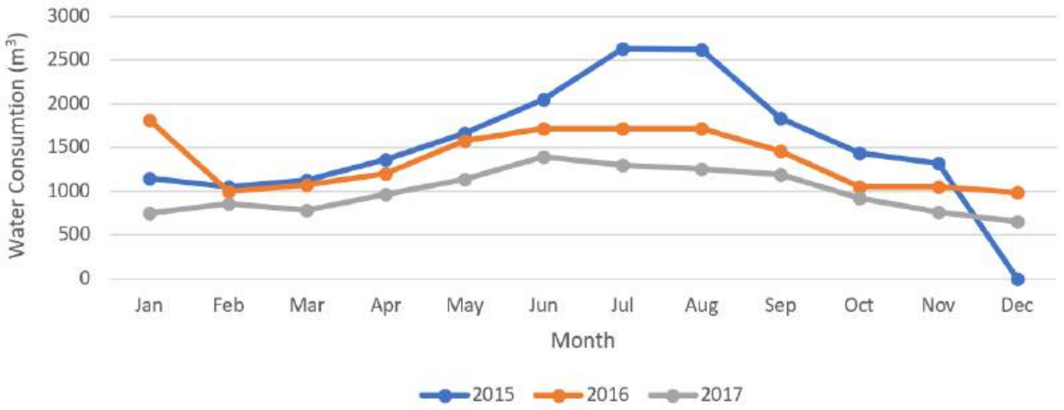

Fig. 3. Monthly Water Consumption

Water is used on Site for domestic hot water, boilers, humidification systems, and domestic systems. The average monthly consumption is 1.294 m^3. The seasonal averages were compared, with the fall and winter seasons having the lowest averages, 909 m^3 and 1067 m^3 respectively. The spring and autumn season averages were 1.453 m^3 and 1.749 m^3 respectively. The combined seasonal average for the spring and summer was 62% higher than the winter and fall seasons.

- ***Seasonal Water Consumption Analysis***

The water consumption of the Site building, averaged between 2015 and 2017, was determined to be 15.533 m^3 and hence can be used as the baseline benchmark. Figure 4 shows the trend correlation between water consumption compared against Heating Degree Days and Cooling Degree Days measured in degrees Celsius (°C) summed per month. Consumption peaks were observed in July and August of 2015 and January of 2016. General increases were observed in the spring and summer months of all years reviewed. Fluctuations of water consumption could have been attributed to many factors: the lack of a cooling tower system, office temperature preferences, potential shifts in occupancy of the Site building, installation of different fixtures, leaks, etc. Overall, the water consumption of the building correlates to the seasons.

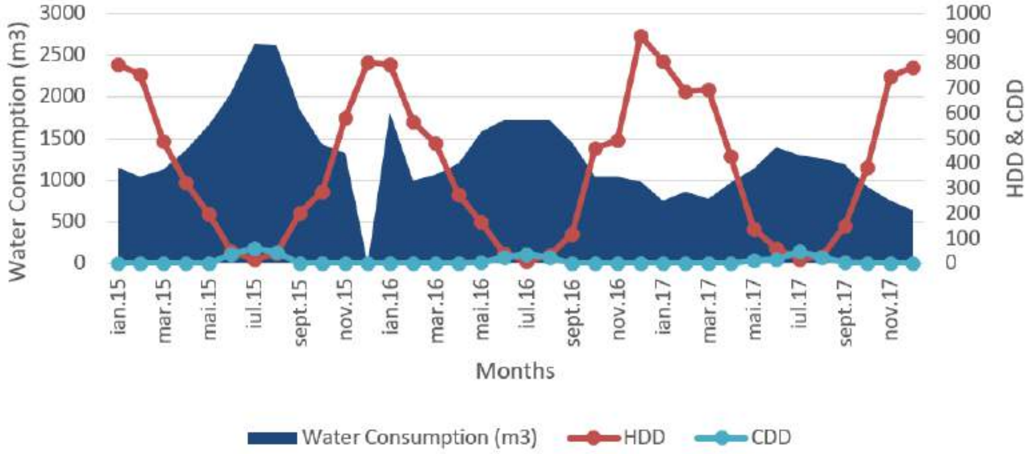

Fig. 4. Water consumption comparison of the building plotted against heating and cooling degree-days between 2015 and 2017

Figure 5, is a graphical representation of water consumption in relation to the increase in number of cooling degree days (CDD), at the Site building. From this graph, a slight decrease in measured water consumption can be seen to occur in relation to the measured number of cooling degree days. The correlation between consumption and CDD is expressed as the displayed value of R2 in Figure 5. Essentially, this represents the amount of water lost per increase in cooling degree day. The R2 value does not in any way represent how efficiently the system operates. On a scale of 0% to 100%, the relation between water consumption and CDD can be expressed as 47%, which indicates moderate correlation. The correlation is expected as the building does possess cooling towers.

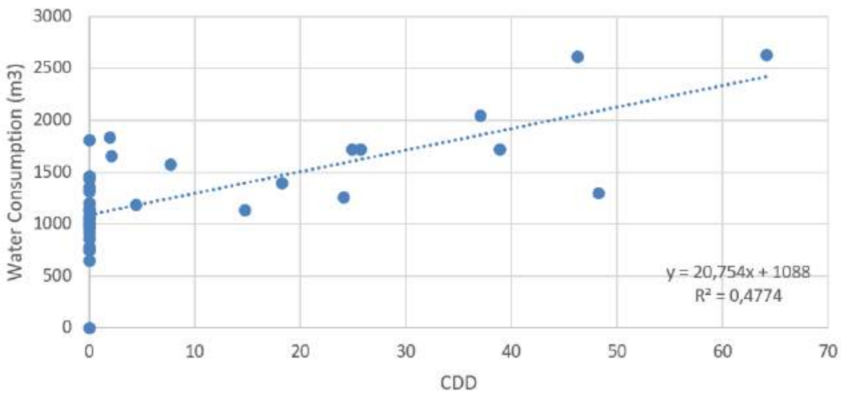

Fig. 5. Water Consumption and Cooling Degree Day Regression Analysis

3. Water Conservation Measures and Recommendations

- ***Cooling Tower Systems***

The cooling tower blower fan unit in use is using a VFD control system. The VFD control system significantly reduce the amount of energy consumed by this unit by reducing its operating speed and operating capacity in relation to the amount of measured cooling demand within the facility. This could be better accomplished using a slide scale algorithm to intercept the linear relationship

between two plotted points and determine the required fan operating capacity. Note: BAS contractor shall confirm the cooling tower operation.
Cooling towers require continuous make-up water to account for losses due to evaporation and drift. A key parameter used to evaluate cooling tower operation is "cycles of concentration" (sometimes referred to as cycles or concentration ratio). This is calculated as the ratio of the concentration of dissolved solids (or conductivity) in the blowdown water compared to the make-up water. Since dissolved solids enter the system in the make-up water and exit the system in the blowdown water, the cycles of concentration are also approximately equal to the ratio of volume of make-up to blowdown water. Many systems operate at two to four cycles of concentration, while six cycles or more may be possible. Increasing cycles from three to six can reduce cooling tower make-up water by 20% and cooling tower blowdown by 50%.
The use of rainwater harvesting as the main or partial source of make-up water has become increasingly common for industrial and commercial cooling tower applications. Rainwater, however, must be properly assessed and tested for nutrient presence.

- ***Humidification Systems***

The Gas Steam Humidifier will periodically "blowdown" or skim water from the tank to reduce the concentration of total dissolved solids that accumulate during long-term operation. An important parameter used to evaluate humidifiers operation is "hardness of the water". Due to the wide range of water conditions, it is important that the blowdown is set according to the local water conditions. By water conditions we are referring to the hardness of the water supplied to the humidifier.

- ***Domestic Systems***

Based on the information gathered from the domestic water system audit, the majority of urinals, toilets, and lavatory faucets are conventional ones.
The Site buildings can reduce water if they update the remaining domestic toilets, urinals, and faucets to highly efficient/low flow options (<4.8 LPF, <1.5 LPF, and <1.9 LPM respectively).

- ***High Efficiency Bathroom Faucets***

High efficiency bathroom faucets consume 1.9 LPM of use, significantly lower than that of conventional faucets. As shown in Table 2 and Table 3, the Site building currently makes use of conventional and 2.39 lpm bathroom faucet fixtures. Converting all the conventional and 2.39 LPM faucets to high efficiency faucets would reduce the associated water consumption.

- ***High Efficiency Kitchen Faucets***

High efficiency kitchen faucets consume 5.7 lpm and conventional kitchen faucets consume 8.3 lpm. As shown in Table 2, the Site building currently makes use of 6.76 lpm kitchen faucet fixtures. Converting the 6.76 LPM kitchen faucets to high efficiency faucets would reduce the associated water consumption.

- ***Low Flow Regulators in Urinals***

High performance low water urinals, complete with a pressure compensating internal flow regulator, consume 1.5 liters of water per flush (LPF), which is lower than the current 3.8 liters of water per flush (LPF) for the urinals on floors 11-25. Converting the conventional urinals to high efficiency would reduce the associated water consumption.

- ***High Efficiency Toilets***

High efficiency toilets consume 4.8 LPF of use, significantly lower than that of conventional toilets. As shown in Table 2 and Table 3, the Site building currently makes use conventional toilets with an assumed flow rate of 13.2 LPF on floors 11-25. Converting all the conventional toilets to low flow/high efficiency faucets would reduce the associated water consumption.

4. Conclusion

In the new urban setting, Rainwater harvesting can be considered a viable solution. This technology has the advantage of flexibility and simplicity of construction.
Stormwater recycling is likely to be of significant environmental benefit through the reduction of non-point source pollutant loads and the minimization of the requirement to build additional water supply infrastructure with increasing population densities. [1]
The paradigm of those rainwater harvesting systems refers to the stormwater quality, which is connected with the roofs, gutters, downspouts, water tanks and to the actual drinking water cost.

Regarding rainwater quality, the studies show that the correct design of the stormwater collection and storage will guarantee the use of water for nondrinking purposes (e.g., toilets, irrigation, etc.); however, a correct stormwater treatment will assure the use for drinkable purposes. Considering the price increase of drinking water and also the water scarcity in some areas, the implementation of government programs subsidies for both existing and new buildings will be a solution for rainwater harvesting. It is important to understand that the advantages of this technology will be beneficial for both the end user and the society.

References

[1] United Nations, Department of Economic and Social Affairs (DESA), Population Division. *World Population Prospects 2019*, Online Edition. Rev. 1, Published by the United Nations, 2019.
[2] McDonald, R. I., K. Weber, J. Padowski, M. Flörke, C. Schneider, P. A. Green, T. Gleeson, S. Eckman, B. Lehner, D. Balk, T. Boucher, G. Grill, and M. Montgomery. "Water on an urban planet: Urbanization and the reach of urban water infrastructure." *Global Environmental Change* 27 (2014): 96-105.
[3] Foris, D., A. Tokar, D. M. Tokar, and T. Foris. "A New Dimension on Sustainability of Tourism Destinations: The "Green Water" Program". Paper presented at the XI International Tourism Congress ITC'19, Funchal, Ilha da Madeira, Portugal, November 05 - 07, 2019. *Proceedings of International Congress 2019 – Abstract Book – The Image and Sustainability of Tourism Destinations*: 24-25.
[4] Tokar, A., D. Foriș, D. Tokar, and S. Popa-Albu. "Solutions for the Reuse of Rainwater in Indoor Plumbing." *Hidraulica Magazine*, no. 4 (December 2020): 51-58.
[5] Tokar, A., and A. Negoițescu. "Treatment Solutions for Rainwater Contaminated with Various Pollutants." *Analele Universității "Eftimie Murgu", Fascicula de Inginerie* XXII, no. 1 (2015): 405-414.
[6] Nolde, E. "Possibilities of rainwater utilization in densely populated areas including precipitation runoffs from traffic surfaces." *Desalination* 215, no. 1–3 (2007): 1-11.
[7] American Concrete Pavement Association. "R&T Update." *Concrete Pavement Research and Technology*, no. 3, (2002), https://www.equipmentworld.com, Accessed 08.04.2021.
[8] Bahri, A. *Managing the other side of the water cycle: Making wastewater an asset*. Publishing Elanders in Molnlyck, Sweden, 2009.
[9] Foris, D., M. Plesca, T. Foris, and D. Tokar. "Protecting sweet water Resources from Mountain Area through Ecological Investments in Tourism Industry." Paper presented at the 4th International Multidisciplinary Scientific Conference on Social Sciences and Arts SGEM, Sofia, Bulgaria, August 24 – 30, 2017.
[10] Foris, D., and M. Plesca. "Sustainable tourism through the protection of sweet water resources in montain area. " *Bulletin of the Transilvania University of Braşov* 10, no.1 (2017): 107-112.
[11] Itsukushima, R., Y. Ogahara, Y. Iwanaga, and T. Sato. "Investigating the Influence of Various Stormwater Runoff Control Facilities on Runoff Control Efficiency in a Small Catchment Area." *Sustainability* 10 no. 2 (2018): 407.
[12] Despins, C. *Ontario Guidelines for Residential Rainwater Harvesting Design and Installation Best Practices Manual* // Ontario's Building Code, Version1.0: 1-85, 2010.

Theoretical Possibilities of Using Building Integrated Wind Turbines for Urban Energy Production

Assistant professor **Fănel Dorel ȘCHEAUA**[1]

[1] "Dunărea de Jos" University of Galați, fanel.scheaua@ugal.ro

Abstract: *The wind energy potential is being used more and more all over the world today. This is auspicious because renewable resource is used for energy production, thus avoiding carbon emissions in the environment that come from burning fossil fuels. Vast wind farms fields have been developed in areas with wind potential and more recently marine areas are used for the installation of high-capacity wind turbines. In addition to these concerns of high-power applications, the concept of building integrated wind turbine for energy production of reduced power but which can be used in urban consumption is proposed, thus contributing to obtaining the title of city with green energy buildings. In order to achieve this goal, the aspects of space that must be occupied by the wind power plants must be considered, but also by the aspect of the building in architectural terms for the appropriate framing in the respective area. Thus, both criteria must be met in order to carry out such projects in urban buildings, which offer them advantages over classic buildings in terms of the energy production aspect based on environmentally friendly renewable sources.*

Keywords: *Wind turbine at buildings, three-dimensional modelling, CFD*

1. Introduction

The growing need for energy worldwide has led to the increasing use of fossil fuels which as we know have meant huge emissions of greenhouse gases into the atmosphere, which affects the environment in terms of increasing annual temperature values, rising sea levels by the accelerated melting of glaciers, which represent irreversible changes for the moment. The solution to mitigate these extreme phenomena would be to reduce these emissions globally. This goal is an ideal that is imposed by most world countries with high emissions level. One of the solutions is represented by the production of energy from renewable sources, which have registered an advance in recent years globally. For this reason sources of solar energy, wind, tidal or waves force are aimed to obtain green energy with a low impact on the environment for production.
In terms of wind force, it should be noted that applications have increased based on the use of high-power horizontal axis turbines both on land and more recently at sea with higher powers.
In order to supplement the energy production at city level, attempts have been made to install wind turbines in urban buildings as a means of bringing production closer to final consumers.

2. Mounting solutions for wind turbines on urban buildings

Different solutions for wind turbines mounting on urban buildings are presented, which have the possibility to bring an energy input by using the existing space on the roof. These methods are representing a viable alternative for urban areas that identify themselves as high energy consumers using the space on the roof that is available.
Regarding the typology of wind turbines used, both horizontal and vertical axis models can be used, depending on the possibilities existing at the working point where the assembly is performed. The wind speed, the direction as well as the period of action are considered in order to choose the turbine constructive type that is indicated to be used.
Examples of installation and use of wind turbines on the rooftop of buildings are shown in Figure 1.

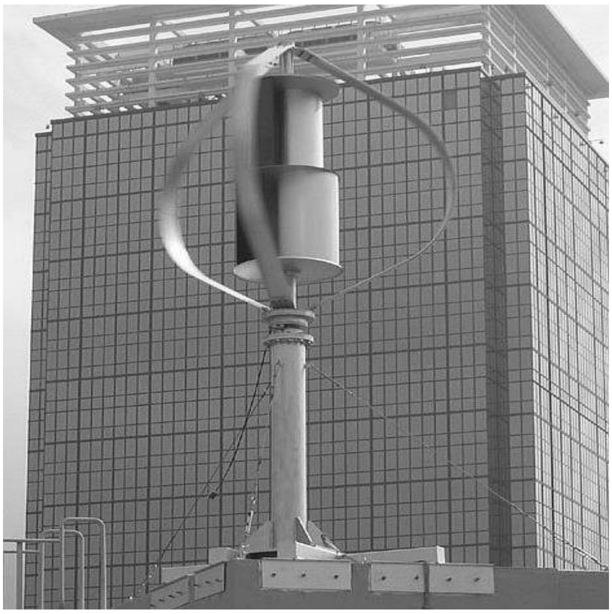

a) Hybrid vertical axis wind turbine

b) Darrieus wind turbine

c) Horizontal axis wind turbine

Fig. 1. Wind turbines mounted at rooftop of the buildings

In addition to the roof mounting of wind turbines, the process of including wind turbines in the building's own architecture is also used, thus forming an architectural model that also has the role of modern design that complements the energy aspect.

These architectural procedures represent modern trends in terms of building construction that bring an extra aesthetic and functional value to these buildings that attract attention through the state-of-the-art aspect (figure 2).

d) London Strata SE1 building

e) Bahrain world trade center

Fig. 2. Building integrated wind turbine

3. Vertical axis wind turbine model integrated at buildings

It is conceptually presented the process of installing wind turbines in urban buildings in order to produce energy and at the same time to be well integrated into the architecture of the building so as not to affect the appearance and aesthetics of the building.
The methodology that follows this principle refers to the use of wind turbines with vertical axis that present extensive mounting possibilities adaptable to large lengths both vertically and horizontally.
The wind turbines installation can be done both on the building corner side and also on the rooftop.
The endowment type is made for buildings located in suitable positions related to the continuous wind action that can be used for installation of the turbines.

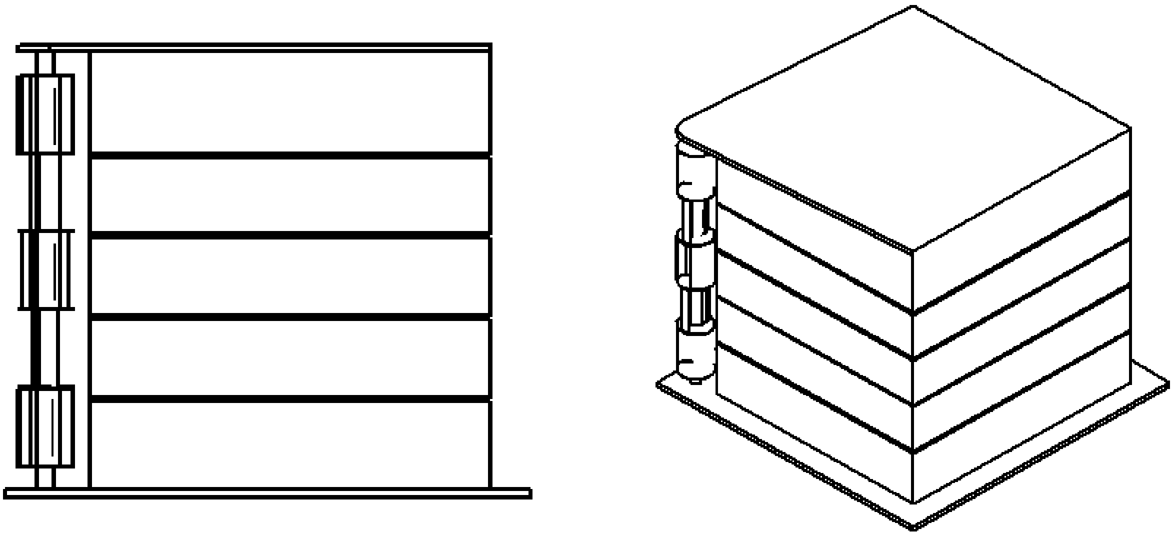

Fig. 3. Vertical axis wind turbine integrated on building corner concept

The mounting posibility of wind turbine system with vertical axis at the corner of a building is presented (figure 3). It represents a practical model for equipping buildings with wind power plants for energy production which can be applied to buildings located in areas with constant wind actions. This installation type of as well as the rotor typology proposed for installation also ensures an aspect that falls within the modern design norms increasing the architectural and aesthetic value of the respective building.

4. Wind action on the building virtual model

Using the building 3D model (figure 4), an analysis of the air flow is performed to show the main air flow rate stream that have the property of driving the wind turbine rotor in motion.

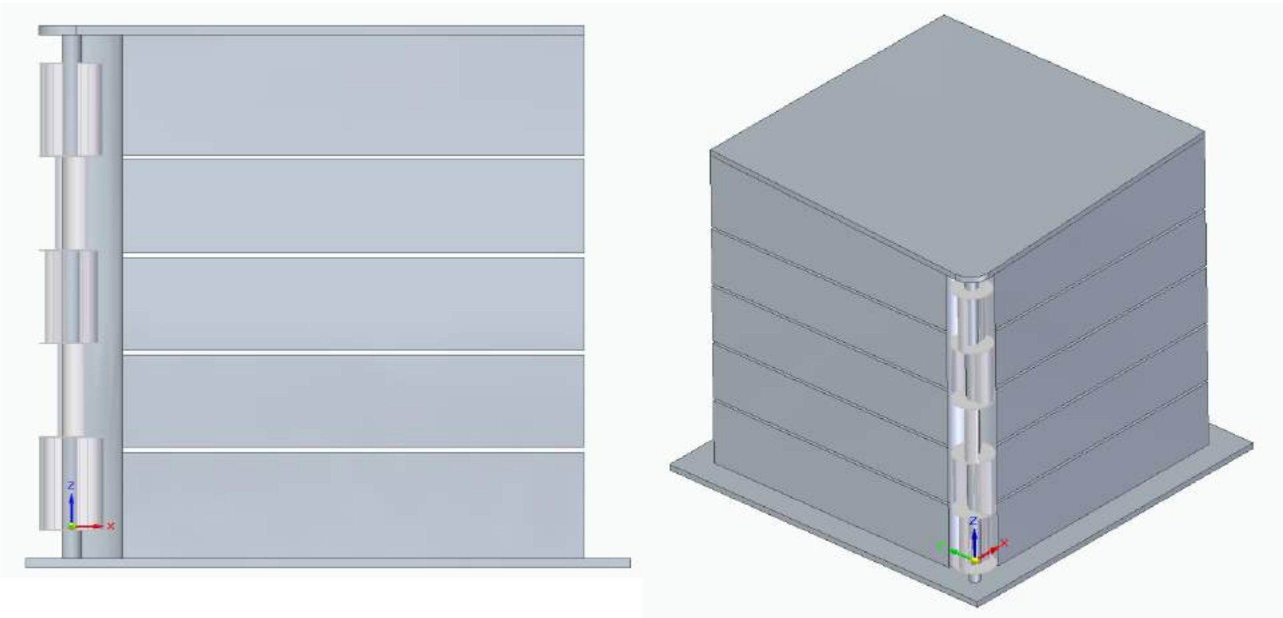

Fig. 4. Building with integrated wind turbine 3D model

The airflow analysis is performed with the Ansys CFX program performing the numerical simulation of air circulation at the building level and the appearance of the potential for the turbine rotor to move based on the wind force.
The working fluid is represented by air at 25 degrees Celsius with the k-Epsilon turbulence option for the fluid region.
Figure 5 shows the main domains of the analysis on the imported virtual model.

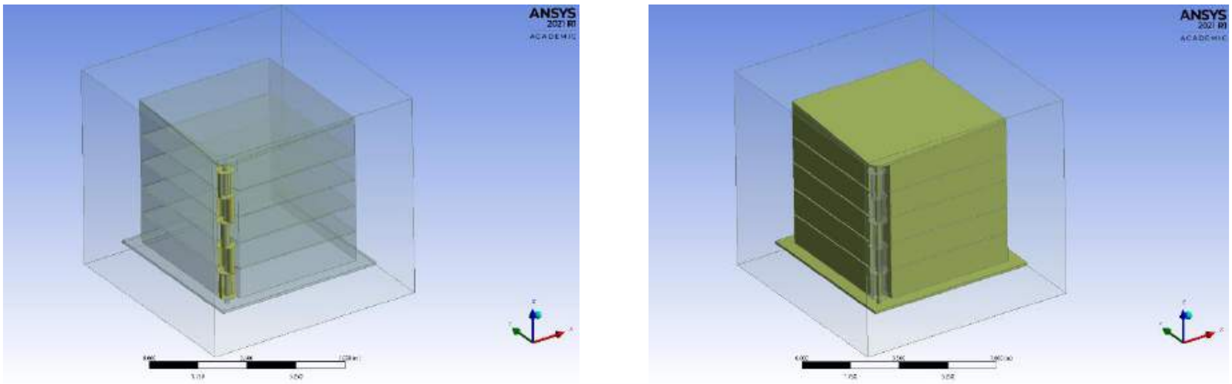

a) Wind turbine rotating domain b) Building solid domain

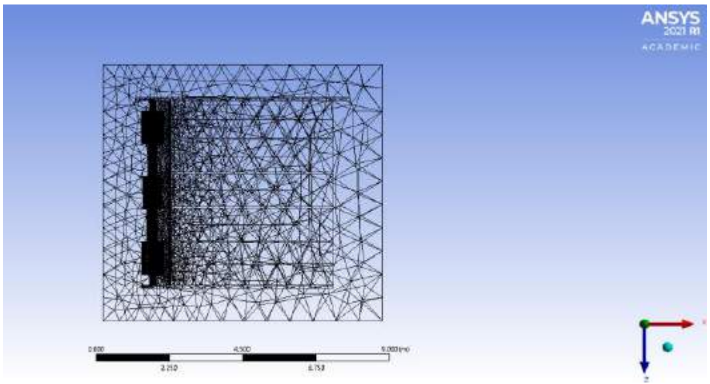

c) Mesh domain

Fig. 5. Flow analysis principal domains

Using the methods of numerical analysis on the virtual building model with vertical axis wind turbine embedded, the energy potential can be predicted based on the wind force for different values of the air circulation velocities.

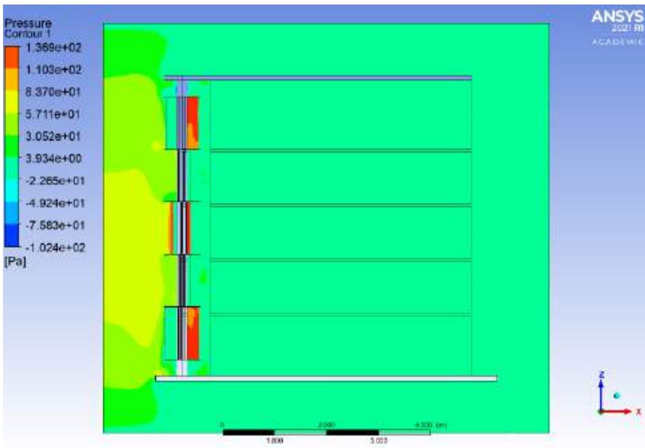

a) Pressure values

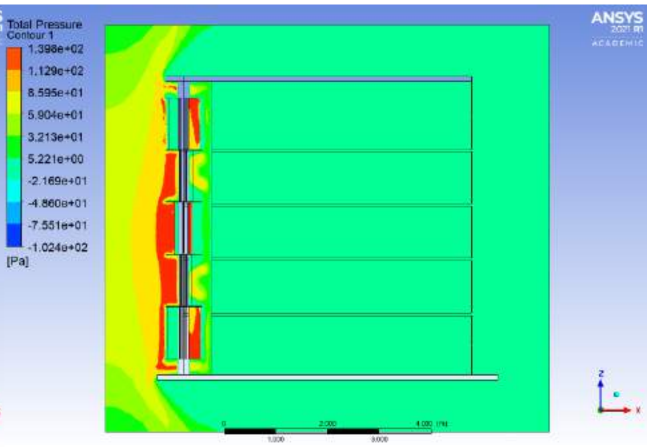

b) Total pressure values

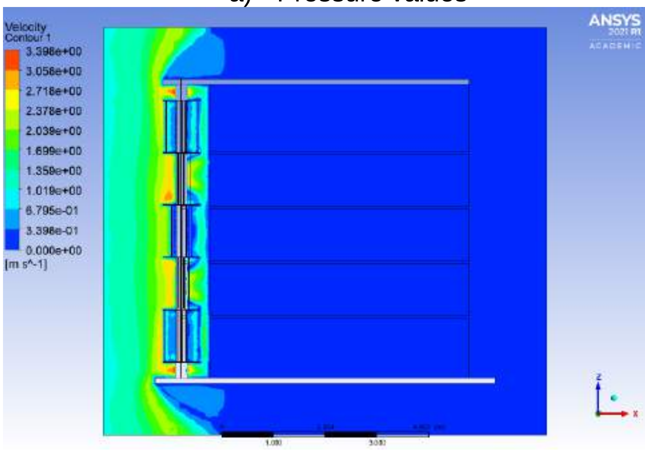

c) Air velocity values

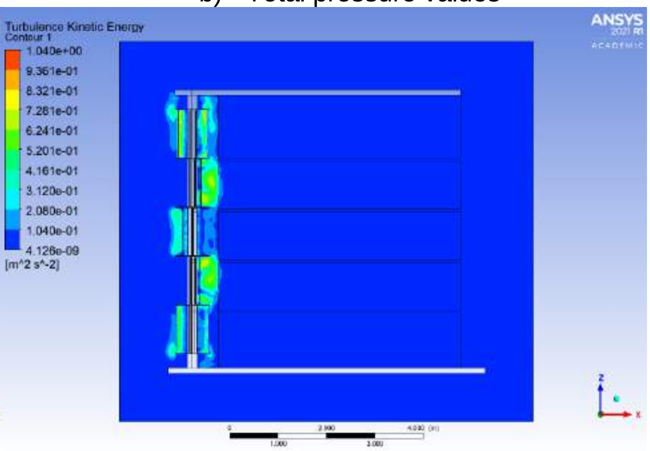

d) Turbulence kinetic energy values

Fig. 6. The obtained result values from air flow analysis

On the obtained results (figure 6), can be observed the main trajectory described by the air circulation at the building level acting directly on the building lateral wall but also on the turbine rotor which is positioned integrated on the building corner. For a better air circulation and an improved action of the rotor can be adopted a curved shape of the building facade that would direct the main air flow on the turbine rotor blades thus ensuring better results.

5. Conclusions

When it comes to producing the energy needed by growing human communities, all possibilities and alternatives needs to be adapted and redesigned in order to improve the atmospheric emissions level.
The energy sector needs to make major changes in the coming years for obtain encouraging results and this goal will be achieved if new technologies in the field of renewable energy production that are available and in unlimited quantities are developed and applied.
A solution to be applied is also the one proposed in this paper to achieve the endowment of buildings with wind turbines for energy harvesting in urban areas.
This mounting method can be accomplished for both new and old buildings and it should be noted that for new buildings it could become a task in the future, to ensure an energetic component of the building and to move to the level of energy independent building.
In addition, from the building architectural point of view, these facilities can be incorporated in the basic architecture of the building, thus achieving a combination and a harmonization of the aesthetic and functional aspect.

References

[1] Longo, R., P. Nicastro, M. Natalini, P. Schito, R. Mereu, and A. Parente. "Impact of urban environment on Savonius wind turbine performance: A numerical perspective." *Renewable Energy* 156 (2020): 407-422.
[2] Müller, G., M. F. Jentsch, and E. Stoddart. "Vertical axis resistance type wind turbines for use in buildings." *Renewable Energy* 34, no. 5 (2009): 1407-1412.
[3] Casini, M. "Small vertical axis wind turbines for energy efficiency of buildings." *Journal of Clean Energy Technologies* 4, no. 1 (2016): 56-65.
[4] Xu, W., Y. Li, G. Li, S. Li, C. Zhang, and F. Wang. "High-resolution numerical simulation of the performance of vertical axis wind turbines in urban area: Part II, array of vertical axis wind turbines between buildings." *Renewable Energy* (May 2021). Journal Pre-proof.
[5] Peacock, A. D., D. Jenkins, M. Ahadzi, A. Berry, and S. Turan. "Micro wind turbines in the UK domestic sector." *Energy and Buildings* 40, no. 7 (2008): 1324-1333.
[6] Ragheb, M. *Wind turbines in the urban environment*. MSc Thesis, 2008.
[7] Dilimulati, A., T. Stathopoulos, and M. Paraschivoiu. "Wind turbine designs for urban applications: A case study of shrouded diffuser casing for turbines." *Journal of Wind Engineering and Industrial Aerodynamics* 175 (2018): 179-192.
[8] Smith, R. F., and S. Killa. "Bahrain World Trade Center (BWTC): the first large-scale integration of wind turbines in a building." *The structural design of tall and special buildings* 16, no. 4 (2007): 429-439.
[9] Bobrova, D. "Building-integrated wind turbines in the aspect of architectural shaping." *Procedia engineering* 117 (2015): 404-410.
[10] Toja-Silva, F., T. Kono, C. Peralta, O. Lopez-Garcia, and J. Chen. "A review of computational fluid dynamics (CFD) simulations of the wind flow around buildings for urban wind energy exploitation." *Journal of Wind Engineering and Industrial Aerodynamics* 180 (2018): 66-87.
[11] Rezaeiha, A., H. Montazeri, and B. Blocken. "A framework for preliminary large-scale urban wind energy potential assessment: Roof-mounted wind turbines." *Energy Conversion and Management* 214 (2020): 112770.
[12] Zanforlin, S., and S. Letizia. "Effects of upstream buildings on the performance of a synergistic roof-and-diffuser augmentation system for cross flow wind turbines." *Journal of Wind Engineering and Industrial Aerodynamics* 184 (2019): 329-341.
[13] Grieser, B., Y. Sunak, and R. Madlener. "Economics of small wind turbines in urban settings: An empirical investigation for Germany." *Renewable Energy* 78 (2015): 334-350.
[14] Jafari, S. A. H., K. C. Kwok, and S. Hassanli. "Integration of wind turbines in tall buildings for wind power generation." Paper presented at the 8th International Colloquium on Bluff Body Aerodynamics and Applications, Boston, Massachusetts, USA, June 7 – 11, 2016.
[15] https://www.emsd.gov.hk_wind+turbines+on+buildings.
[16] https://th.bing.com/th/id/Re707c5_ImgRaw.
[17] www.wind-works.org_stream-12W-Rooftop_20120422=wind+turbines+on+buildings&simid.
[18] https://www.wsp.com/-/media/Project/Global/Image/img-engineering-strata-se1.

Analysis of Pneumatic Circuits with FluidSim

Dipl. Eng. **Remus COJOCARU[1],** Prof. PhD. Eng. **Paul BOCĂNETE[2],**
Assoc. Prof. PhD. Eng. **Dumitru DELEANU[2],** Dipl. Eng. **Cătălin FRĂȚILĂ[3],**
PhD. Eng. **Tiberiu AXINTE[3],** Dipl. Eng. **Mihai DIACONU[3]**

[1]Princess Cruises, USA

[2]Constanta Maritime University, Romania

[3]Research Center for Navy, Romania

*tibi_axinte@yahoo.com

Abstract: *In this paper, we study the pneumatic schemes with FluidSim software from Festo. The pneumatic circuits have the advantage that they do not pollute the air and have a low energy consumption. Therefore, pneumatic installations are used in various technical fields. The pneumatic installations must be adapted according to the purpose for which they are used. At the beginning, the pneumatic installation must be designed and after that, it can be mounted. The project of installations consists in drawing pneumatic schemes. In introduction, we present the role and the main fields in which the pneumatic installations are used. After that, we describe those basic pneumatic devices that constitute the pneumatic schemes. Based on pneumatic devices described, we will make some simple and complex pneumatic circuits.*

Keywords: *FluidSim, pneumatic, scheme, circuit, cylinder*

1. Introduction

The first inventions described in the field of pneumatics were made by the mathematician Hero (10-75 A.D.) from Alexandria. These inventions in the field of pneumatics are based on the power of wind and steam, [1].
But today all pneumatic devices work based on air pressure is achieved by an air compressor. In order for compressed air to reach from the compressor to the pneumatic devices, it must pass through air line hoses, [2].
In fact, all pneumatic systems generally consist of two parts: operative and control.
The operative part is made of all pneumatic devices. The control part has the role of providing pneumatic control signals to the pneumatic devices, Fig. 1.
Pneumatic installations are used in: education, research, car service, wagon repair workshop, locomotive depot, etc, [3].

Fig. 1. Pneumatic trainer kit type TP 101, [4]

2. Pneumatic devices

In recent years, much has been invested in the development of pneumatic devices, [5].
Thus, the latest generations of devices can operate at a lower In this paper, we present the main features for the following pneumatic devices: air distributor, double acting cylinder, air service unite.

- Compressed air supply

Designation	Range	Value	Unit	Symbol
Operating pressure	0..2	0.6	MPa	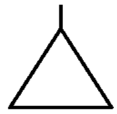
Volume	0.001...1000	0.1	l	
Max flow rate	0...5000	1000	l/min	

- Double acting cylinder

Designation	Range	Value	Unit	Symbol
Piston diameter	0.001...2	0.02	m	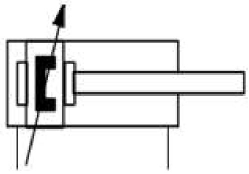
Piston rod diameter	0...1	0.008	m	
Maximum stroke	0.001...0.2	0.1	m	
Piston position	0..5	0	m	
Mounting angle	0...360	0	deg	

- Throttle check valve

Designation	Range	Value	Unit	Symbol
Standard nominal flow rate	0.1..5000	85	l/min	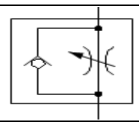
Opening level	0...100	100	%	

- Air service unite

Designation	Range	Value	Unit	Symbol
Standard nominal flow rate	0.1..5000	750	l/min	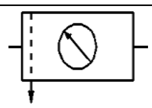
Nominal pressure	0...2	0.6	MPa	

- Distributor type 5/n way valve

Designation	Range	Value	Unit	Symbol
Standard nominal flow rate	0.1..5000	60	l/min	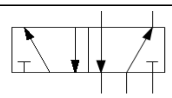
Desired position	0...4	2	-	

The advantage of pneumatic installations ist hat the devices can be replaced very easily. For example, double cylinder with cylinder without piston rod. Or types of distribuitors: a 5/n way valve with another a 6/n way directional valve. Change of the devices from the pneumatic installations is made according to the necessities. Usually the pneumatic devices change when: the part fails, there is another type of part, when the pneumatic installation is maintained, etc. Always after mounting the pneumatic device with the air line hoses through which the air passs, check for air leaks, [4].

3. Pneumatic schemes

In order to build a pneumatic installation, a pneumatic circuit must be realised first time. At present, the pneumatic schemes are designed with special software. For the project of pneumatic circuits, we use the FluidSim software. At the beginning, we will represent a simple pneumatic scheme, Fig.2.

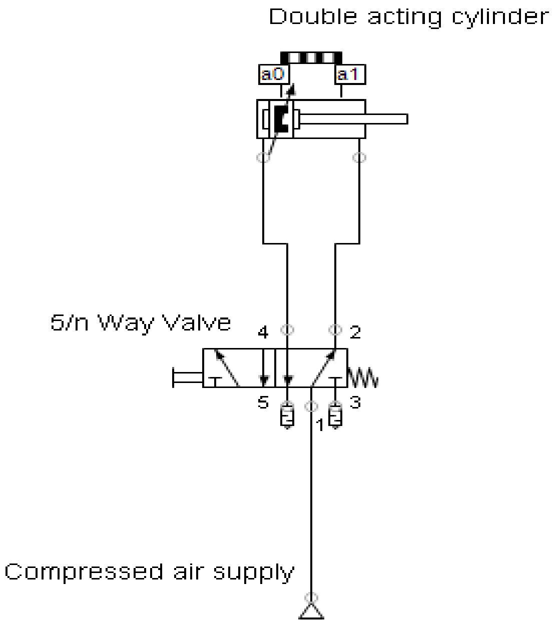

Fig. 2. Pneumatic schemes – Case 1

The first pneumatic circuit is composed of:
- A double acting cylinder.
- A distributor type 5/n way valve.
- A compressor.

For the pneumatic cylinder are three diagrams on the following parameters: position (x), velocity (v) and acceleration (a), Fig. 3.

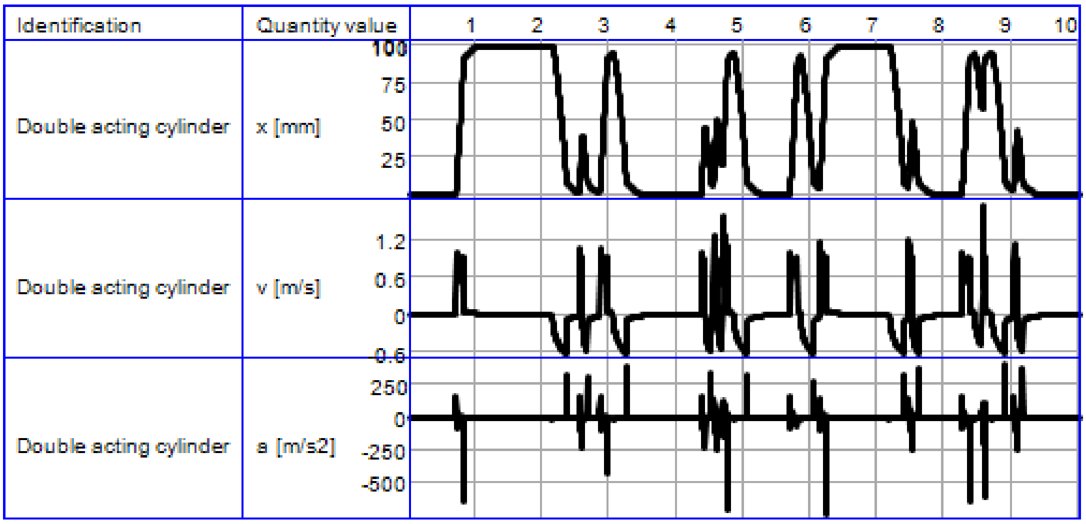

Fig. 3. Double acting cylinder diagrams – Case 1

The compressor supplies air with a maximum pressure of P_{max} = 0.6 MPa.

At the circuit in case 1, we mount a throttle check valve. The throttle check valve is used for controlling the operation speed from pneumatic cylinder, Fig.4.

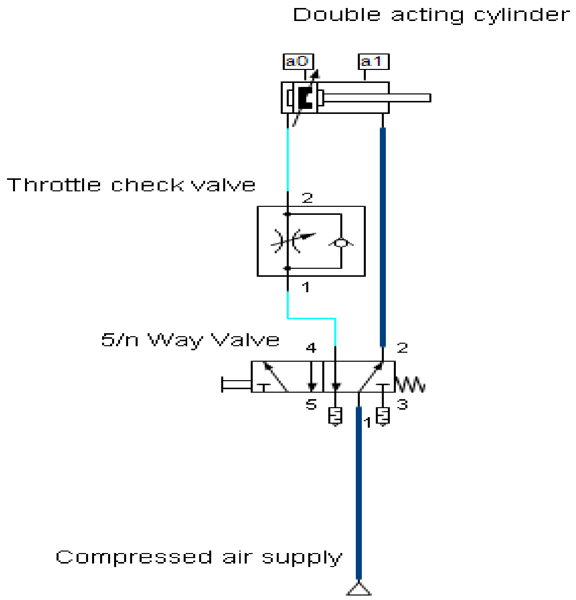

Fig. 4. Pneumatic schemes with throttle check valve – Case 1

Further, to this pneumatic circuit we add an air service unit and air filter, Fig. 5.
Air filter removes impurities present in compressed air before it is delivered to the pneumatic components, [6].

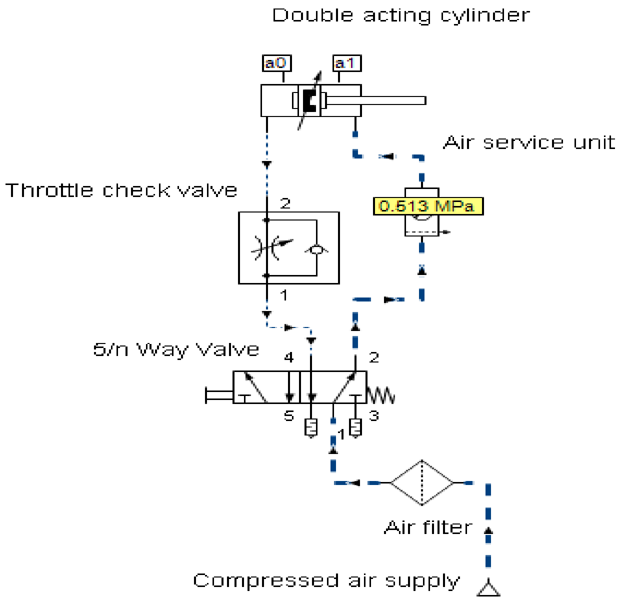

Fig. 5. Pneumatic schemes with air service unit and air filter – Case 1

Ordinarily air service unit is present after a compressor in a pneumatic circuit. The function of this device is to remove humidity, dust particles and moisture from the compressed air, [7].
The piston in the cylinder moves from a0 to a1. The pressure in the air service unit is P= 0.513 MPa, when we recorded the piston movement. When the piston reaches and in a1 then it moves in reverse, meaning from a1 to a0, Fig. 5.
The second pneumatic circuit scheme is made of following devices, Fig. 6:

- two double acting cilynder adjustable (cylinder I and II).
- two pressure gauges.
- Two distributors types 5/n way wave.
- three distribuitors types 3/n way wave
- a compressor.

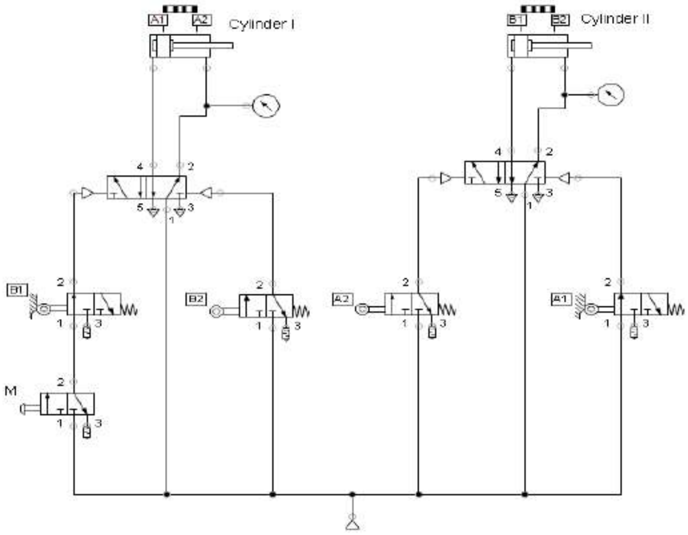

Fig. 6. Pneumatic schemes – Case 2

We perform a simulation of the pneumatic system from case 2. Press the M button to start the pneumatic circuit in case 2. At the beginning, the piston from cylinder I moves between point A1 and point A2. Afterwards, the piston from cylinder II between points B1 and B2. During the movement of the pistons, there are pressure variations in the pneumatic cylinders. In our case, the pressure in cylinder I is $P_I = 0.486$ MPa and pressure in cylinder II is $P_{II} = 0.6$ MPa, Fig.7.

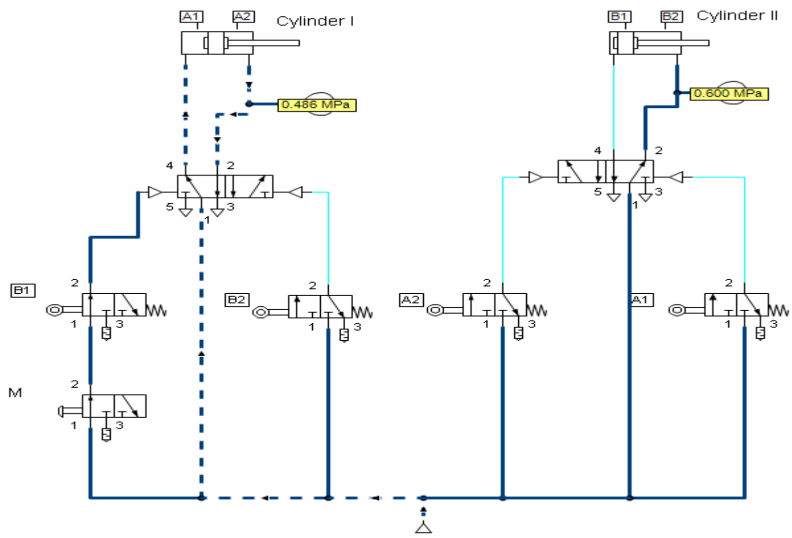

Fig. 7. Pneumatic circuit open – Case 2

After the piston from cylinder II reaches in point B2, then pistons return. First, the piston from cylinder II moves between point B2 and point B2 and then the cylinder I move from points A2 and A1, Fig. 7.

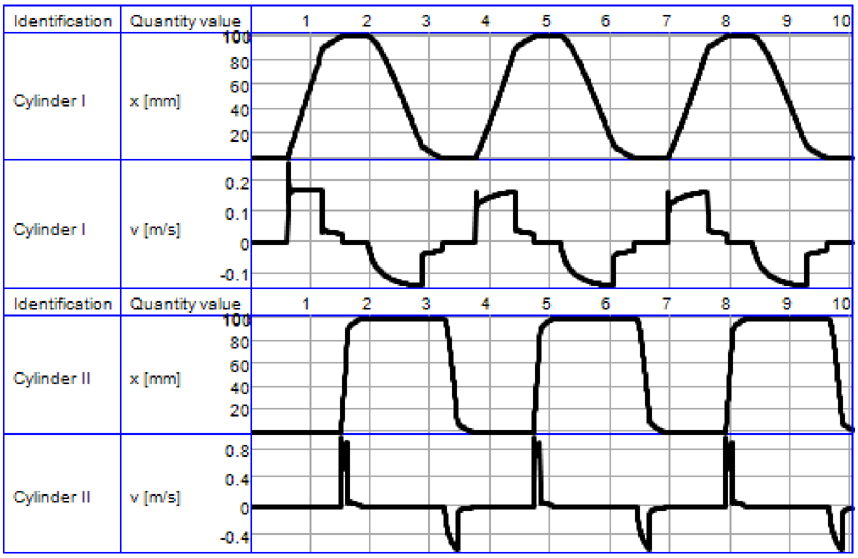

Fig. 8. Pneumatic cylinders diagrams - Case 2

Diagrams are made from both cylinders that have parameters: position(x) and velocity(v), Fig. 8.

4. Conclusions

The project of the pneumatic circuits with the FluidSim software is done in a short time. Pneumatic scheme can be modified depending on the field in which the pnumatic installation is used. After the pneumatic system is designed, a simulation of the circuit can be performed. If in this article, we have simulated pneumatic circuits with one or two cylinders. In the future we cab design pneumatic schemes with three or four pneumatic cylinders. Pneumatic installations can be made quickly and easily if the pneumatic circuits are amde with FluidSim from Festo. Devices that are defective or old, can be replaced with other high performance devices in pneumatic installations bassd on the projected circuits. Based on simple pneumatic circuits, complex pneumatic circuits can be developed. Thus, it is possible to build complex pneumatic installations with an optimal energy consumption

References

[1] Mistry, H. *Fundamentals of Pneumatic Engineering*. CreateSpace Independent Publishing Platform, 2013.
[2] Rus, S., M. Diaconu, F. Zaharia, M. Degeratu, and A. Ion. "Wind tunnel testing on underwater robots models." *Annals of the Oradea University, Fascicle of Management and Technological Engineering* IX (XIX) (2010): 2.39-2.47.
[3] Belev, B., P. Gechevski, and N. Dundov. "Using Simulators for Education and Training – Condition, Necessity." *Development* (2005): 39-44.
[4] www.festo.com.
[5] Panaitescu, M., G. B. Dumitrescu, and A. Scupi. "Sustainable pneumatic transport systems of cereals." Paper presented at the 2013 International Conference on Environment, Energy, Ecosystems and Development, Venice, Italy, September 28-30, 2013.
[6] Rus, S., M. Diaconu, C. Fratila, and M. Degeratu. "Hyperbaric oxigen therapy (HBOT) as a practice of the scientific hyperbaric medicine and engineering." *Annals of the Academy of Romanian Scientists, Series on Engineerng Sciences* 10 (2018): 55-70.
[7] Bocanete, P. *Steam Turbines. Construction and Exploitation / Turbine cu abur. Constructie și Exploatare*. Constanta, Dobrogea Publishing House, 1996.

Comparison of Rainfall Interpolation Methods for Obtaining Mean Annual Maximum Precipitation Isohyets in a High Elevation Zone in Mexico

Dra. **Maritza ARGANIS[1*],** M.I. **Margarita PRECIADO[2],** M.I. **Juan José BAÑOS[3]**, Dr. **Alejandro MENDOZA[4]**

[1] Universidad Nacional Autónoma de México. Instituto de Ingeniería, MArganisJ@iingen.unam.mx

[2] Instituto Mexicano de Tecnología del Agua, camifoxy@gmail.

[3] Universidad Nacional Autónoma de Mëxico. Posgrado en Administración. Facultad de Contaduría y Administración. juanbmartin@yahoo.com

[4] Universidad Nacional Autónoma de México. Instituto de Ingeniería, AMendozaR@iingen.unam.mx

*Corresponding Author: MArganisJ@iingen.unam.mx

Abstract: *Average rainfall calculation by isohyets method is considered in hydrology as one of the most accurate ones because traditionally this procedure takes into account site topography to draw lines of equal precipitation; also having isohyets in a region allows estimating mean precipitation at a point that does not have measurements. The spatial interpolation process consists of estimating values that a variable Z reaches in a set of points defined by a pair of coordinates (X, Y), known Z values of a set of points located in a study area. Almost all interpolation procedures are based, roughly, on the use of statistical techniques. To quality verification of an interpolated map, a validation set consisting of a series must be used of sampling points (of which the real value is therefore known) at which an estimate is to be made of said real value (without using of course the value measured in them). In this study, Inverse Distance Weighed (IDW) method and ordinary Kriging method (OK) with Gaussian variogram were applied in addition to Cokriging method (OCK) that uses a geographic information system in order to compare them from the density and shape of the isohyets obtained with these methods. For this, weather stations from CLICOM database belonging of Mexico City and the Valley of Mexico were considered. Additionally, design isohyets were obtained for 10 years return period to make comparisons with traditional isohyets existing in databases of an official agency. It was found that IDW method allows to draw closed isohyets of low precipitation compared to those obtained with Kriging, even though Kriging method in design events reports isohyets more parallel to traditional method ones; on the other hand and this method gave the best determination coefficient and lower mean square error, Cokriging method, which considers elevation as an additional variable, gave parallel shapes similar to those drawn historically. Therefore, it is considered that Kriging and Cokriging methods are valid for estimating design isohyets in the high elevated zone of Mexico analyzed.*

Keywords: *Isohyets, average maximum annual rainfall, Mexico City, Kriging, IDW, Cokriging*

1. Introduction

Average rainfall occurring in a basin is a fundamental concept of hydrology that is used in many practical problems, especially for rainfall transformation into runoff and subsequent obtainment of hydrographs that subsequently have to be simulated for a basin or river. The methods traditionally used for its estimation are the arithmetic method, Thiessen polygons and the Isohyets method [1,2],latter being most recommended because it considers study site topography and gives a better indication precipitation contribution at each site of the basin, considering watershed, although there are authors who have reported that depending on the study site, one method may be better than another [3].
Geographic information systems, which use has become widespread since 1980s, use various interpolation tools to plot surfaces and lines of equal value of a variable, this are used as aids for plotting contour lines and climatic variables such as isotherms and isohyets. Among these methods, it stands out the Kriging methods and the inverse of the weighted distance method (IDW) of which persists the discussion of whether the Kriging methods have advantage over the IDW method due to the fact that the first considers, not only space influence, but also of time in analyzed variable, while IDW method only highlights spatial aspect or data separation according to

site analysis [4], also authors report that Kriging method gives better values of equal-valued curves depending on climatic variable [5,6]. [6] found that precipitation interpolation at a site improves when taking into account variables addition of precipitation and distance, if elevation is contemplated as an additional variable; from their comparisons between interpolation methods, they reported as the best the ordinary Cokriging method applied on monthly precipitation data in a basin of Australia. In areas of the Gulf of Mexico, elevation variable does not show a high correlation with precipitation, according to the study by [7] and Cokriging method reports better results than Idw technique, but does not improve on thin plate smoothing spline (TPSS) techniques.
The previously cited studies indicate that one rainfall interpolation method may be better than another depending on the physiography of the analyzed site; for that reason, this study investigates which of these interpolation methods reports the best results in precipitation estimation with isohyets in a region of high elevations and subject to convective rainfall. For this purpose, a comparison of isohyet maps calculated with three ArcGis© tool is made: one of Ordinary Kriging methods (in this case one that uses a Gaussian semivariogram), IDW method, and also using Cokriging method that takes into account precipitation, distance and elevation of measurement points. Mean square error and determination coefficient are used as basis of comparison Additionally, a comparison of design isohyets obtained with these methods was made with respect to isohyets drawn "by hand" reported by databases of official agencies in Mexico [8], i.e., with traditional method for design isohyets for a return period Tr=10 years. The study area used was Mexico City, which has elevations up to 2250 meters above sea level, and some stations for Mexico State, in Mexican Republic, were also considered.

2. Methodology

2.1 Isohyets Method

P Isohyets are defined as curves of equal precipitation. This method makes it possible to obtain

Weighted average precipitation can be acquired in the following way [9] (Figure 1):
a) Isohyets are drawn from stations, considering high topography points.
b) Each isohyet is assigned an area equal to sum of half of areas between two contiguous isohyets, or each area between two isohyets is assigned an average value of precipitation Pi of the isohyets.
c) Area Ai of the surfaces is estimated, the total area A_t will be sum of these areas.
d) Mean value is calculated using the following expression (eq. 1):

$$P = \frac{1}{A_t}\sum_{i=1}^{n} P_i A_i \quad (1)$$

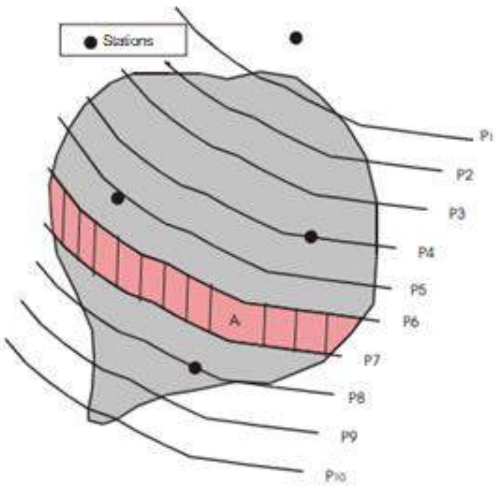

Fig. 1. Isohyets method. (Source: [9])

2.2 Inverse Distance Weighted Method (IDW)

The Inverse Distance Weighted Method (IDW) is used and described in ArcGis© or Arcmap of Esri©, it was presented in 80's by [10]. [11] performs interpolation of the value of a cell with the help of a weighted linear combination of sample points taken at a certain distance; by default, power of distance of the points to one of interest is set to 2 and the greater the distance of sample points to one of interest less participation it will have in estimation of its value. It is considered a deterministic method because it uses a mathematical equation and considers values measured in surroundings. [12]. Equation used by IDW method, to estimate precipitation P ̃(S_0) at a point S_0, known precipitation information P(Si) at n points S_i , with i=1,2,...,n , is as follows [6] (eq. 2):

$$\hat{P}(S_0) = \sum_{i=1}^{n} \omega_i P(S_i) \tag{2}$$

Where: $\omega_i = \frac{{d_{i0}}^{-k}}{\sum_{i=1}^{n} {d_{i0}}^{-k}}$, ω_i are the weight factors, d_{i0} Euclidean distance between points i with known information and point 0, k is a power given as a control parameter.

This method interpolates a raster surface from points using inverse distance weighting (IDW) technique. Main parameters considered by this method are described in [13, 14].

2.3 Variogram

Let Z be a variable that takes values at points i and j; if a new variable y is defined as difference (eq. 3):

$$y = z_i - z_j \tag{3}$$

Variogram of Z is variance of the prior y variable and is denoted (eq. 4):

$$\gamma_{ij} = E((z_i - z_j)^2) \tag{4}$$

Variogram depends only on separation of the two points i and j, but not on the location of these points [15].

2.4 Kriging Methods

Kriging methods [16, 17] are geostatistical interpolation methods and take into account the spatial correlation between the data, i.e. not only the distance of the sample data to the data to be estimated, but also the way in which the sample points are spatially positioned. two steps that Kriging methods follow are: obtaining statistical dependence rules with the help of creating variograms and covariance functions to calculate the statistical dependence values (called spatial autocorrelation) that depend on autocorrelation model (fitting a model) and in a second step performs unknown values prediction. [11].

There are two methods for Kriging: ordinary and universal [13].

Ordinary Kriging can use the following semivariogram models:
1) Spherical: spherical semivariogram model. This is the default.
2) Circular: circular semivariogram model.
3) Exponential: exponential semivariogram model.
4) Gaussian: normal or Gaussian distribution semivariogram model.
5) Linear: linear semivariogram model with a sill.

Universal Kriging can use the following semivariogram models:
1) Linear with linear derivative: universal Kriging with linear derivative.
2) Linear with quadratic derivative: Universal Kriging with quadratic derivative.

There are options available through the Advanced Parameters dialog box. These parameters are:

1) Lag size: default value is the cell size of output raster.
2) Major range: represents a distance beyond which there is little or no correlation.
3) Partial threshold: the difference between the nugget and the threshold.
4) Nugget: represents error and variation at spatial scales too fine to detect. The Nugget effect is seen as a discontinuity at the origin.

In this analysis, the lowest variances were obtained with the ordinary Kriging method and Gaussian semivariogram.

Estimating precipitation equation for ordinary Kriging method is, eq 5:

$$\widehat{P(s_0)} = \sum_{i=1}^{n} \omega^{ok}{}_i \, P(S_i) \tag{5}$$

Where: $\sum_{i=1}^{n} \omega^{ok}{}_i = 1$, $\omega^{ok}{}_i$ are the weight factors of the ordinary Kriging method that are estimated by solving a system of n+1 linear equations (eqs. 6 and 7):

$$\sum_{i=1}^{n} \gamma(s_i - s_j)\omega_i^{ok} + \mu_1^{ok} = \gamma(s_i - s_0) \tag{6}$$

$$\sum_{i=1}^{n} \omega^{ok}{}_i = 1 \tag{7}$$

Where γ (s_i − s_j) are the variogram values between sampling locations, s_i and sj, γ (s_j − s_0) are variogram values between sampling location sj and target location, and s_0, is Lagrange multiplier parameter. Experimental variogram using Ordinary Kriging method can be found in [6]; in hydrology it is common to use defined positive exponential variogram, Gaussian and spherical type to model experimental variogram (Table 1).

Table 1: Examples of positive definite variograms used in Ordinary Kriging method (Source: [6])

Variograms model	Equation
Exponential	$\gamma(d) = C_0 + C_1[1 - e^{(-\frac{2d}{a})}]$
Gaussian	$\gamma(d) = C_0 + C_1[1 - e^{\left(-\frac{2d^2}{a^2}\right)}]$
Spherical	$\gamma(d) = \begin{cases} C_0 + C_1\left[\frac{2}{3}\left(\frac{d}{a}\right) - \frac{1}{2}\left(\frac{d^3}{a^3}\right)\right], d < a \\ C_0 + C_1, d \geq a \end{cases}$

C_0 = Nugget coefficient, C_0 + C_1 = S_{ill}, a = variogram model range. d = separation distance between two locations

2.5 Cokriging Method

Cokriging method proposes to improve Ordinary Kriging method by considering a second variable to improve estimation of search variable; for case of precipitation estimating at a point, as a precipitation function at other sites, the distance between them and elevation as a second variable, equations of method are by next form (eq. 8):

$$\widehat{P(s_0)} = \sum_{i1=1}^{n} \omega^{ock}{}_{i1} \, P(S_{i1}) + \sum_{i2=1}^{n} \omega^{ock}{}_{i2} \, E(S_{i2}) \tag{8}$$

Where: $\sum_{i1=1}^{n} \omega^{ok}{}_{i1} = 1, \sum_{i2=1}^{n} \omega^{ok}{}_{i2} = 0$, $\omega^{ok}{}_{i1}$ are the weight factors associated with first variable P (precipitation in this study) and $\omega^{ok}{}_{i2}$ are weight factors associated with second variable E (elevation in this analysis). Such factors are obtained by solving a system of n+2 simultaneous equations [6] (eqs. 9):

$$\sum_{i1}^{n}\gamma_{PP}(S_{i1}-S_{j1})\omega_{i1}^{ock}+\sum_{i1}^{n}\gamma_{PE}(S_{i2}-S_{j1})\omega_{i2}^{ock}+\mu_{1}^{ock}=\gamma_{PP}(S_{i1}-S_{0})\ for\ j1=1,\dots,n$$
$$\sum_{i1}^{n}\gamma_{EP}(S_{i1}-S_{j2})\omega_{i1}^{ock}+\sum_{i2}^{m}\gamma_{EE}(S_{i2}-S_{j2})\omega_{i2}^{ock}+\mu_{2}^{ock}=\gamma_{EP}(S_{i2}-S_{0})\ for\ j2=1,\dots,m$$
$$\sum_{i1=1}^{n}{\omega^{ock}}_{i1}=1\ \sum_{i2=1}^{m}{\omega^{ock}}_{i2}=0 \tag{9}$$

Where: $\gamma_{PE}(S_{i2}-S_{j1})$ and $\gamma_{EP}(S_{i1}-S_{j2})$ are the values of variograms crossed between the values of variables P and y E; μ_{1}^{ock} and μ_{2}^{ock} are Lagrange multipliers that take into account two unbiased conditions. The key in this method is to establish a model that establishes continuity and cross-dependence. Further details of this theory are explained by [6].

2.6 Characteristics of errors in interpolation

Error estimation in a point is difference between t-measured value and estimated one. Likewise assigning and error to each point.
Errors set must have the following characteristics:
1. Errors means and errors square must be near zero
2. Errors values must be independent of their location on space and not be autocorrelated.
3. Errors distribution function must be approximated to a normal distribution.

2.7 Study site

A portion of Mexico comprised by Mexico City was considered for analysis; from CLICOM database [18], climatological stations were selected for mean annual maximum precipitation data from 40 revised stations in Mexico City (with 20 or more years of record, some stations with data from 1921 to 2018), from the regionalization study of [2] . (Figure 2).

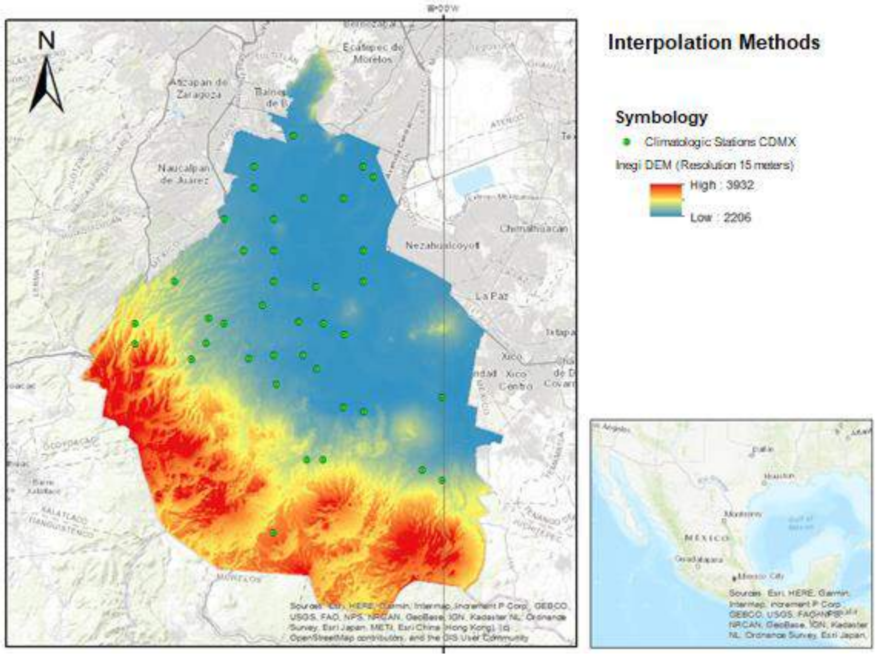

Fig. 2. CLICOM climatological stations in Mexico City. (Source: own design)

The digital elevation model (DEM) provided by INEGI, with a cell size of 15 m, was used. We had .shp files of the points of climatological stations, DEM and CDMX polygon.

3. Results and discussion

Spatial Analysis tool of ArcGis was used to apply different interpolation methods that this application has: a) IDW method b) Ordinary Kriging method (OK) and free tool compatible with ArcGis was added for the case of the c) CoKriging method. In each case, default parameters provided by Arcmap were used.
Figure 3 shows the isohyet map obtained with IDW method considering all climatological stations and Figure 4 shows isohyet map drawn by eliminating three stations with locations at high, intermediate and low elevations in the Mexico City basin, to see the sensitivity in the plotting of the isohyets by each method, three stations that were eliminated have elevations of 2229, 2260 and 2850 masl. Figures 5 and 6 show similar maps obtained with Ordinary Kriging method and Gaussian semivariogram with same considerations of using all stations and removing three stations mentioned above.

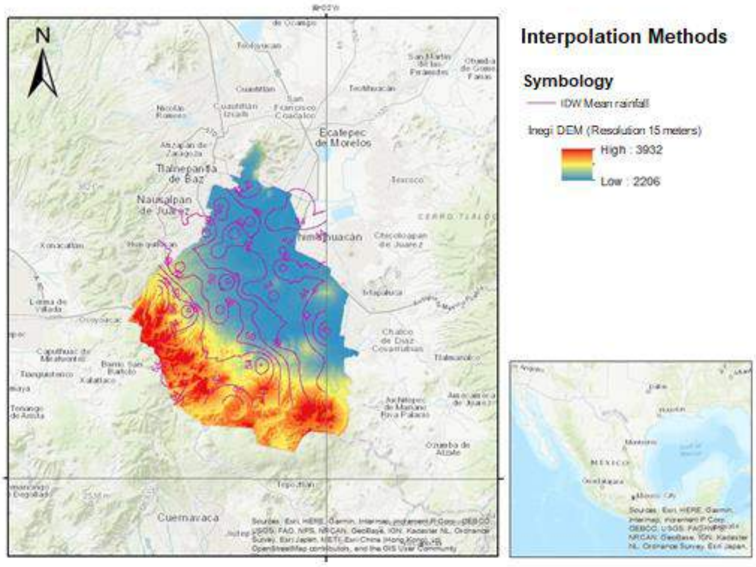

Fig. 3. Historical maximum annual mean rainfall isohyets map of Mexico City. IDW method using the stations. (Source: own design)

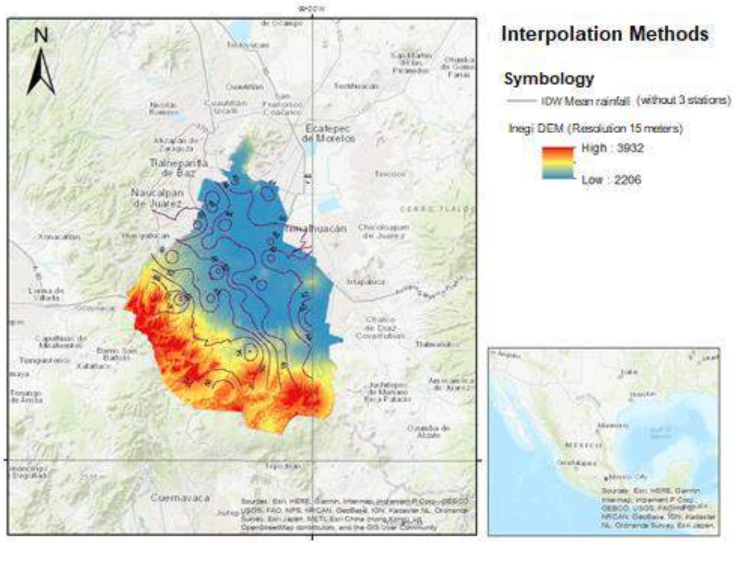

Fig. 4. Maximum annual mean rainfall isohyets map for Mexico City. IDW method and removing 3 stations. (Source: own design)

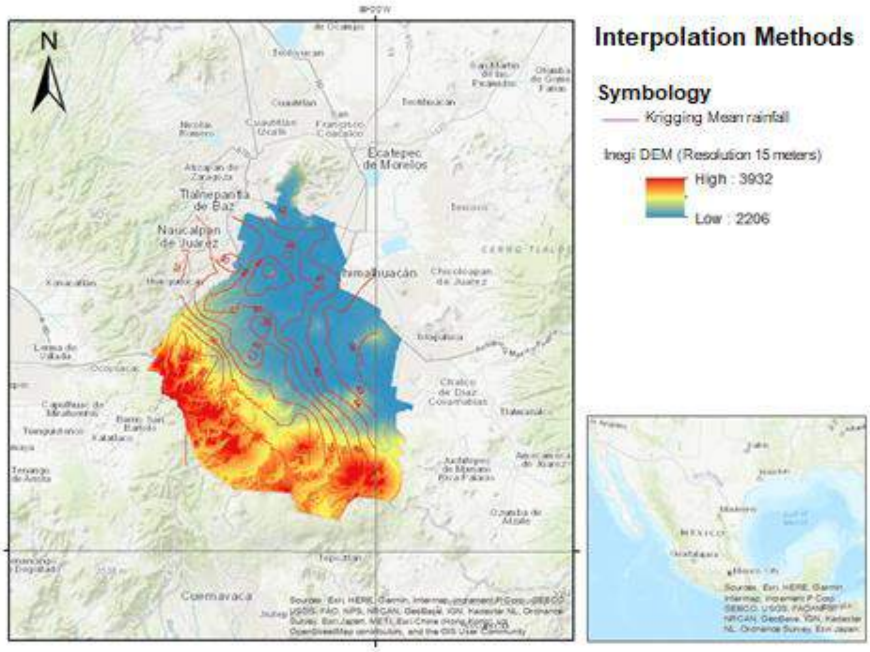

Fig. 5. Maximum annual mean rainfall isohyets map for Mexico City. Kriging Gaussian method and all stations. (Source: own design)

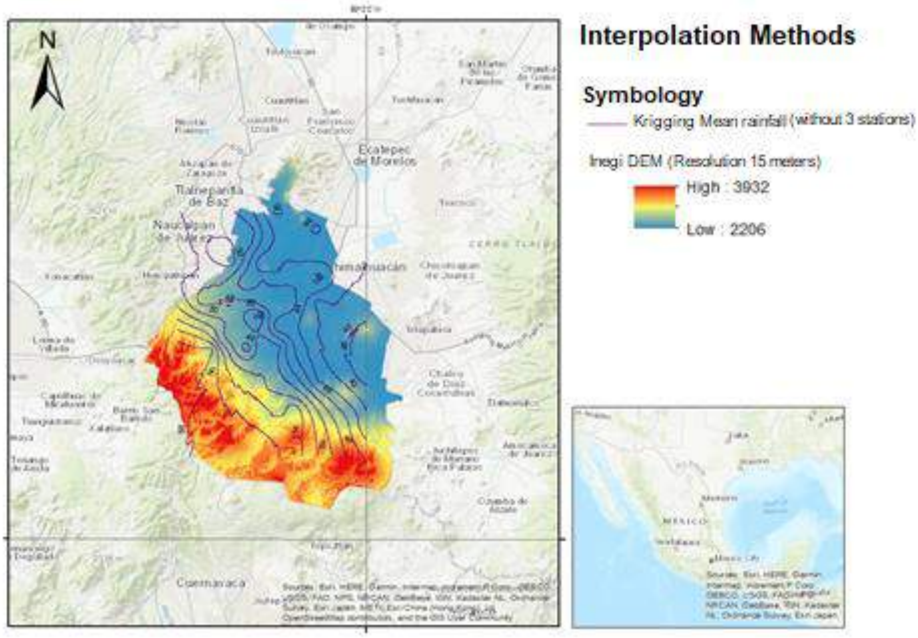

Fig. 6. Historical maximum annual mean rainfall isohyets map of Mexico City. Gaussian Kriging method and removing 3 stations. (Source: own design)

From figures 4 to 6 it can be noticed that Gaussian Kriging method has greater difficulty in obtaining closed isohyets, while IDW method does manage to represent closed precipitation isohyets of more than 70 mm. On the other hand, traces of the SCT curves, particularly those that do not manage to close, are a little more similar to those of the Kriging method.

Using design factors, considering a General Extreme Values function and regionalization methodology by [2] (Table 2) and with mean of maximum annual historical precipitation, the design isohyets were calculated for a return period of 10 years, using IDW method and Gaussian Kriging Method. Figures 7 and 8.

Table 2: Mexico City regional factors. General Extreme Value Function

Tr years	Factor
2	0.94326
5	1.2053
10	1.3868
20	1.567
50	1.8095
100	1.9984
500	2.4597
1000	2.6691
5000	3.1824
10000	3.4158

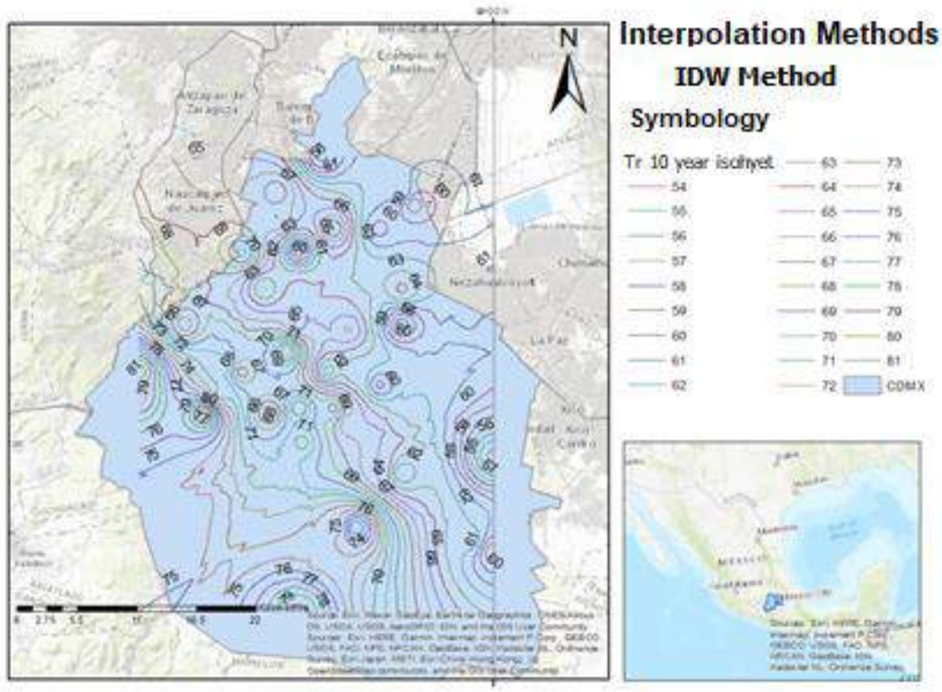

Fig. 7. Maximum annual mean rainfall isohyets map for Tr=10 years for Mexico City. IDW method. (Source: Own design)

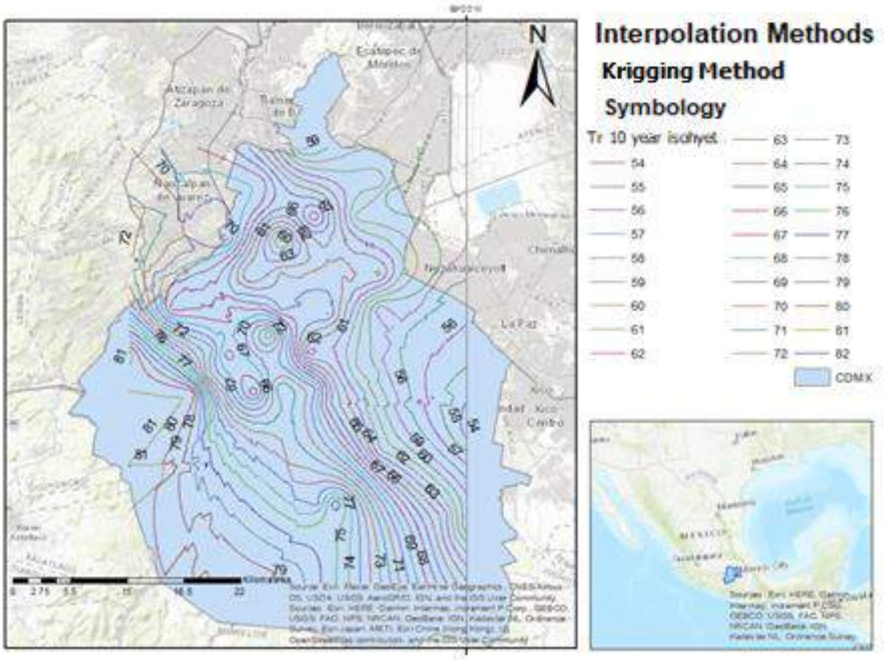

Fig. 8. Maximum annual mean rainfall isohyets map for a Tr=10 years for Mexico City. Gaussian Kriging method (Source: Own design)

Helped with the ArcGIS software, measured and calculated values with the Kriging and IDW methods were obtained. Measured data graphs against those calculated with these methods are shown in Figure 13 a and b.

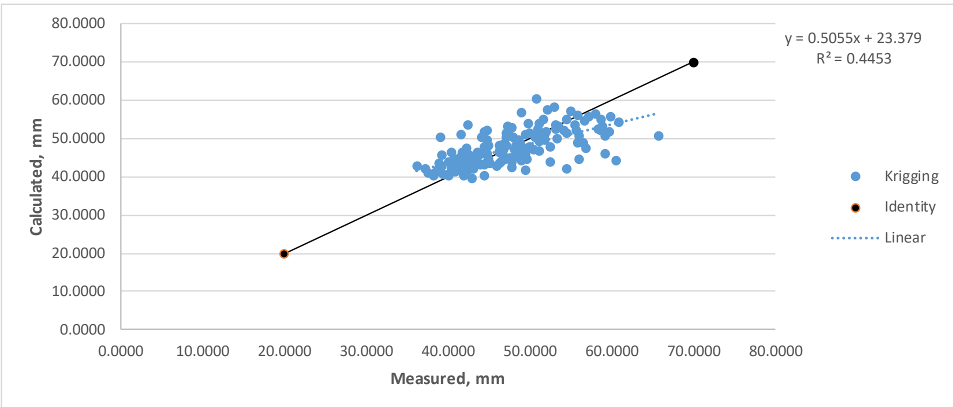

a) Krigging

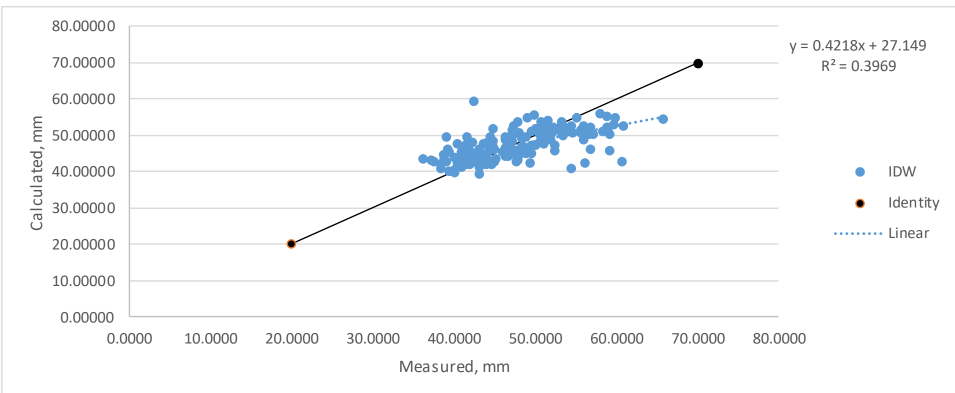

b) IDW

Fig. 13. Comparison of the measured and calculated values with the methods a) Kriging and b) IDW

The mean square error obtained with the Kriging method was 21.19 while with the IDW method it was 22.83, that is, Kriging gave a lower error in the estimation of the isohyets. From Figures 13 a and b, a determination coefficient R2 of 0.4453 and 0.3969 was estimated with Kriging and IDW, which implies a correlation coefficient of 0.67 and 0.63, so that the Kriging method resulted in a better fit.
Additionally, the descriptive statistics of the errors obtained with the Kriging and IDW methods as well as their histograms were performed (Table 3 and Figures 14 and 15).

Table 3: Descriptive statistics results. Kriging and IDW methods

Concept	Kriging	IDW
Mean	0.0593	0.2567
Typical error	0.3673	0.3807
Median	-0.4365	-0.1418
Mode	none	none
Standard deviation	4.6174	4.7858
Variance	21.3208	22.9043
Curtosis	1.4628	1.8356
Skewness	0.6680	0.4633
Range	27.6204	34.6957
Minimum	-11.3389	-16.8333
Maximum	16.2815	17.8624
Sum	9.3631	40.5624
Data number	158.0000	158.0000
Confidence level (95.0%)	0.7256	0.7520

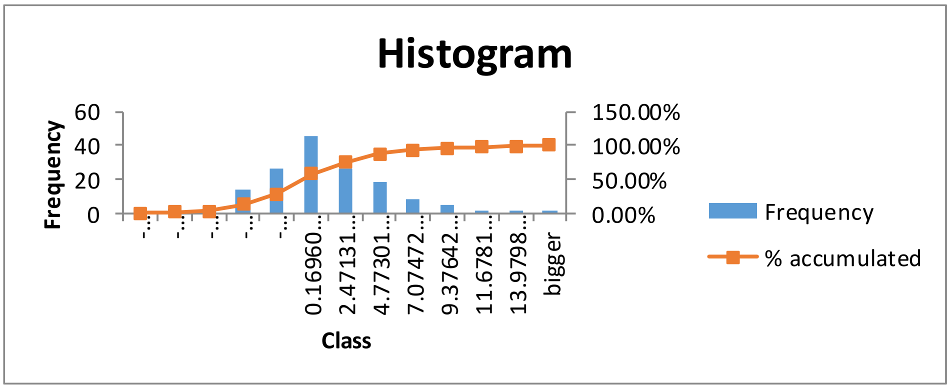

Fig. 14. Histogram of errors. Kriging method

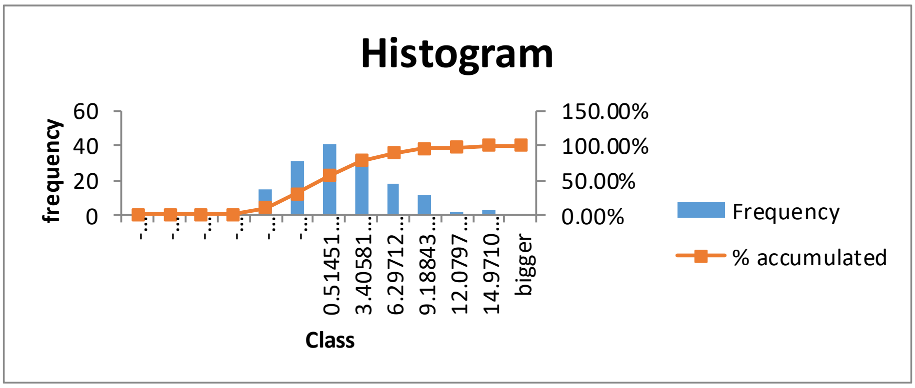

Fig. 15. Histogram of errors. IDW method

Regarding error statistics and their histograms, from figures 14 and 15 is observed that the errors have a grouping similar to those of a normal distribution, in addition from Table 3 the mean of the errors in the case of the Kriging method is close to zero and the standard deviation of the Kriging method error is less than the IDW method error.
To deepen into what happens with isohyets in case of design storms, we selected an isohyets map prepared "hand made" from the [8], corresponding to design isohyets for a Tr=10 years for maximum 24-hour rainfall in mm, which has closed isohyets and data similar to those of historical rainfall, for Mexico City case (Figure 16) and was superimposed with a transparency with respect to what is reported by IDW method and Gaussian Ordinary Kriging method in Figures 17 and 18.

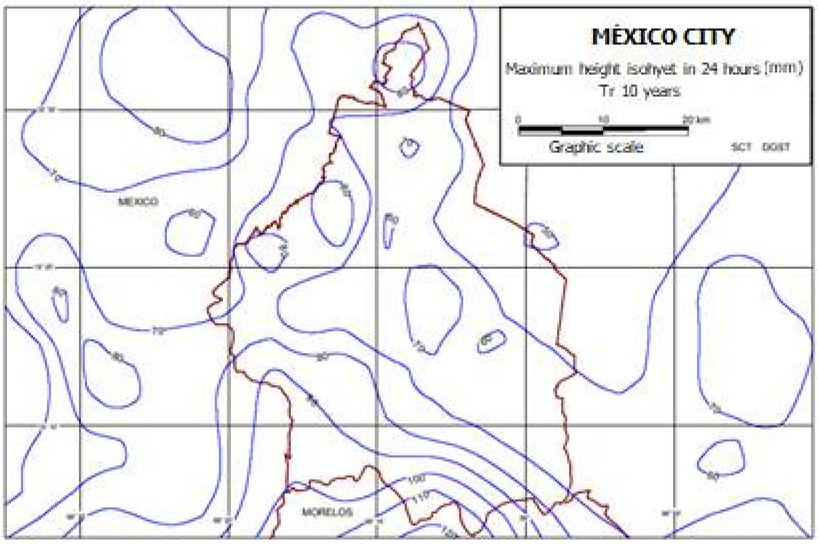

Fig. 16. Maximum annual mean rainfall isohyets map for a Tr=10 years for Mexico City. (Source:[8])

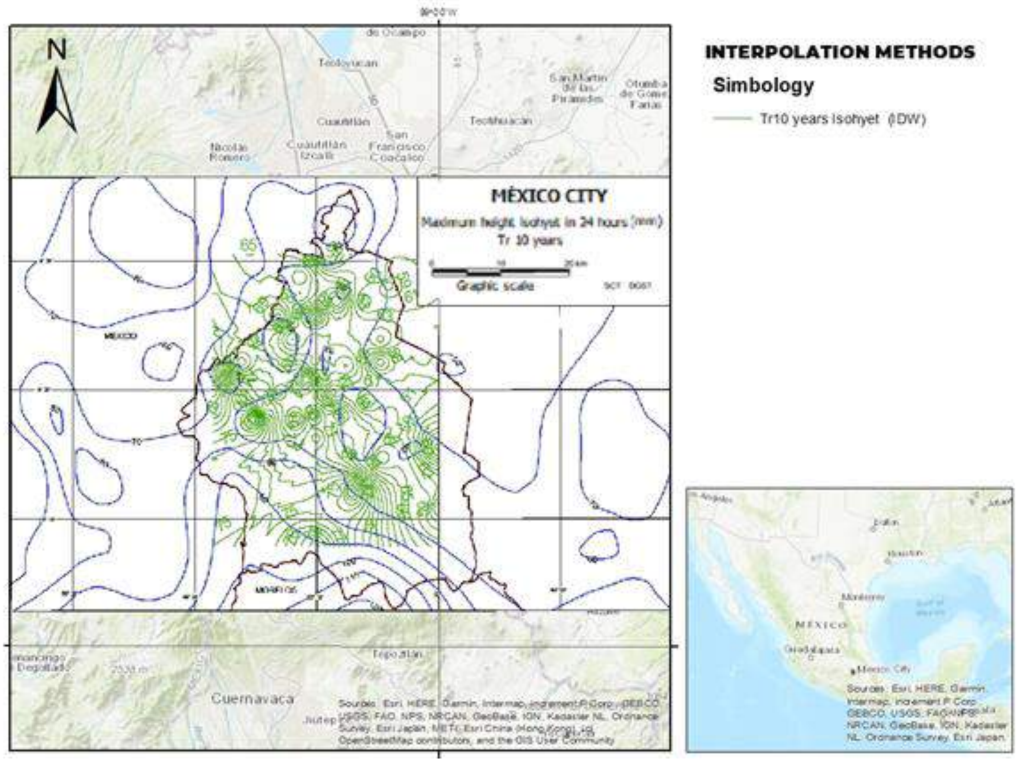

Fig. 17. Maximum mean annual rainfall isohyets map for Tr=10 years. Mexico City. IDW method. (Source: Own design)

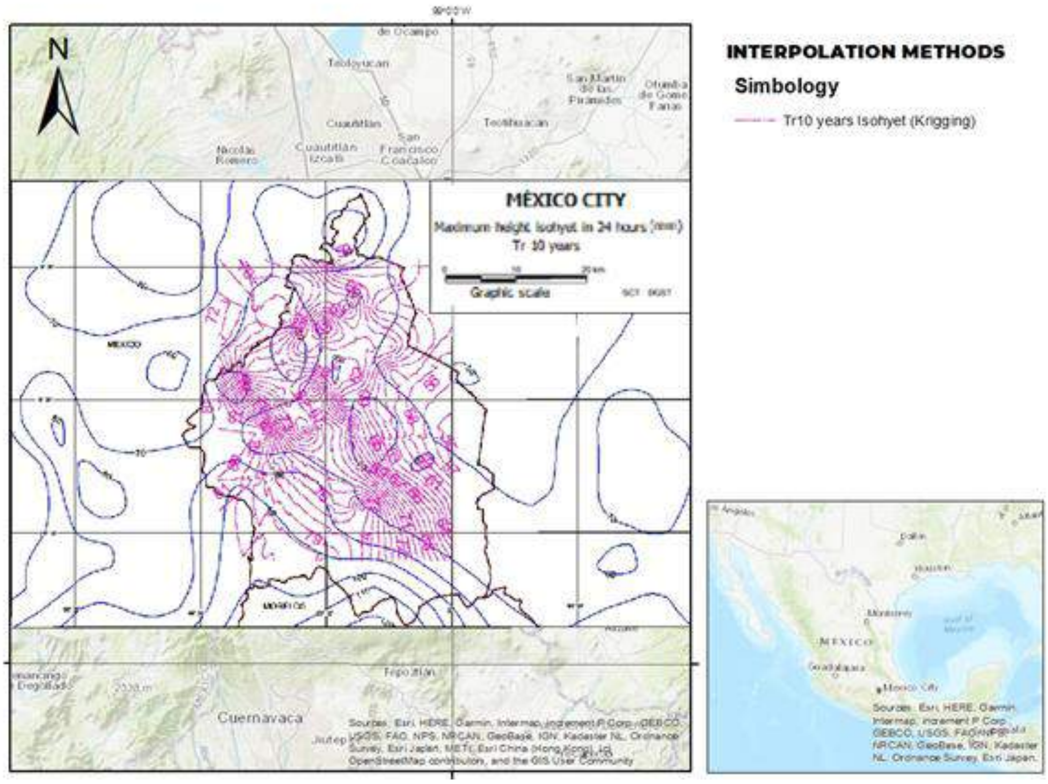

Fig. 18. Maximum mean annual rainfall isohyets map for Tr=10 years. Mexico City. Gaussian Kriging method. (Source: Own design)

Figures 17 and 18 show that Gaussian Kriging method has greater difficulty in obtaining closed contour lines; while IDW method does manage to represent closed precipitation isohyets of more than 60 mm; on the other hand, the traces of the SCT curves, particularly those that fail to close, are parallel to those of Kriging method in some of the 80 and 90 mm isohyets of the SCT.
In order to see effect of adding elevation variable in design isohyets estimation, Cokriging method was used and a new comparison was made with respect to the SCT isohyets for return period Tr=10 years (Figure 19).

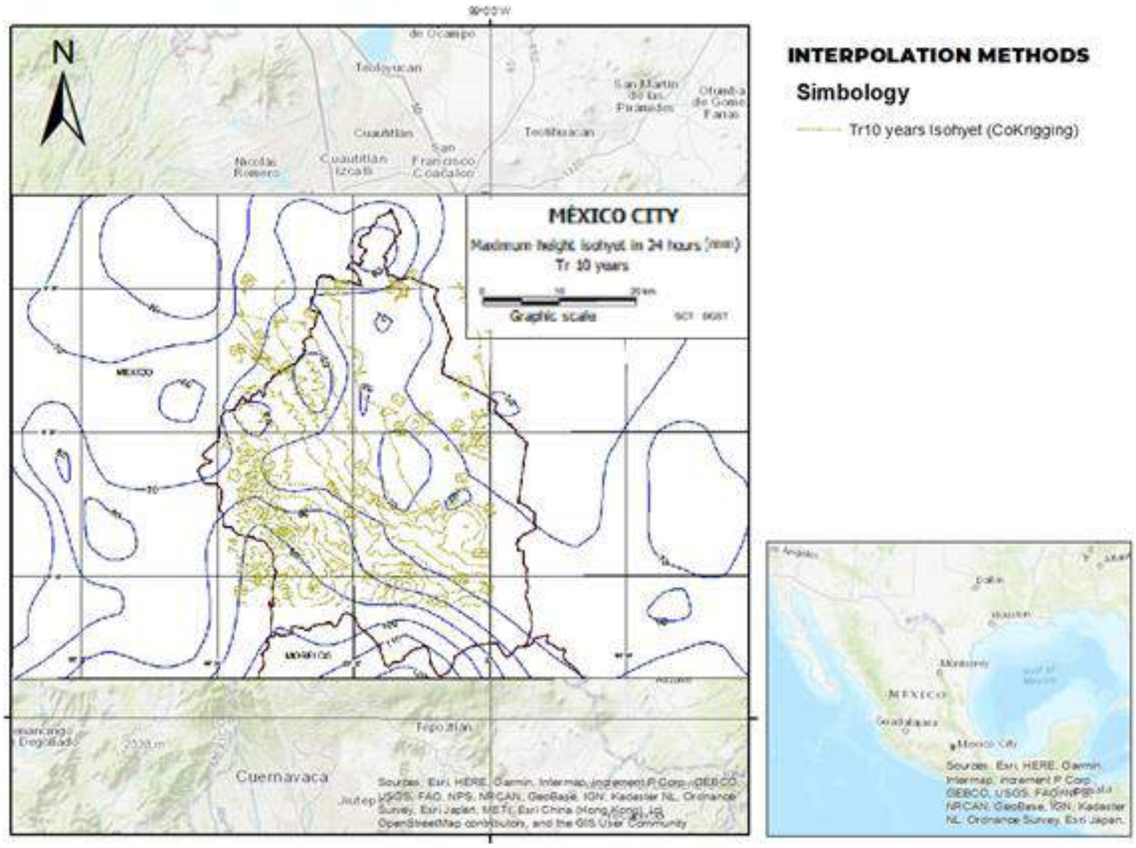

Fig. 19. Maximum mean annual rainfall isohyets map for Tr=10 years. Mexico City. Cokriging method. (Source: Own design)

Figure 19 shows that isohyets density decreases when using Cokriging method, with respect to Ordinary Kriging and IDW, closed isohyets are obtained and those that are open are more parallel to the SCT isohyets.

4. Conclusions

Applying different interpolation methods as a tool for drawing isohyets in a region with high elevations and their comparison with the traditional isohyet method in the case of historical and design events leads to the conclusion that the IDW method achieves a plotting of isohyets with regular geometric shapes and closures in them, but it has the disadvantage of only taking into consideration the precipitation variable and not the geography of the site and it provided a higher mean square error compared to the Kriging method.
Cokriging method, which takes into account both the precipitation variable and elevation as a secondary variable, gave isohyets that were parallel to those of traditional method provided by the official SCT, but the density of these isohyets was low in comparison to the results provided by the Kriging method. Additionally, the Kriging method obtained a higher correlation coefficient between the historical and calculated data, in addition to the fact that the mean square error was also lower with respect to the IDW method. The standard deviation of the error series was also lower when using the Kriging method; it is a simpler model than Cokriging and reports acceptable results that makes it a valid method to use for the estimation of for both historical and design isohyets in Mexico City, which is a site located at high elevations and characterized by convective rains, which in some cases are of high intensity, but short duration.

Acknowledgments

Authors would like to thank the student Juan Emmanuel Baños for reviewing texts of this document.

References

[1] Araujo, F. C., E. L. D. Mello, G. M. Gollin, L. E. D. Quadros, and B. M. Gomes. “Streamflow regionalization in Piquiri river basin”. *Engenharia Agrícola* 38, no.1 (Jan-Feb 2018): 22-31.
[2] Domínguez, M.R., E.E. Carrizosa, M.G.E. Fuentes, J.M.L. Arganis, R. J. Osnaya, and T.A.E. Galván. “Análisis regional para la estimación de precipitaciones de diseño en la República Mexicana”. “Regional Analysis in approaching design rainfall in Mexican Republic.” *Tecnol. Cienc. . Agua.* 9, no.1 (Jan-Feb 2018): 5-29. DOI: 10.24850/j-tyca-2018-01-01.
[3] Pizarro, T. R., C. Ramirez, and J.P. Flores. “Análisis comparativo de cinco métodos para la estimación de precipitaciones areales anuales en períodos extremos.” / “Comparative analysis of five methods for estimating annual areal precipitation in extreme periods.” *Bosque* 24, no. 3 (Dec. 2003): 31-38. http://dx.doi.org/10.4067/S0717-92002003000300003.
[4] Wruck, S., W. Klaus, H. G. Cortés Torres, W. Uhland, and E. K. Helene. “Desarrollo de un mapa de isoyetas (precipitación media anual) para el sureste de la región Costa de Chiapas.”/ “Development of an isoyeta map (average annual precipitation) for the southeast of the Costa de Chiapas region.” Memorias congreso OMMAC, 2014, Tuxtla Gutiérrez Chiapas, México, November 10-14.2014. http://www.ommac.org/memoria2014/extensos/E2014092604.pdf.
[5] López, M. J., J. Sánchez, and R. Andressen. “Comparación de varios métodos para la representación cartográfica de información climática en zonas altas del Estado Lara” / ”Comparison of various methods for mapping climate information in high areas of Lara State”. *Bioagro* 13, (2001): 39-46. https://www.redalyc.org/pdf/857/85713106.pdf.
[6] Adhikary, S., N. Muttil, and A. Yilmaz. “Cokriging for Enhanced Spatial Interpolation of Rainfall in Two Australian Catchments”. *Hydrol. Process*. 31 (2017): 2143-2161. https://doi.org/10.1002/hyp.11163.
[7] Díaz Padilla, G., I. Sánchez Cohen, R. Quiroz, J. Garatuza Payán, C. Watts Thorp, and I. R. Cruz Medina. “Interpolación espacial de la precipitación pluvial en la zona de barlovento y sotavento del Golfo de México”. / “Spatial interpolation of rainfall in the windward and leeward area of the Gulf of Mexico”. *Agricultura técnica en México* 34, no. 3 (Jul-Sept. 2008): 279-287. http://www.scielo.org.mx/scielo.php?script=sci_arttext&pid=S0568-25172008000300002&lng=es&tlng=es.
[8] SCT, 2021. Isoyetas / Isohyets. http://www.sct.gob.mx/fileadmin/DireccionesGrales/DGST/Isoyetas/distrito_federal.pdf.
[9] ETSECCP, 2021. Capítulo de Libro *La Precipitación*. / Book Chapter *Precipitation*. Escuela Superior de Ingeniería de Caminos Canales y Puertos, La Coruña. España. http://caminos.udc.es/info/asignaturas/grado_itop/415/pdfs/Capitulo%202.pdf.
[10] Philip, G. M., and D.F. Watson. “A Precise Method for Determining Contoured Surfaces”. *Australian Petroleum Exploration Association J.* 22 (1982): 205–212. https://doi.org/10.1071/AJ81016.
[11] Watson, D.F., and G.M. Philip. “A Refinement of Inverse Distance Weighted Interpolation.’ *Geoprocessing* 2 (1985): 315–327.
[12] Esri, 2020. Available on: https://www.esri.com/en-us/home.
[13] Arcgis, 2020. https://desktop.arcgis.com/es/arcmap/10.3/guide-books/extensions/geostatistical-analyst/an-introduction-to-interpolation-methods.htm.
[14] Arcgis, 2021. Ayudas. https://desktop.arcgis.com/es/arcmap/10.3/tools/3d-analyst-toolbox/comparing-interpolation-methods.htm.
[15] Ahmed, S., R. Jayakumar, and A. Salih. *Groundwater Dynamics in Hard Rock Aquifers Sustainable Management and Optimal Monitoring Network Design*. First edition, New York, Editors: Ahmed, S., Jayakumar, R., Salih, A. (Eds.), 2008. file:///C:/Users/marganisj/Downloads/2008_Book_GroundwaterDynamicsInHardRockA.pdf.
[16] Royle, A.G., F. L. Clausen, and P. Frederiksen. “Practical Universal Kriging and Automatic Contouring”. *Geoprocessing* 1 (1981): 377–394.
[17] Oliver, M. A. ”Kriging: A Method of Interpolation for Geographical Information Systems”. *International J. of Geographic Inf Syst*. 4 (1990): 313–332. https://doi.org/10.1080/02693799008941549.
[18] CICESE, 2021. Clicom. http://clicom-mex.cicese.mx/.

Acoustic Monitoring of Diesel Engine

Dr. **S. NARAYAN**[1*], Dr. **Vipul GUPTA**[2]

[1] Qassim University, Saudi Arabia

[2] Inus University, India

* Corresponding author's e-mail address: rarekv@gmail.com

Abstract: *The sound generated from a diesel engine can be modelled by suitable time-frequency analysis techniques. These methods show that there is a widening of frequency bands around top dead centre positions. As anticipated, the sound emitted from engine increases with an increase in speed and load. Condition monitoring of engines by Winger Ville functions and complex wavelet transformations allow studying the recognition of combustion events. This work deals with the tests carried out on a common rail direct diesel engine test rig. The acquired data was processed by signal processing techniques and results obtained are analyzed.*

Keywords: *Noise, vibrations, acoustic*

1. Introduction

Condition monitoring in diesel engine is accomplished by several means e.g., acoustics, wear, speed & cylinder pressure measurements. However, acoustic measurements provide a non-intrusive information about the signals originating from the engine. Acoustic monitoring of diesel engines has provided rich haul of information based on vibration measurements [1]. Acoustic contamination is perceived to be a problem for signal processing of diesel engine acoustics. Acoustic measurements can be carried by means of microphones placed at a distance that eliminates the need of high temperature resistant monitoring equipment. Initial step in acoustic monitoring is to consider factors like load, speed. Injection parameters etc. Austen and Priede have considered these factors in their work [2]. Yuichi and Yashiro have considered frequency components of noise radiated from camshaft and crankshafts [3].

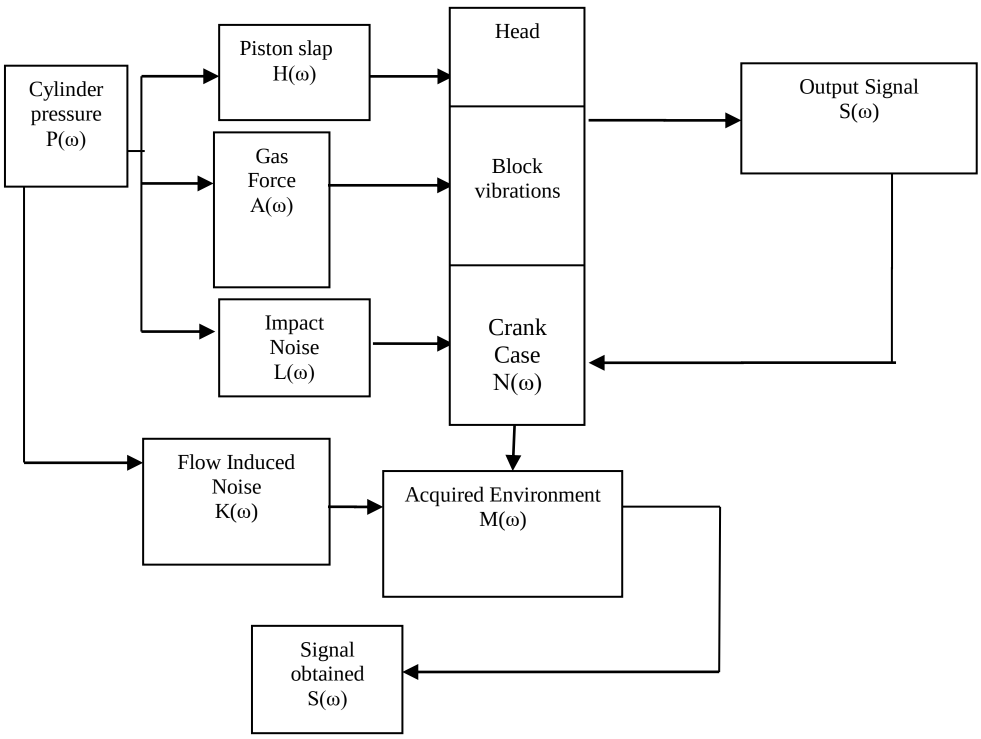

Fig. 1. Flow Chart of Engine Noise

Apart from these motion-based noise, combustion-based noise has been studied extensively [4]. Combustion based noise is affected by misfires, pressure rise rate, injection angles and amount of fuel injected. Li et al has used advanced signal processing techniques to detect injection faults, misfires etc. [5]. Gu and Ball have used fuzzy logic techniques to monitor noise spectra for condition monitoring of engines [6].
Several research works have been done to reduce the noise radiated from engines. Combustion noise is most important noise, which induces other kinds of noises like piston slap, bearing noise etc.
The overall noise emissions can be summarized as given in the figure 1 presented herein [7-20].

The sound signal in frequency domain can be expressed as:

$$S(\omega) = P(\omega)\,K(\omega)\,M(\omega)+[\,H(\omega)\,A(\omega)\,L(\omega)]\,P(\omega)\,N(\omega)\,M(\omega) \quad [1]$$

$$S(\omega) = \{[K(\omega) +[\,H(\omega)\,A(\omega)\,L(\omega)]\;\;N(\omega)\,\}\,P(\omega)\,M(\omega) \quad [2]$$

Which further yields

$$S(\omega) = J(\omega)P(\omega)\,M(\omega) \quad [3]$$

If we neglect the resonance phenomenon and take into consideration only combustion excitation this relationship can be written in time domain as:

$$S(t) = J(t)*P(t)*\,M(t) \quad [4]$$

All the types of noises except flow noise depend upon the combustion excitation force, which is dominant near TDC, hence sound emitted from the engine can be considered to vary linearly with combustion pressure in form of:

$$S(\theta) =k\,p(\theta) \quad [5]$$

Hence, it can be referred that combustion process is the key source of noise in engines. Figure 2 shows the plot of wave forms of in cylinder pressure for a complete revolution of 720° crank angle.

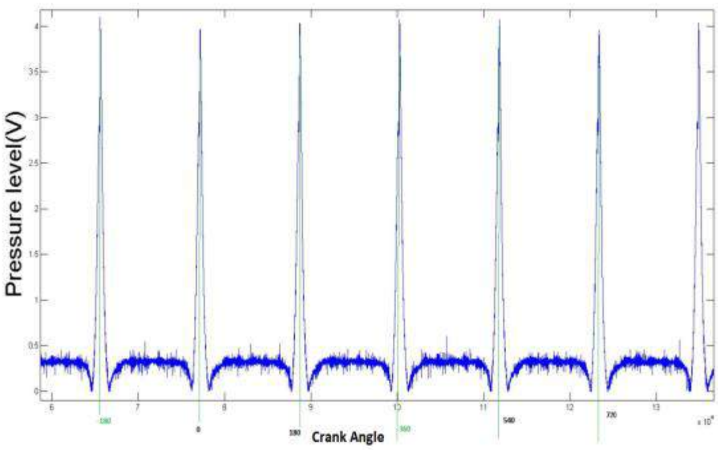

Fig. 2. Cylinder Pressure

Peaks in this figure correspond to combustion events taking place in the cylinder around TDC. These events can be more understood by time-frequency representation of graphs as shown in figure 3, which denotes that acoustic frequency at TDC positions is very high.

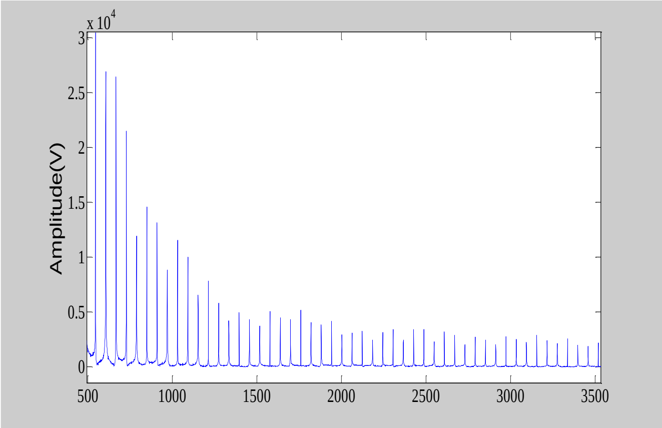

Fig. 3. Spectrum of Pressure Signals

2. Time-Frequency analysis

Cyclic averaging is the most efficient method to cancel the random noise. RMS value of sound can be calculated using relationship:

$$\text{RMS} = \frac{1}{n}\sum_{1}^{n}\sqrt{\frac{[s]^2}{T}} \quad [6]$$

Where: s is windowed engine cycle signal, n is number of cycles & T is time period of cycle.
The average SPWVD function is defined by relationship:

$$\text{(SPWVD)} = \frac{1}{n}\sum_{\mathrm{I}=1}^{n}(SPWVD)_{\mathrm{I}} \quad [7]$$

3. Experimental setup

Tests were done on a single cylinder HARTZ engine having specifications as presented in Table no 1.

Table 1: Engine Specifications

Type	Diesel Engine
Make	HARTZ
No of cylinder	**1**
Bore	69 mm
Stroke	65 mm
Displacement	0.243 liter
Compression	22:1
Maximum Power	3.5kW@4400RPM
Maximum Torque	10N-m @2000RPM

Table 2: Pressure Transducer Specifications

Range	0-250Bar
Sensitivity	20pC/Bar
Resonance Frequency	160kHz

The in-cylinder pressure was monitored by an AVL transducer having specifications shown in Table 2. Block vibrations were measured by means of a Endveco7240C type Mono axial accelerometer having features accelerometer are presented in Table no 3. The data recorded during each test was under steady state conditions as seen in Table no 4.

Table 3: Accelerometer Transducer Specifications

Range	1000g
Sensitivity	3pC/g
Resonance Frequency	90kHz

Table 4: Test Data Collected

Case	Load	Speed	Q (pre)	Q (main)	SOI (pre)	SOI (main)	P_{rail}
B3	50%	1600	1	6.3	19.9	5.09	508
BASE	100%	1600	1	13.8	14.8	6.29	714
B1	0%	1600	-	-	-	-	-
B2	50%	2000	1	6.6	22.5	5.68	515

4. Results and discussions

Figure no 4 shows the acoustic signals obtained from the testing conditions. The signals obtained may be contaminated by room resonance conditions. This distortion is maximum when the wavelength of sound waves matches with room dimensions. The resonance modes of rectangular room of length L, width W& height H is given by relationship:

$$f = \frac{c}{2}\sqrt{\frac{P^2}{L^2}+\frac{Q^2}{W^2}+\frac{R^2}{H^2}} \qquad [8]$$

Where c is velocity of sound in air & P,Q,R=0,1,2,3……

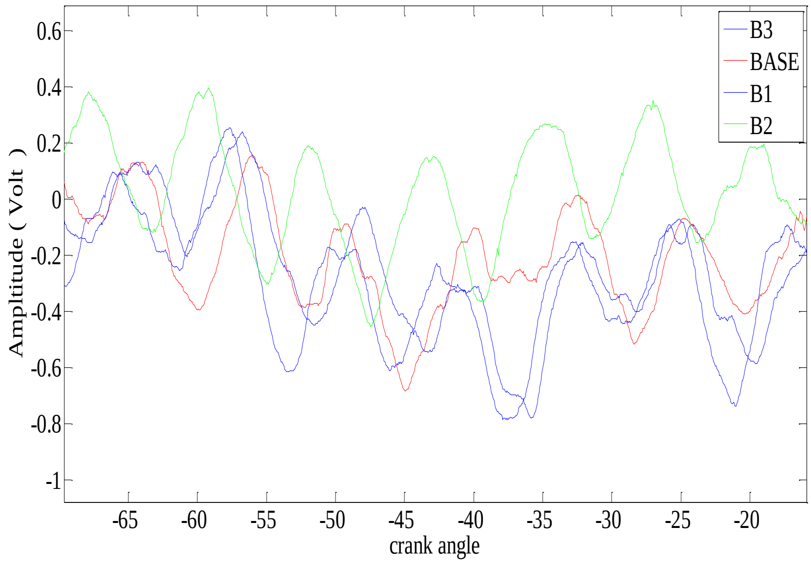

Fig. 4. Sound Data Acquired

Figure no 5-7 shows the time-frequency plots using Winger Ville function. Combustion events are evident by broadening of frequency bands around TDC positions. The onset of combustion events is evident by a sharp increase, which slowly decays with advanced crank angles. The even contribution of each cylinder is evident from the similar shape.

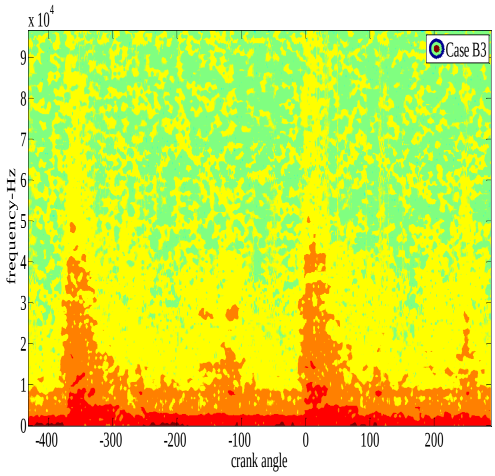

Fig. 5. Time-Frequency plot(B3)

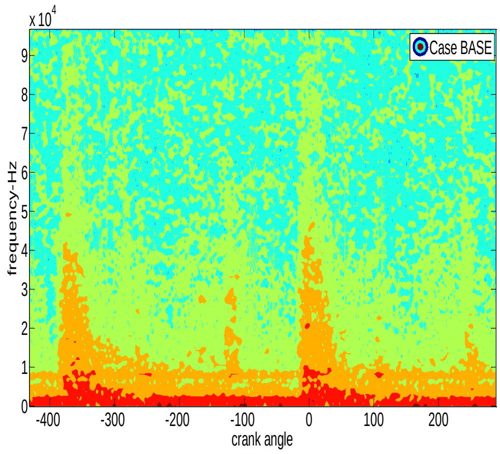

Fig. 6. Time-Frequency plot(BASE)

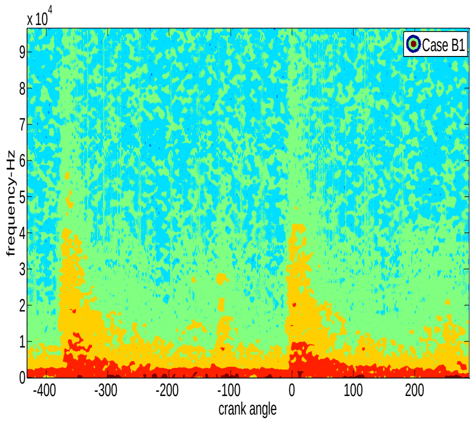

Fig. 7. Time-Frequency plot(B1)

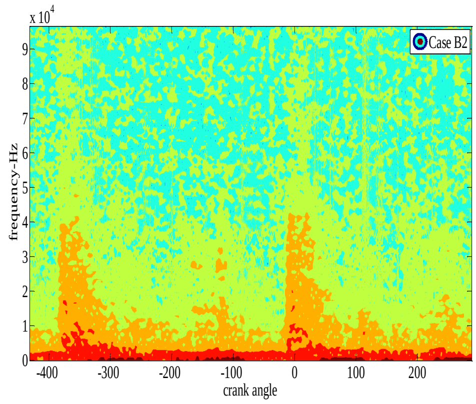

Fig. 8. Time-Frequency plot(B2)

These plots show that the dominant frequencies are below 100KHz & the fluctuations in amplitude of these frequencies below 1KHz does not correspond closely to combustion events. These observations endorse the anticipated resonance effects. Two persistent bands are visible around 10KHz& 40KHz which corresponds to resonances in pre amplifier and microphone respectively. Figure 9-12 show the CWT contour plots for the given testing conditions. It is clear that CWT plots do not provide detailed information in low frequency range as Winger Ville plots, however they highlight combustion features better at higher frequency ranges [9-26].

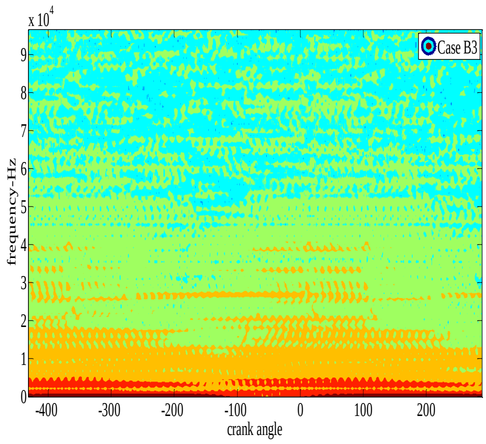

Fig. 9. CWT Time-Frequency plot(B3)

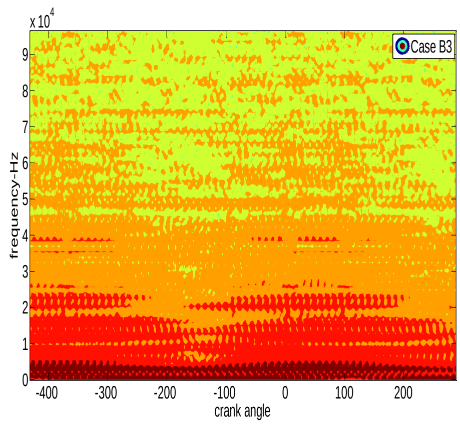

Fig. 10. CWT Time-Frequency plot(BASE)

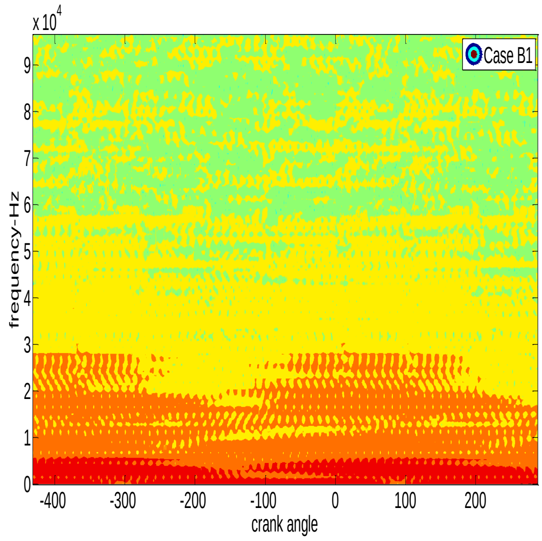

Fig. 11. CWT Time-Frequency plot(B1)

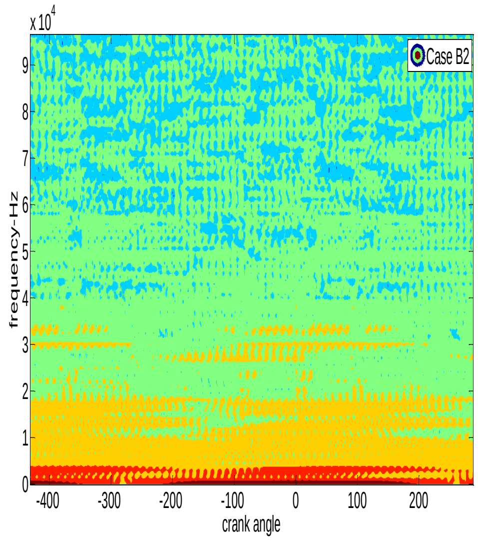

Fig. 12. CWT Time-Frequency plot(B2)

5. Conclusion

The sound models can be generated based upon the measurements of in cylinder pressures. Time frequency models show that at lower frequency ranges sound is distorted by external noise whereas at higher frequency ranges combustion events dominate. Use of Complex wavelet transformation and Pseudo Winger Ville distribution provides effective ways for condition monitoring of diesel engines.

References

[1] Narayan, S., Ivan Grujic, Nadica Stojanovic, Aleksandar Davinić, Jovan Dorić, and Jasna Glisovic. "Engine load impact on maximum value of normal force in piston mechanism." *Tractors and power machines* 23, no.1-2 (2018): 10-16.
[2] Narayan, S., Ivan Grujic, Nadica Stojanovic, Kaisan Muhammad Usman, Shitu Abubakar, and Faisal O. Mahroogi. "Design and analysis of an automotive single plate clutch." *Mobility & Vehicle Mechanics* 44, no. 1 (2018): 13-26.
[3] Narayan, S., Ivan Grujic, Nadica Stojanovic, Kaisan Muhammad Usman, Shitu Abubakar, and Faisal O. Mahroogi. "Application of various signal processing methods in combustion engines." *Mobility & Vehicle Mechanics* 44, no.1 (2018): 1-12.
[4] Stojanovic, Nadica, Jasna Glisovic, Ivan Grujic, Aleksandar Davinić, S. Narayan, Muhammad Usman Kaisan, and Shitu Abubakar. "3D Modelling and Aerodynamic simulation of a passenger car." *Machine Design* 10, no. 4 (2018): 153-156.
[5] Stojanovic, Nadica, Jasna Glisovic, Ivan Grujic, Sunny Narayan, Sasa Vasiljevic, and Bojana Boskovic. "Experimental and numerical modal analysis of brake squeal noise." *Mobility & Vehicle Mechanics* 44, no.4 (2018): 73-85.
[6] Mahroogi, Faisal O., and S. Narayan. "A recent review of hybrid automotive systems in GCC region." *Proceedings of institute of mechanical engineers Part D: Journal of Automotive engineering* 234, no.7 (2019): 1393-1402.
[7] Kaisan, M.U., S. Abubakar, B. Ashok, Dhinesh Balasubramanian, S. Narayan, Ivan Grujic, and Nadica Stojanovic. "Comparative analyses of biodiesel produced from Jatropha and neem seed oil using a gas chromatography mass spectroscopy technique." *Biofuels* (December 2018): DOI: 10.1080/17597269.2018.1537206.
[8] Narayan, Sunny, and Vipul Gupta. "Numerical Analysis of Secondary Motion of Piston Skirt in Engines." *International Journal of acoustics and vibrations (IJAV)* 23, no. 4 (2018): 557-565.
[9] Narayan, Sunny. "A review of diesel engine acoustics." *FME Transactions* 42, no.2, (2014): 150-154, DOI:10.5937/fmet1402150N.
[10] Narayan, S., Sasa Milojevic, and Vipul Gupta. "Combustion monitoring in engines using accelerometer signals." Journal of Vibro-engineering 21, no. 6 (2019): 1552-1563.
[11] Mahroogi, Faisal O., S. Narayan, and Vipul Gupta. "Acoustic transfer function in gasoline engines." *International Journal of Vehicle Noise and Vibration (IJVNV)* 13, no. 3 (2018): 270-280.

[12] Narayan, S. “Wavelet analysis of diesel engine noise.” *Journal of Engineering and Applied Sciences* 8, no. 8 (2013): 255-259.
[13] Narayan, S. “Analysis of Piston Slap Motion.” *International Journal of Applied Mechanics and Engineering IJAME* 20, no. 2 (2015): 445-450.
[14] Narayan, Sunny. “Piston Slap Noise in engines.” *International Journal of Applied Engineering Research* 8, no. 14 (2013): 1695-1700.
[15] Narayan, Sunny. “Effect of dwell time on noise radiated from Diesel engine.” *International Journal of Applied Engineering Research* 8, no. 11 (2013): 1339-1347.
[16] Kaisan, Muhammad Usman, Shitu Abubakar, Muhammed Mustapha M, and S. Narayan. “Determination of Wear Metals Debris Concentration in Aircraft Engines.” *International Journal of Recent Technology and Engineering (IJRTE)* 8, no. 2 (July 2019): 1289-1292.
[17] Narayan, S., Ali Sulaiman Alsagri, and Vipul Gupta. “Design and analysis of hybrid automotive suspension system.” *International Journal of Mechanical and Production Engineering Research and Development (IJMPERD)* 8, no. 2 (2018): 637-642.
[18] Mahroogi, Faisal O., and S. Narayan. “Design and analysis of Double Wishbone suspension systems for automotive applications.” *International Journal of Mechanical and Production Engineering Research and Development (IJMPERD)* 8, no. 11 (2018): 1433-1442.
[19] Stojanovic, Nadica, Nouby M. Ghazaly, Ivan Grujic, Jasna Glisovic, and S. Narayan. “Influence of size of ventilated brake disc’s ribs on air flow velocity.” *International Journal of Advanced Science and Technology IJAST* 29, no. 1 (2020): 637-647.
[20] Mahroogi, Faisal O., and S. Narayan. “Effects of dampers on piston secondary motion.” *International Journal of Vehicle Noise and Vibration (IJVNV)* 16, no. 1-2 (2018): 46–57.

Intelligent Hydraulic System for Comparative Functional Testing of Biodegradable Working Fluids

PhD Stud. Eng. **Liliana DUMITRESCU[1],** PhD Stud. Eng. **Ștefan-Mihai ȘEFU[1*],**
PhD Stud. Eng. **Ionela-Mihaela BACIU[1],** PhD Eng. **Marian BLEJAN[1]**

[1] Hydraulics and Pneumatics Research Institute INOE 2000-IHP, Bucharest, Romania
* sefu.stefan93@gmail.com

Abstract: *In the hydraulic field and especially in mobile hydraulics, the effect of oil losses on the environment (soil, water) is profoundly negative. In this context, the use of biodegradable fluids, with low impact on the environment, is one of the research directions lately developed. While some systems are made ever since the design phase so that they work with biodegradable fluids, most of the existing ones have been designed without taking into account this aspect. However, in the case of systems of previous generations, it is possible to use biodegradable oils as a working fluid following research on the compatibility of components with the fluid. The article presents a first step in this direction, by creating a stand that tests the effects of operation with biodegradable oil of simple hydraulic systems. The disadvantage of the large time required for testing can be mitigated by creating an intelligent data acquisition and transmission system, which eliminates the need for permanent monitoring by a human operator.*

Keywords: *Intelligent hydraulic systems, biodegradable hydraulic fluids, endurance tests*

1. Introduction

One of the most important components of hydraulic systems is the working fluid; its nature is different depending on the application, but also on the historical period. The most common - mineral oils - began to be used in hydraulic installations in 1920, although they were available since the early 20th century. The working fluids used in hydraulic systems suffer cyclically significant variations in speed, pressure and temperature; in addition, they are in contact with various materials and may be exposed to electromagnetic fields or even nuclear radiation, and so on. Such difficult fluid use conditions impose specific requirements: lubrication capacity, acceptable viscosity under all operating conditions, stable physical and chemical properties, low compressibility, limited foaming tendency, compatibility with materials in the system, etc.

There is currently a wide variety of working fluids that are chemically divided into several classes, but no fluid meets all the characteristics necessary for a given hydraulic transmission. In order to satisfy as many requirements of the hydraulic system as possible, the working fluid is added accordingly. Additives were introduced into mineral oils in the 1940s to improve the chemical and physical properties of hydraulic oils, especially anti-corrosion and anti-flammable ones. Over time, the problem of pollution and environmental degradation has arisen, mainly in agricultural land and the seas and oceans. At the beginning, there appeared the biodegradable lubricants used in the maritime industry since 1985, as an alternative to mineral oil products, which degrade slightly, slowly and inappropriately. Their advantages are rapid biodegradability and environmental protection due to the low eco-toxicity of chemicals entering the soil.

Although it seems an easy solution to a problem, the use of biodegradable oils cannot be recommended as a quasi-general solution; in some applications, a compatibility study with hydraulic systems is required in order to avoid malfunctions caused by improper use. As the tests that are most often performed are endurance tests, it is recommended to make intelligent stands that can operate without being constantly monitored by an operator. The stands for endurance testing of hydraulic fluids are based on the principles of intelligent hydraulics, consisting of pumping groups, pressure distribution and regulation groups, electronic controller, computer block with sensor and appropriate software, data acquisition, transfer and processing system, including the control block. The technological support for transferring and digitizing the entire system is the Internet of Things (IoT). IoT smart devices allow connecting via the Internet with other devices, services and automated systems, thus forming a network of objects. Intelligent hydraulics involves the analysis of processes and, to a certain extent, the making of the necessary decisions [1, 2].

2. Tested fluids and working methodology

As shown above, in some cases a test of the compatibility of biodegradable fluids with the other components of the hydraulic system is required; this applies when the system was not designed to work with such fluids, but it is desirable to replace mineral oils. The compatibility study is done starting with the most important components of the system; the work order would be power generators, distribution and control equipment, and hydraulic motors. The working methodology is a complex one, which verifies both the behavior of the equipment and the working fluids after long-term operation in load.

The fluids tested are the following:

a) ***KAJO-BIO-Hydrauliköl HETG 46***, from LUBRICON (Australia)

It is a hydraulic fluid based on vegetable oils, slightly biodegradable, environmentally friendly. The additives used provide excellent properties related to resistance to oxidation, corrosion, low temperature and extreme pressure. The density is 918 kg/m^3, the kinematic viscosity at 100ºC is 10 cSt.

b) ***Shell Naturelle Fluid HF-E 46***, from Shell Deutschland Oil GmbH

It is a hydraulic fluid with a density of 921 kg/m^3 and the kinematic viscosity at 40ºC is 47.2 cSt.

c) ***Lubrifin H46 EP***, from Total Lubrifin

It is a mineral oil that has been used as a benchmark. It has a density of 871 kg/m^3, and the kinematic viscosity at 40°C is between 41.4 - 50.6 cSt.

The test procedure involves performing commands that simulate the actual operation of a hydraulic system: performing double strokes of a linear hydraulic motor requires the actuation of an electrically operated directional control valve to supply alternately the two chambers of a cylinder. The loads on the two directions of movement were performed (simulated) with two pressure valves. The working frequency of 0.1 Hz was chosen so that the rhythm does not influence the operation and at the same time does not favor the appearance of faults. In this situation, the action of the thin slots in the devices on the working fluids, the diametrical clearances in the devices and the variation of some functional parameters over time will count.

For each of the 3 types of hydraulic oil, a stand was made with a minimal structure, but able to ensure the performance of the tests. The hydraulic devices used are identical in terms of hydraulic design, performance and manufacturer.

The proposed work sequence allows the following tests to be performed:

- Verification of the realization of the functional hydraulic schemes; it consists in checking the fluid flow in the two directions that simulate the chambers of a hydraulic cylinder.
- Dimensional verification of some components of the hydraulic equipment used to make the stands. To this end, the clearances between the spool and the body at the directional valves and the flow losses at 100 bar through the directional valves were checked. The measured data are included in the database.
- Measurement of functional parameters; the pressure drop on the directional valves and the flow variation are measured.
- Checking the purity of the working fluid before the start of the test program and during its running.
- Checking the kinematic viscosity of each working fluid.
- Carrying out an endurance program that adjusts the working pressure to 150 bar, the switching frequency to 0.1 Hz and a number of 600,000 cycles. Tests 1....5 are repeated every

200,000 cycles, following which some comparisons will be made and the necessary conclusions will be drawn.

3. Description of the constructive solution of the stands

3.1 Electro-hydraulic structure of the stands

Figure 1 shows the hydraulic operation diagram of the stands. The three stands are structurally and functionally identical.

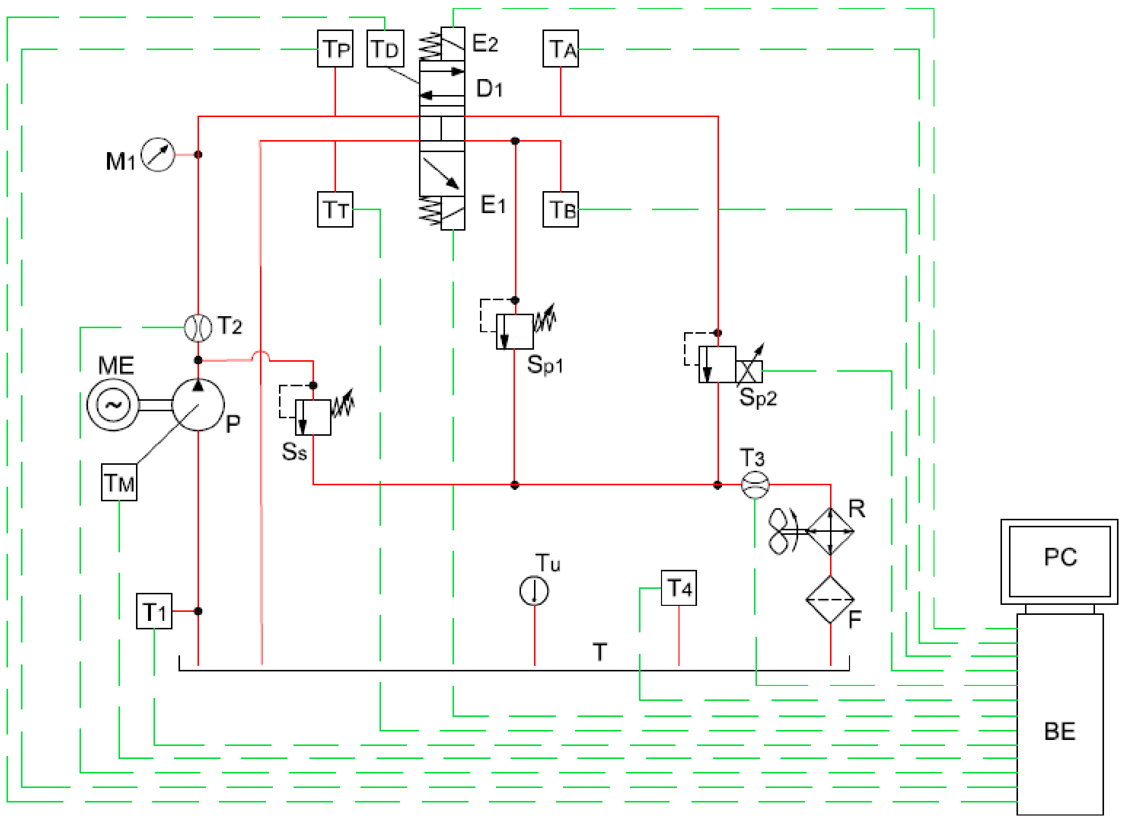

Fig. 1. Functional diagram of a hydraulic test stand

The hydraulic pump symbolized with P is driven by an electric motor ME, supplying the installation with the working fluid. The pump flow is measured with the flow meter T2. The pressure achieved in the system either by the pressure valve with manual adjustment Sp1 or by the electrically controlled proportional pressure valve Sp2, is measured with the pressure transducers TA and TB respectively. The T1 transducer measures the pressure on the suction path. The TD1, T4 and TM transducers monitor the operating temperatures of the pump, tank oil and directional valve D1. The flow difference between transducers T3 and T2 represents the loss of internal flow of directional valve D1. Directional valve selects which branches of the hydraulic circuit are active for the test. All commands and output signals are managed by the electronic block BE, which is directly connected to a PC.

The SS pressure relief valve ensures that the upper critical limit pressure is not exceeded in the hydraulic system. The heat exchanger R, allows the working fluid to cool when it reaches high temperatures, exceeding 60ºC. Filter F retains particles in the working fluid; such particles would increase the wear of the hydraulic equipment.

These identical stands study the changes in properties that occur in different types of working fluids and the degree of wear of hydraulic devices during operation. The electric motor is started from BE, which drives the hydraulic pump. By switching the directional valve to one of its fields, the desired working (test) valve is selected. In the first phase of the tests, the operating frequency was set to 0.1 Hz, which means that every 10 seconds the position of the directional valve spool changes. The working fluid is subjected to various loads created by manually adjustable valves or proportional valves. These loads range from 10 bar to 200 bar [3].

3.2. Computer system of working fluid test stands

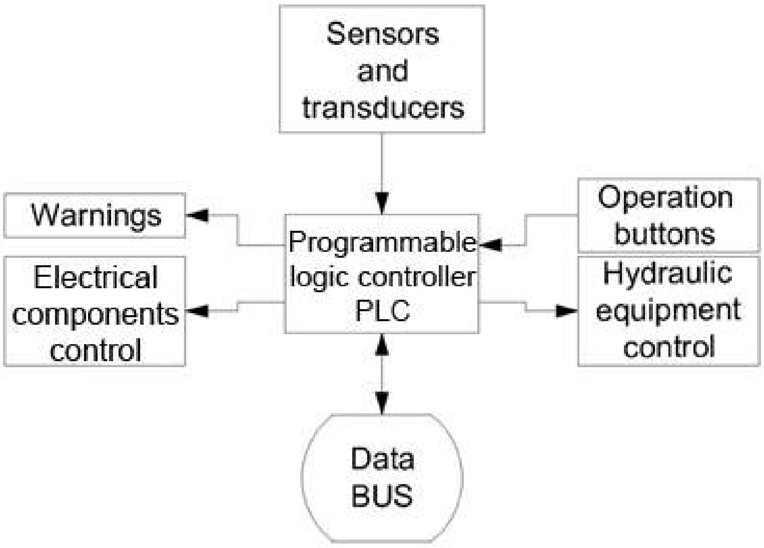

Fig. 2. Hardware structure of the data acquisition and control system of a designed test stand

The data acquisition and control system consists of transducers and sensors, electro-hydraulic converters specific to the control equipment (electromagnetic actuators) of the stand, as well as the operator console containing operation and control buttons and optical and acoustic signals of the system. These components are interfaced with the programmable logic controller PLC by electronic modules for the conversion of analog or digital electrical signals into standard electrical signals; in the case of analog signals, we work in the ranges -10 V… + 10 V, 4… 20 mA, and in the case of digital signals - in relay contacts, as to the input and output signals. The PLC reads/writes these signals and converts them to numeric or Boolean values (true/false). Another signal processing that is performed at the level of the programmable logic controller consists in scaling the numerical values in values corresponding to the measured or commanded physical parameter [4].

In addition, at the PLC level, digital/Boolean signals can be filtered to eliminate noise. Other functions performed by the PLC are to automate the testing process (e.g., starting the electric motor in the star or triangle position, selecting the hydraulic circuits specific to the tests performed, etc.), and also to exchange data with the higher hierarchical system via the data bus (see Figure 3).

The functional block diagram of the computer system for control and monitoring of stands is shown in Figure 3. The PC operating system communicates via the internal data bus (there can be RS485 serial bus or Ethernet) with the programmable logic controllers at each stand, with transducers and execution elements on the test stands. The software running on this PC allows the local operation of the system of test stands, as well as communication via LAN or IoT networks and Internet, with the database server running a DBMS (Data Base Management System) software, which allows storage and accessing of data specific to the tests performed [5, 6].

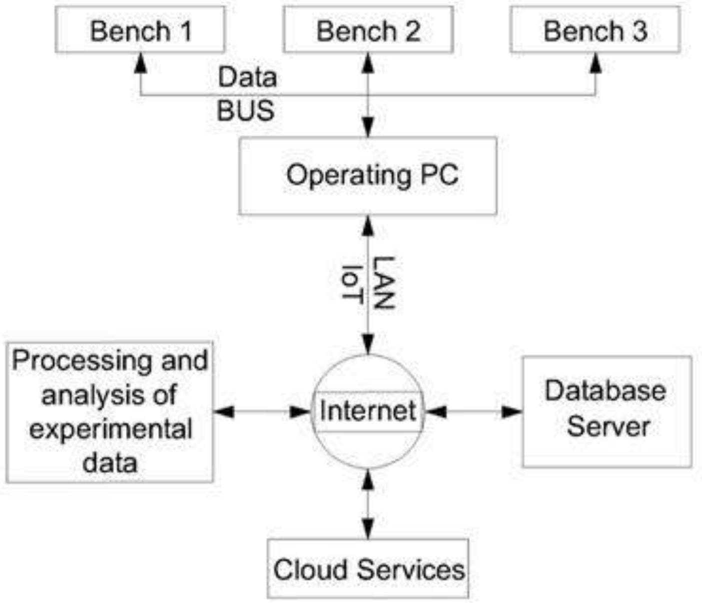

Fig. 3. Hardware structure of the computer system

The processing and analysis of experimental data can be performed on any PC connected to the Internet that has access to the database server, with dedicated software applications.
An alternative to database and experimental data processing may be the acquisition of Cloud Services to implement these features [7].

4. Results and conclusions

The results obtained so far, after performing an (incomplete) number of work cycles, allow the following conclusions to be drawn:

1. Following the first verification it was found that the biodegradable fluids can make the hydraulic scheme of the 2 stands (the third stand has as working fluid the H 46 hydraulic oil), at the test pressures of 5 bar; 50 bar; 100 bar, and 200 bar. No difference was found between the sizes measured simultaneously on the three stands; in other words, so far biodegradable fluids have had behavior and effects similar to those of conventional hydraulic oil in hydraulic systems.
2. The proposed and materialized scheme of the stand was validated by the proper operation of the three hydraulic assemblies.
3. Operation with a frequency of 0.1 Hz (directional valve control at 10 s) did not cause any malfunctions.
4. The degree of contamination of the working fluids is similar in all three cases, at the same time, and it is maintained in the accepted operating parameters; indirectly, it confirms that the use of biodegradable fluids does not cause wear different from that caused by mineral hydraulic oil.
5. The tests will be continued until the proposed number of cycles is reached (600,000); following that, at the end of the testing process a complete presentation of the results will be made.

Acknowledgments

This paper has been funded by the Romanian Ministry of Research and Innovation under NUCLEU Programme, Financial Agreement no. 18N/2019, Ad 13/14.04.2021, Project code PN 19-18.01.01, Phase 59 "Experimental research on the possibilities of reducing pollution by using biodegradable fluids in specific hydraulic drive systems". European funding has also been granted, under Competitiveness Operational Programme POC 2014-2020, call POC-A1-A.1.1.3-H-2016, Financial agreement no. 253/02.06.2020, signed between INOE 2000 and the Ministry of Education and Research for the project titled "Horizon 2020 Support Center for European project management and European promotion PREPARE", MYSMIS2014 code 107874.

References

[1] Avram, Mihai, Viorel Gheorghe, Despina Paula Duminică, and Constantin Udrea. *Hydrotronics and Pneutronics* / *Hidronica si pneutronica,* Bucharest, University Publishing House, 2008.
[2] Vasiliu, Nicolae, and Daniela Vasiliu. *Fluid Power* / *Acționări hidraulice și pneumatice* Vol.1, Bucharest, Technical Publishing House, 2005.
[3] Sorebo, Gib. "Managing the risk of the Internet of Things." *Control Engineering*, August 25, 2015. Accessed June 10, 2021. https://www.controleng.com/single-article/managing-the-risk-of-the-internet-of-things/03e6419374662db00e02f0436cbd5cb2.html.
[4] Laube, Martin, and Steffen Haack. "Condition Monitoring for hydraulic Power Units–user-oriented entry in Industry 4.0." Paper presented at the 10th International Fluid Power Conference IFK, Dresden, Germany, March 8-10, 2016.
[5] Avram, Mihai, Valerian-Emanuel Sârbu, Alina-Rodica Spânu, and Constantin Bucșan, "Intelligent hydraulic power generating group." *International Journal of Mechatronics and Applied Mechanics*, no. 3 (2018): 157-162.
[6] NI (National Instruments). "A Practical Guide for Connecting LabVIEW to the Industrial IoT." March 5, 2019. https://www.ni.com/ro-ro/innovations/white-papers/17/a-practical-guide-for-connecting-labview-to-the-industrial-iot.html.
[7] Avram, Mihai, Constantin Bucşan, Silvia Miu, Alina Spânu, and Marian Tănase. "Modular intelligent system for the control of proportional equipment." *The Romanian Review Precision Mechanics, Optics & Mechatronics*, no. 40 (2011): 311-314.

A Review of Combustion-Based Noise in Engines

Dr. **Vipul GUPTA[1]**, Dr. **S. NARAYAN[2*]**

[1] Indus University, India

[2] Qassim University, Saudi Arabia

* Corresponding author's e-mail address: rarekv@gmail.com

Abstract: *This portion of noise is attributed due to combustion process taking place inside cylinders. Previous works have shown that engine block vibrations are also sensitive towards various changes in fuel injection parameters. Accelerometer signals have been able to locate various important features of combustion process in diesel engines. Use of in cylinder pressure and block vibration transducers form an important methodology for analysis of combustion process taking place in diesel engines. Data from microphones located at a suitable distance from engine also provides an important information about performance of engines, however there is a major risk of contamination of these signals.*

Keywords: *Noise, vibrations, acoustic*

1. Introduction

Combustion noise generated mainly depends upon the rate of in cylinder pressure developed during ignition delay period. Overall design of combustion chamber as well as variations in various fuel injection parameters e.g., injection pressure, amount of fuel injected and its timings also play a crucial role in contributions of combustion noise emissions from engines [1]. Depending upon the type of engine as well as various operational parameters, overall noise emissions from a typical diesel engine may be in range 80-110dBA [2, 3]. Split injection using electronic control unit (E.C.U.) may help to shortens the period of premixed phase of combustion and hence help to reduce the overall noise emissions by about 5-8dBA [4]. Head and Wakes have shown that during transient operational conditions, overall noise levels are about 4-7dBA higher as compared to steady state operations [5]. Cold starting conditions may lead to higher ignition delay period, which in turn causes increase in the premixed period of combustion [6]. Quality of fuel injected inside combustion chamber also affects the magnitude of combustion noise. It has been observed that a reduction of Cetane number of fuel from 50 to 40 causes a rise of up to 3 dBA in combustion based noise emissions [7]. For a naturally aspirated engine, the combustion-based noise depends upon the quantity of fuel that mixes with air charge during the course of delay period and hence the compression ratio of engines also plays a vital role [7]. In case of gasoline engines, the delay period is longer due to lower compression ratio, which may lead to lower temperature of charge and hence more noise emissions [7].

2. Background of combustion process in diesel engines

Due to high efficiency, diesel engines have been a favorite choice in case of heavy-duty automobiles including trucks [8]. However, they suffer from major drawbacks of high noise, weight and vibrations. These engines may be further classified into following two major types:
1. Direct injection (D.I.) engines
2. Indirect injection (I.D.I.) engines
In case of D.I. engines, the fuel is injected directly inside the combustion chamber and as a consequence of it, lesser time is available for formation of fuel and air mixture. Hence, a heterogeneous mixture consisting of both rich as well as lean parts is formed inside the chamber.

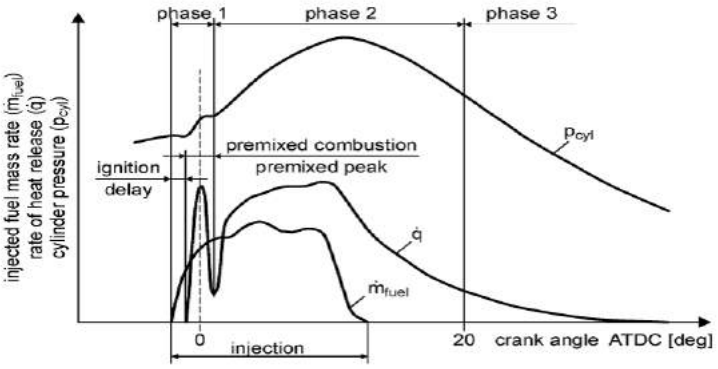

Fig. 1. Various phases of Diesel engine combustion [8]

Figure no 1 shows various phases of combustion as observed during course of operation of a typical diesel engine. The delay phase starts with onset of injection process and ends with beginning of premixed phase of combustion. The injection of fuel inside combustion chamber begins a few degrees before TDC position depending on the various injection conditions of engine. As soon as the cold jet of fuel penetrates the chamber, it mixes up with hot compressed air already present inside. The droplets thus formed vaporize, forming layers of fuel-air mixture around the periphery of jet. As the temperature rises to about 750K, the first break down of Cetane fuel takes place. Further propagation of various chemical reactions produces C_2H_2, C_3H_3, C_2H_4, CO_2 as well as water vapors [9].

Resulting rise in temperatures causes a complete combustion of fuel-air mixture formed. This sudden period of combustion further leads to rise in the heat release rate as well as high pressure gradient($\frac{dP}{d\theta}$). This further enhances temperatures in the pre-mixed zone leading to conditions favourable for production of NO_x. Once the premixed phase consumes all mixture formed,oxygen available for combustion is consumed around the inner regions wherein the temperatures in ranges of 1600-1700K are reached [8]. Now various partially burnt particles diffuse towards outer layers and begin to burn withina thin region of reaction formed around the periphery of spray leading to formation of a diffusion flame.

This phase of combustion is known as diffusion controlled combustion and is depicted by region 2 and 3 in figure no 1. Higher temperatures along with lack of oxygen provides an ideal condition for the formation of soot.

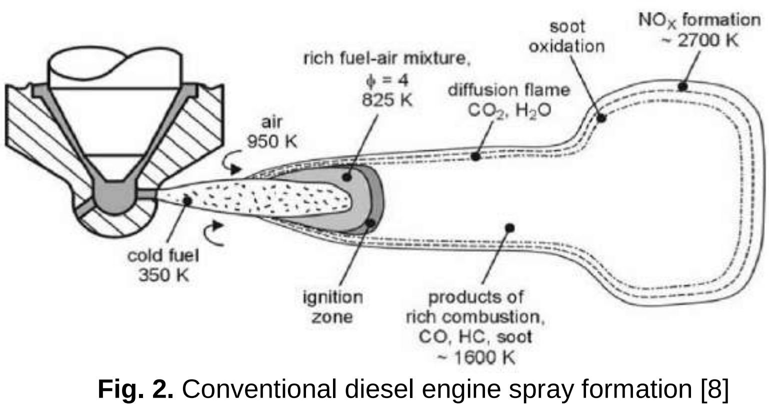

Fig. 2. Conventional diesel engine spray formation [8]

The diffusion flame thus formed then uses rest of oxygen available from surrounding environment resulting in high temperatures of order 2700K, which consumes all the soot formed. At outer zone of flame, there is enough oxygen content for formation of NO_x. Figure no 3 shows the rate of soot formation as a function of crank angle. Most of soot that is formed during earlier stages is later consumed and hence final exhaust emissions may have only a fraction of initial soot emissions. As seen from figure no 1, the diffusion-controlled combustion can be divided into further three phases. During the second phase, the burning rate is dependent on rate of mixing of fuel fragments formed and air and hence rate of reaction is faster. During the third phase, oxidation of remaining unburnt particles and soot takes place, however due to decreased temperature of end gas formed during the expansion stroke as well as lesser oxygen content available, slower reaction rates are observed.

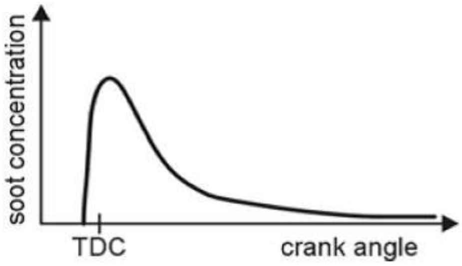

Fig. 3. Rate of soot formation [8]

Process of NO_X and soot formation in combustion engines has shown an opposite trend as shown in figure no 4. In order to reduce the NO_x formation rate it is necessary that local temperatures must not rise beyond 2000K [8]. A possible way to do so is to inject fuel late inside combustion chamber, which further shifts the combustion phase towards expansion phase resulting in significant reduction of chamber temperatures. However, rate of consumption of fuel and soot formation increases due to late combustion.

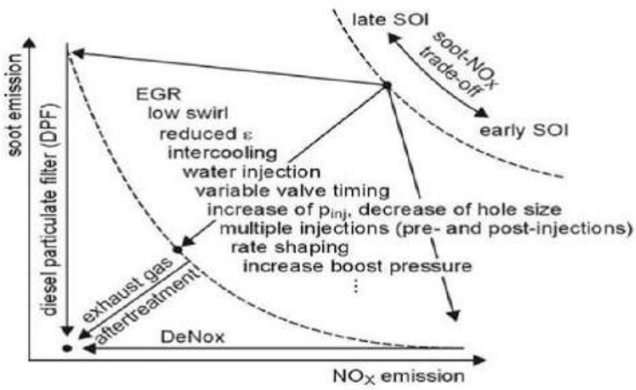

Fig. 4. Soot & NOx trade off [8]

Hence, modern systems utilize multiple injection techniques in order to control both NO_x as well as soot formation rate [8, 9, 10, 11].

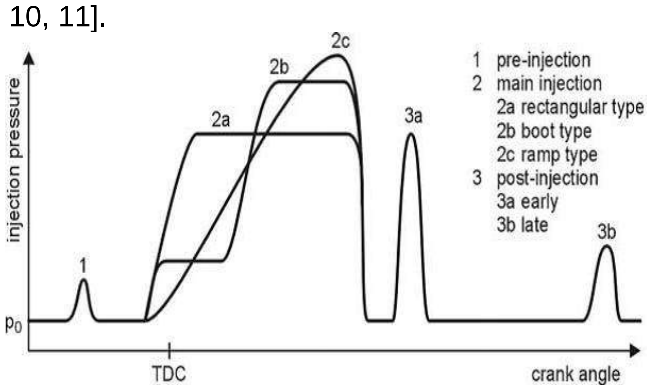

Fig. 5. Multiple injection methods adopted for modern diesel engines [8]

3. Conclusions

There are generally three phases of injection process used, namely pre-injection period, main-injection period & post injection period. There is a delay period between instant at which fuel is injected inside the combustion chamber and actual start of ignition process. Greater this delay period, more is the temperature achieved during course of combustion and hence better conditions exist for NOx formation. In order to shorten this delay period, a small amount of fuel is pre-injected before main injection occurs during the phase of pre-mixed combustion. Torque and power produced in engine mainly depends on the duration of main injection period. It is advantageous to vary the injected fuel mass with time in order to reduce the specific consumption of fuel. This is achieved by rate shaping as seen in figure no 5. Rate shaping curve may be rectangular, step or boot type in shape. Post-injection of fuel is done in order to reduce the soot emissions and in some cases may be useful for exhaust gas recirculation treatment [12]. It has been reported that post injection may reduce the rate of soot formation by about 70% without increasing the fuel consumption [13-20].

References

[1] Narayan, S., Ivan Grujic, Nadica Stojanovic, Aleksandar Davinić, Jovan Dorić, and Jasna Glisovic. "Engine load impact on maximum value of normal force in piston mechanism." *Tractors and power machines* 23, no.1-2 (2018): 10-16.

[2] Narayan, S., Ivan Grujic, Nadica Stojanovic, Kaisan Muhammad Usman, Shitu Abubakar, and Faisal O. Mahroogi. "Design and analysis of an automotive single plate clutch." *Mobility & Vehicle Mechanics* 44, no. 1 (2018): 13-26.

[3] Narayan, S., Ivan Grujic, Nadica Stojanovic, Kaisan Muhammad Usman, Shitu Abubakar, and Faisal O. Mahroogi. "Application of various signal processing methods in combustion engines." *Mobility & Vehicle Mechanics* 44, no.1 (2018): 1-12.

[4] Stojanovic, Nadica, Jasna Glisovic, Ivan Grujic, Aleksandar Davinić, S. Narayan, Muhammad Usman Kaisan, and Shitu Abubakar. "3D Modelling and Aerodynamic simulation of a passenger car." *Machine Design* 10, no. 4 (2018): 153-156.

[5] Stojanovic, Nadica, Jasna Glisovic, Ivan Grujic, Sunny Narayan, Sasa Vasiljevic, and Bojana Boskovic. "Experimental and numerical modal analysis of brake squeal noise." *Mobility & Vehicle Mechanics* 44, no.4 (2018): 73-85.

[6] Mahroogi, Faisal O., and S. Narayan. "A recent review of hybrid automotive systems in GCC region." *Proceedings of institute of mechanical engineers Part D: Journal of Automotive engineering* 234, no.7 (2019): 1393-1402.

[7] Kaisan, M.U., S. Abubakar, B. Ashok, Dhinesh Balasubramanian, S. Narayan, Ivan Grujic, and Nadica Stojanovic. "Comparative analyses of biodiesel produced from Jatropha and neem seed oil using a gas chromatography mass spectroscopy technique." *Biofuels* (December 2018): DOI: 10.1080/17597269.2018.1537206.

[8] Narayan, Sunny, and Vipul Gupta. "Numerical Analysis of Secondary Motion of Piston Skirt in Engines." *International Journal of acoustics and vibrations (IJAV)* 23, no. 4 (2018): 557-565.

[9] Narayan, Sunny. "A review of diesel engine acoustics." *FME Transactions* 42, no.2, (2014): 150-154, DOI:10.5937/fmet1402150N.

[10] Narayan, S., Sasa Milojevic, and Vipul Gupta. "Combustion monitoring in engines using accelerometer signals." *Journal of Vibro-engineering* 21, no. 6 (2019): 1552-1563.

[11] Mahroogi, Faisal O., S. Narayan, and Vipul Gupta. "Acoustic transfer function in gasoline engines." *International Journal of Vehicle Noise and Vibration (IJVNV)* 13, no. 3 (2018): 270-280.

[12] Narayan, S. "Wavelet analysis of diesel engine noise." *Journal of Engineering and Applied Sciences* 8, no. 8 (2013): 255-259.

[13] Narayan, S. "Analysis of Piston Slap Motion." *International Journal of Applied Mechanics and Engineering IJAME* 20, no. 2 (2015): 445-450.

[14] Narayan, Sunny. "Piston Slap Noise in engines." *International Journal of Applied Engineering Research* 8, no. 14 (2013): 1695-1700.

[15] Narayan, Sunny. "Effect of dwell time on noise radiated from Diesel engine." *International Journal of Applied Engineering Research* 8, no. 11 (2013): 1339-1347.

[16] Kaisan, Muhammad Usman, Shitu Abubakar, Muhammed Mustapha M, and S. Narayan. "Determination of Wear Metals Debris Concentration in Aircraft Engines." *International Journal of Recent Technology and Engineering (IJRTE)* 8, no. 2 (July 2019): 1289-1292.

[17] Narayan, S., Ali Sulaiman Alsagri, and Vipul Gupta. "Design and analysis of hybrid automotive suspension system." *International Journal of Mechanical and Production Engineering Research and Development (IJMPERD)* 8, no. 2 (2018): 637-642.
[18] Mahroogi, Faisal O., and S. Narayan. "Design and analysis of Double Wishbone suspension systems for automotive applications." *International Journal of Mechanical and Production Engineering Research and Development (IJMPERD)* 8, no. 11 (2018): 1433-1442.
[19] Stojanovic, Nadica, Nouby M. Ghazaly, Ivan Grujic, Jasna Glisovic, and S. Narayan. "Influence of size of ventilated brake disc's ribs on air flow velocity." *International Journal of Advanced Science and Technology IJAST* 29, no. 1 (2020): 637-647.
[20] Mahroogi, Faisal O., and S. Narayan. "Effects of dampers on piston secondary motion." *International Journal of Vehicle Noise and Vibration (IJVNV)* 16, no. 1-2 (2018): 46–57.

FLUIDAS

NATIONAL PROFESSIONAL ASSOCIATION OF HYDRAULICS AND PNEUMATICS IN ROMANIA

fluidas@fluidas.ro